2013

Ultrafast Laser Material Processing For Photonic Applications

Mark Ramme
University of Central Florida

University of
Central
Florida

STARS
Showcase of Text, Archives, Research & Scholarship

ULTRAFAST LASER MATERIAL PROCESSING FOR PHOTONIC APPLICATIONS

by

MARK RAMME
Dipl.Ing. University of Applied Sciences Aachen, 2006
M.S. University of Central Florida, 2007

A dissertation submitted in partial fulfillment of the requirements
for the degree of Doctor of Philosophy
in the Department of Electrical Engineering and Computer Science
in the College of Engineering and Computer Science
at the University of Central Florida
Orlando, Florida

Summer Term
2013

Major Professor: Martin Richardson

ABSTRACT

Femtosecond Laser Direct Writing (FLDW) is a viable technique for producing photonic devices in bulk materials. This novel manufacturing technique is versatile due to its full 3D fabrication capability. Typically, the only requirement for this process is that the base material must be transparent to the laser wavelength. The modification process itself is based on non-linear energy absorption of laser light within the focal volume of the incident beam.

This thesis addresses the feasibility of this technique for introducing photonic structures into novel dielectric materials. Additionally, this work provides a deeper understanding of the light-matter interaction mechanism occurring at high pulse repetition rates. A novel structure on the sample surface in the form of nano-fibers was observed when the bulk material was irradiated with high repetition rate pulse trains.

To utilize the advantages of the FLDW technique even further, a transfer of the technology from dielectric to semiconductor materials is investigated. However, this demands detailed insight of the absorption and modification processes themselves. Experiments and the results suggested that non-linear absorption, specifically avalanche ionization, is the limiting factor inhibiting the application of FLDW to bulk semiconductors with today's laser sources.

Für meine Eltern – Ursula und Reiner.

Eure Unterstützung und Euer Vertrauen in mich

waren, und sind, unverzichtbar.

ACKNOWLEDGMENTS

TABLE OF CONTENTS

LIST OF FIGURES

LIST OF TABLES

LIST OF CONSTANTS

Constant	Constant Name	Constant Value
c	Vacuum speed of light	$3 \cdot 10^8 \ m/s$
e	Electron charge	$1.602 \cdot 10^{-19} \ C$
ϵ_0	Vacuum permittivity	$8.854 \cdot 10^{-12} \ F/m$
h	Planck constant	$6.626 \cdot 10^{-34} \ m^2 kg/s$
m_e	Electron mass	$9.1093 \cdot 10^{-31} \ kg$
μ_0	Vacuum permeability	$4\pi \cdot 10^{-7} \ Vs/Am$

LIST OF ACRONYMS

Acronym	Meaning
2PA	Two-photon absorption
3PA	Three-photon absorption
Al_2O_3	Aluminum Oxide
B_2O_2	Dioxodiborane
BBO	Barium Borate
CaO	Calcium Oxide
CB	Conduction band
CCD	Charge-coupled device
CPA	Chirped pulse amplification
CREOL	Center for Research and Education for Optics and Lasers
Cz	Czochralski
DFG	Difference Frequency Generation
DIC	Differential Interference Contrast
E-field	Electric field
EM-field	Electro-Magnetic field
EM-wave	Electro-Magnetic wave
EO modulator	Electro-optic modulator
FCPA	Fiber-Chirped-Pulse-Amplifier
FLDW	Femtosecond laser direct writing

FZ	Floatzone
(c:)GaAs	(crystalline) gallium arsenide
HA	Heat accumulation
HAZ	Heat affected zone
hh	heavy hole
HSFL	High spatial frequency LIPSS
InP	Indium Phosphide
IR	Infrared
lh	light hole
LIPSS	Laser-induced periodic surface structure
LSFL	Low spatial frequency LIPSS
MOPA	Master-oscillator power-amplifier
MPI	Multi-photon ionization
NA	Numerical Aperture
NaO	Sodium Oxide
NIR	Near-IR
OPA	Optical Parametric Amplifier
P-LIPSS	Parallel LIPSS
SEM	Scanning Electron Microscope
(c:)Si	(crystalline) Silicon
SiC	Silicon Carbide

SiO$_2$	Silicon Oxide
SO	Split-Off band
STE	Self-trapped excitons
TE	Transvers electric field
TEM	Transmission Electron Microscope
Ti:Saph	Titanium:Sapphire
TM	Transvers magnetic field
TTM	Two-Temperature-Model
UFLMP	Ultrafast Femtosecond Laser Material Processing
VB	Valence band

1 INTRODUCTION

1.1 Motivation

With the advent of tabletop femtosecond laser sources, the interest in their use for material processing applications rose quickly due to the extraordinary interaction mechanism between ultrashort-pulsed [1] light and matter. This short pulse duration enables material-independent athermal processing, which greatly reduces the heat-affected zone (HAZ) around the incident radiation [1]-[6] and allows for the reduction of feature size. The ultra-high intensities inherent to such ultrashort-pulsed laser beams have opened a range of new materials to process, such as dielectrics, ceramics or composite materials. Furthermore, it enables the possibility of non-linear absorption taking place in a well-defined focal volume in the bulk of transparent materials, which made true 3D structuring possible. 3D femtosecond laser direct writing (3D FLDW) became an interesting technology to fabricate embedded photonic devices and circuits in transparent dielectrics [7]-[14]. Even though various applications of the technology have been demonstrated, many of the underlying physical processes are still not understood completely.

In recent years, ultrashort-pulsed laser sources into the near-infrared (NIR) and mid-infrared (mid-IR) region of the spectrum have been developed. Thus, a transfer of the 3D FLDW technology towards semiconductor materials has become possible, offering micro-electronic components to be processed [15], [16]. The electronics industry faces many challenges due to the departure from planar circuits towards stacked electronics [17], [18]. This could be enabled using

---

[1] Light pulses with a temporal width of less than 1 ps are considered to be ultrashort pulses in this document.

the 3D FLDW technology. Moreover, historically the electronics industry has proven to promote new technologies more quickly from the laboratory test bed to an industrial production line compared to, say, the automobile industry. Since SEMATECH is an industry-owned, industry-governed industrial research corporation its long lifetime over the past several decades is proof the model works [19], [20]. However, to ease the engagement of the industrial partners further an extended knowledge of the physical processes that are involved in the particular light-matter interaction is necessary for successful technology transfer into this new material group.

Here we investigate the fundamental interaction processes of ultrashort-pulsed light in dielectrics and semiconductor materials, focusing on, absorption and modification phenomena resulting from the availability of free absorbers. First, the influence of processing speed, in particular laser pulse repetition rate and therefore scalability of the processing, is studied. Second, the different material modification threshold behavior of semiconductor materials due to the smaller band gap energy compared to dielectric materials is researched. An influence of free absorbers could lead to a reduced sensitivity of the processing process with respect to the incident photon energy.

1.2   History of Lasers

1.2.1   The Beginnings of Optics

Today lasers are an essential part of our daily life. From the barcode scanner in the grocery store to laser pointers in lectures to large-scale laser cutting robots on car production lines, our lives would be dramatically different without lasers.

The basis, which finally led to the development of the laser by Maiman in June 1960 [21], were laid much earlier by many researchers and scientists. One could argue that da Vinci's studies

of reflection and refraction by mirrors and lenses around 1500 [22] are the beginnings of modern optics. Undoubtedly, Huygens wave theory of light from 1690 [23] marks a cornerstone of modern optics, which was verified by Youngs well known slit and double-slit experiments in 1801 [24]. Later that century, Maxwell revolutionized the field of optics with the formulation of the four Maxell equations [25] in 1865.

$$\nabla \cdot \vec{D} = \rho \tag{1.1}$$

$$\nabla \cdot \vec{H} = 0 \tag{1.2}$$

$$\nabla \times \vec{E} = -\mu_0 \frac{\partial \vec{H}}{\partial t} \tag{1.3}$$

$$\nabla \times \vec{H} = \frac{\partial \vec{D}}{\partial t} + \vec{J} \tag{1.4}$$

Even though the knowledge necessary to formulate these equations was established before Maxwells formulations, the realization of the combinatory character of these four laws allowed for a mathematical description of light wave propagation, the so-called wave equation, here for a charge-free, linear medium [26],

$$\nabla(\nabla \cdot \vec{E}) - \nabla^2 \vec{E} = \mu_0 \left(\epsilon_0 \frac{\partial^2 \vec{E}}{\partial t^2} + \frac{\partial^2 \vec{P}}{\partial t^2} \right) \tag{1.5}$$

Max Planck then postulated in 1901 the theory that energy is being emitted from a blackbody radiator in discrete packages, so-called quanta [27], which led to Albert Einstein's introduction of 'energy quanta' as bundles of wave energy [28] in 1905. The name 'photon' was established much later in 1926 by the American chemist G.N. Lewis [29].

1.2.2 The Development of the Theory of the Laser

The theory of optical absorption and emission was first published by Einstein in 1916 [30]. One year later however, he proposed the principle of stimulated emission [31], a fundamental

process necessary for the development of the laser. Nevertheless, it took another 4 decades before Alfred Kastler discovered the scheme of optical pumping [32]. Before this could take place, Tolman and Ehrenfest needed to suggest the notion that the radiation emitted due to stimulated emission had to be coherent [33]. Furthermore, in 1939 V.A. Fabricant, a Russian physicist, observed negative absorption [34]. This would be later known as population inversion. Finally, in early 1954 Charles Townes and his students Gordon and Zeiger at Columbia University operated the first maser device [35]. The ammonia beam maser emitted radiation at 24 GHz. Around the same time, the two Russian researchers Basov and Prokhorov developed a very similar device [36]. However, the name maser was then already being established by Townes and his team.

After Kastler realized the optical pump scheme, Nicholas Bloembergen proposed 3-level pumping to obtain continuous population inversion and therefore continuous light emission [37]. Finally, in 1958, Townes and Schawlow published their famous and often cited paper on the principle of an optical frequency maser [38].

1.2.3   The Birth of the Laser

Many scientist and researchers were working in the late 1950s and early 1960s on the development of a laser device. Due to advances in crystal growth technology, Maiman was able to reach the goal of light amplification by stimulated emission of radiation, dubbed the LASER first in 1960 using a flash lamp pumped Ruby crystal. His laser emitted pulsed radiation at a wavelength of 694 nm. Later in the same year, Ali Javan at Bell Laboratories developed the Helium-Neon gas laser [39], then emitting radiation at 1150 nm, nowadays still very common at 632 nm wavelength. The first semiconductor laser was realized by Fenner in 1962, followed by Patel's CO_2 laser in early 1964 [40] and the first pulsed Nd:YAG (neodymium-doped yttrium aluminum garnet;

Nd:$Y_3Al_5O_{12}$) by Geusic [41]. The principle of Q-switching was published two years prior by Hellwarth and McClung [42]. The governing rate equations for Q-switching were derived by Wagner and Lengyel [43] in 1963. Essential for the later development of ultrafast laser sources was the theoretical work on the principle of mode-locking by Hargrove in 1964 [44], DiDomenico *et al.* in 1966 [45] and later by Kuizenga and Siegman in 1970 [46]. The first experimental demonstration of Kerr-Lens mode-locking of a laser cavity, however, was done in 1975 by Sala and Richardson [47], [48]. Worth mentioning here is that even though ultrashort pulsed laser sources with pulse durations in the femtosecond regime were available using colliding pulse mode-locking in dye lasers before 1988 [49], [50], the technical development of the Titanium:Sapphire (Ti:Saph) laser by Peter Moulton [51] made ultrashort pulsed laser sources practical for the use in laser processing applications, as will be explain later in Section 1.3.2.

1.3   History of Laser Material Interaction

1.3.1   Lasers - A Flexible Machining Tool

When processing materials with traditional tools such as drills or mills, each of the tools used during the fabrication process has a discrete purpose. Often, this singular purpose can be accomplished with high precision and quality, but at the cost of needing many tools with exactly one purpose. This notion changed dramatically with the introduction of lasers as a tool for material processing. The new "laser tool" is an extremely flexible machining tool, which provides the foundation for innovation for an entire new industry, laser material processing. The basis of that flexibility are laid by three major points:

- o   the type of the laser source, given by the active medium, the emitted power, and the mode of operation, i.e. cw or pulsed

o   the mode in which the light interacted with matter, namely thermal or non-thermal

o   the physical mechanism of interaction in either mode, for thermal those were heating, melting or vaporization, for non-thermal mostly breaking or creating bonds.

Currently lasers are commonly used in a wide variety of tasks in daily life such as in healthcare (i.e. LASIK), manufacturing for welding, cutting, surface modification, surface structuring, additive fabrication, chemical interaction and many more, telecommunication for fiber-optic transmission and even in the arts world for non-destructive cleaning of antique artifacts and entertainment.

Triggered by the prospect of such novel technologies and applications using lasers, the need to understand the fundamental light-matter interaction processes is greater than ever. Experiments on periodic surface structuring by Birnbaum [52], studies of laser-induced surface damage by Bass and Barrett [53] and studies of electrical breakdown in solids by Bloembergen [54] are examples of the early work in this field.

One of the early advantages of laser material processing was that the interaction regime could be chosen to be either thermal or athermal. Athermal meant that the interaction process did not rely on heating effects but on photochemical or photolytic processes. This type of processing became of even greater importance after ultrashort-pulsed sources based on the Ti:Saph laser were more easily available for laser material processing. This new laser source also renewed the interest in research of interaction phenomena between light and matter in the ultrashort pulse regime [55]-[57].

1.3.2   Five Decades of Laser Material Processing

To cite the author of the book 'Laser processing of engineering materials: principles', John Ion, "the reason for continued research and development in lasers for material processing has been either a 'technological push' – a solution looking for a problem – or an 'industrial pull' – a problem looking for a solution" [58]. The triumph of the laser in material processing technologies was greatly influenced by three factors. First, the vast commercialization of a wide range of laser sources allowed for their implementation in the processing chain. Second, continuous advances in automation, process control and monitoring as well as system integration eased the implementation of lasers. Third, the industry's attitude to quickly moving novel processes from the development lab onto the fabrication floor kept the demand on improvements in the technology high.

The unique properties of the laser light were the driving force behind applications in material processing in the first decade after the invention of the laser. Monochromacity and low divergence were especially useful for drilling, cutting and welding application. Raytheon engineers explored laser drilling extensively [58]. Steel sheets were welded together using a Ruby laser in 1963. In the mid-60's, German researchers investigated the use of laser radiation for heat treatment applications [58]. The first laser cutting process was developed by Sullivan in 1967 when a 1 mm thick steel plate was cut using a 300 W CO_2-laser assisted by an oxygen gas-jet. Surprisingly, 3 years earlier the process was already publically demonstrated in the movie *James Bond – Goldfinger*, as shown in Fig. 1.1.

The 1970's were led by the discovery of the fused silica optical fiber by Kao and Hockham [59], [60]. This development should not be underappreciated since it provided an efficient way of laser light delivery for processing applications. Moreover, it is the base of the current laser

technology and it future development. At the same time laser cutting was first realized in an industrial scale. The process was utilized to cut slots into electronic dieboards. Synchronously, other researchers presented laser welds of indistinguishable quality as from welds generated by established technologies.
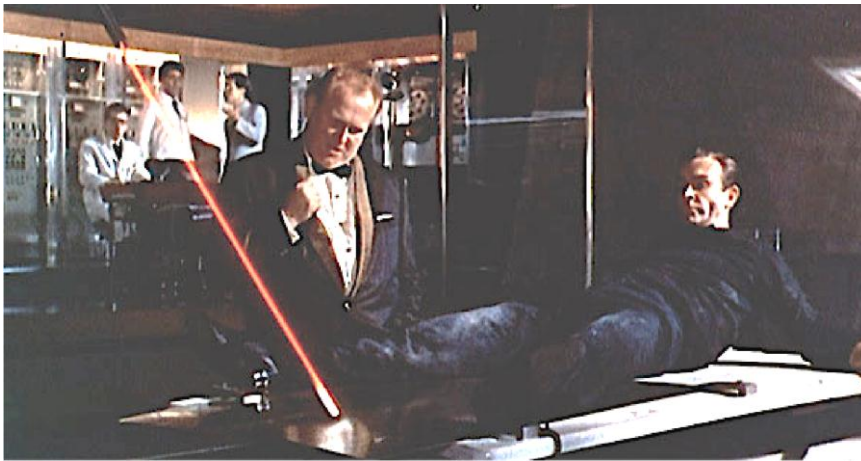
Fig. 1.1 - Public demonstration of laser cutting of steel in the 1964 movie *James Bond – Goldfinger*, 3 years before the actual process was first demonstrated (*James Bond – Goldfinger*, Eon Productions, 1964)

After the discovery of optical fibers in the 70's, the 1980's saw their vast utilization in industrial beam delivery systems. Clunky and sensitive mirror delivery geometries were easily replaced by optical fibers.

At the beginning of the same decade, Rolls-Royce developed the first additive laser process [61]. Their engineers used a blown powder process to fabricate hard-faced regions to repair expensive turbine blades, a process still used today [62].

Important in the context of this thesis was the development of the Ti:Saph laser as a solid-state, ultrashort-pulsed radiation source by Peter Moulton, then working at MIT. The system

provided significant greater pulse energy than colliding pulse ultrashort-pulsed laser sources could provide. In addition, it was also much easier to maintain and its footprint fitted onto a single optical table. Its commercialization by Schwartz Electro-Optics sparked new research and applications to investigate and utilize novel phenomena due to the femtosecond pulse duration.

Another major breakthrough for the use of lasers for material processing was in the 1990's with the development of diode-pump solid-state lasers. The market for high power laser sources for cutting and welding applications was previously dominated by CO_2 lasers [63]. Now Nd:YAG systems offered a serious competition, especially because they provided a much higher power efficiency with 20% "wallplug" efficiency [63] and better beam quality (up to diffraction limit) [63] than CO_2 lasers. The latter one is of great interest for welding applications since it allowed to focus the beam better on the target and therefore improved the control of the weld-seam [64].

With the turn of the century, fiber laser development greatly advanced. Even though the Ti:Saph laser source made laboratory deployment suitable, for industrial purposes the technology was too complicated and still too unreliable. With ultrashort-pulsed fiber laser systems penetrating the market, industrial deployment became suitable. High-precision micromachining was the application of choice, based on the greatly reduced HAZ when utilizing ultrashort-pulsed radiation. In addition, processes based on non-linear absorption like solar cell dicing or waveguide inscription first appeared using ultrashort-pulsed fiber laser sources. Today, fiber laser sources hold 18% market share of the $2 billion dollar revenue from laser application sector [65]. It is predicted that the fiber laser technology will continue to erode market segments hold by other laser technologies in the future.

2 THEORY OF LIGHT-MATTER INTERACTION

2.1 Classic Light-Matter Interaction

The physics involved in the interaction process between light and matter are majorly dependent on two parameters:

(a) the wavelength λ (or frequency ν) of the incident light, and

(b) the type of matter the light is incident on.

Most of work the presented here will consider light with a wavelength in the near infrared (NIR) and infrared (IR) regions between $800\,nm$ to $1064\,nm$ and $1.3\,\mu m$ to $2.4\,\mu m$, respectively. The conversion between wavelength and frequency of light is given by $\nu = \frac{c}{\lambda}$, with c the speed of light. The photon energy E_{photon} in terms of the wavelength can be calculated using

$$E_{photon} = \frac{hc}{e\lambda}[eV]$$

(2.1)

with h and e being Planck's constant, and the electron charge, respectively.

Regarding the types of matter, one can divide most of the known solid matter into three general groups:

- Dielectrics – containing no electrons in the conduction band,

- Metals – possess abundance of free electrons in the conduction band,

- Semiconductors – containing some electrons in the conduction band depending on their temperature and Fermi distribution.

In the following, the details of the interaction of light with these different groups will be discussed.

2.1.1   Energy Band Structure

Considering a single atom comprised of a heavy positive nucleus surrounded by light electrons, the electrons orbit the nucleus at discrete radii occupying so-called *energy shells*. The electrons in the outermost shell of such an atom are the weakest bound by nucleus, and thus are available to interact most strongly with neighboring atoms given enough energy to overcome the bond. Such electrons are called *valence electrons*.

When atoms form a solid, the different shells of atoms are split into very close energy levels to fulfill the requirements of Pauli's exclusion principle, which postulates that a particular energy state can only be populated once but with two different spins of the electron. The difference in energy of such split energy levels is so small that a continuum of permitted energies is formed, the so-called *energy bands*. The energy of these bands corresponds to that of the former energy shells. Since such shells had discrete energy values, there now exists a range of energy states between the bands, which are not permitted for electrons to occupy. This gives rise to the so-called *energy band gap* between the energy bands, here referred to as E_g. A simplified picture of the formation of energy bands and the band gaps is shown in Fig. 2.1.
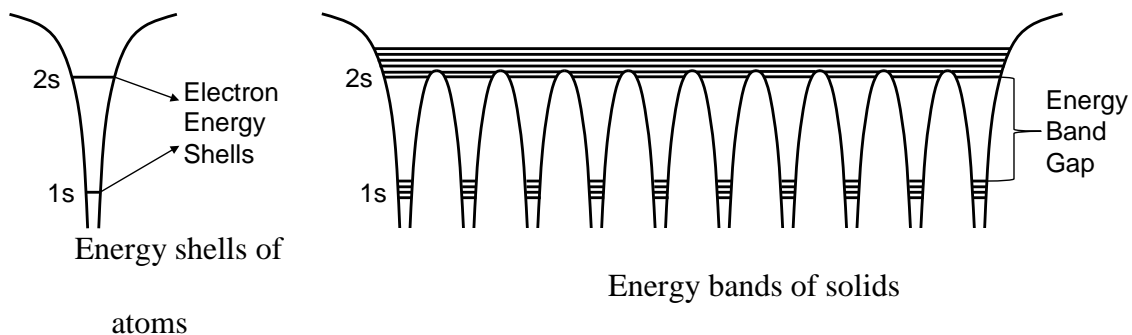
Fig. 2.1 - Scheme of energy shells and energy bands in atoms and solids

11

2.1.2 Interaction between Light and Atoms of Solids

As mentioned earlier, the propagation of light through a media is governed by the Maxwell Equ. (1.1) through (1.4) and hence by the wave-equation Equ. (1.5). A solution to the wave-equation is found for a wave with the field such that

$$\vec{E}(\vec{r},t) = \mathrm{E}_0 \cdot e^{i(\vec{k}\cdot\vec{r}-\omega t)} \tag{2.2}$$

Such light waves interact with matter through the polarization $\vec{\boldsymbol{P}}(\vec{\boldsymbol{r}},\boldsymbol{t})$ of the media the wave is propagating through. It describes the ability of the atoms in the matter to function as dipoles and follow the field. The most general form of the polarization can be given by [66]

$$\vec{P}(\vec{r},t) = \epsilon_0[\tilde{\chi}^{(1)}\vec{E} + \tilde{\chi}^{(2)}\vec{E}\vec{E} + \tilde{\chi}^{(3)}\vec{E}\vec{E}\vec{E} + \cdots] = \tag{2.3}$$

$$[\vec{P}^{(1)} + \vec{P}^{(2)} + \vec{P}^{(3)} + \ldots].$$

Here $\tilde{\chi}^{(N)}$ is the tensor of the susceptibility of the media. If the field strength of the wave is small, the higher order terms can be ignored and one finds the linear response of a media to light as

$$\vec{P}(\vec{r},t) = \epsilon_0 \tilde{\chi}^{(1)} \vec{E}. \tag{2.4}$$

In an isotropic media the susceptibility is a constant and thus the wave-equation simplifies to

$$\nabla^2 \vec{E} = \frac{1+\chi^{(1)}}{c^2} \frac{\partial^2}{\partial t^2} \vec{E}, \tag{2.5}$$

with $\frac{1}{c^2} = \mu_0 \epsilon_0$. If we rewrite the E-field of the propagating light wave for the propagation direction being the z-axis, we find a solution to Equ. (2.5) as

$$\vec{E}(z,t) = E_0 \cdot e^{i(K_z z - \omega t)}, \tag{2.6}$$

with $K_z = k_z + i\alpha_E$, the complex propagation constant in the z-direction. Taking into account that the relation between the field $\vec{E}(z,t)$ and the intensity of the wave $I(z,t)$ is given by $I(z,t) =$

$\sqrt{\frac{\epsilon_o}{\mu_0}}|\vec{E}^2|$, the absorption coefficient can be defined as $\alpha \equiv 2\alpha_E$. Further, the linear complex refractive index of a material $\tilde{n}(\omega)$ is then defined as

$$\tilde{n}(\omega) = \sqrt{1 + \chi^{(1)}} = n(\omega) + i\kappa(\omega), \qquad (2.7)$$

with $\chi^{(1)} = \chi^{(1)'} + i\chi^{(1)''}$, where $\chi^{(1)'}$ is the real part of the susceptibility and $\chi^{(1)''}$ is the complex part, $n(\omega)$ is the real refractive index of the media and $\kappa(\omega)$ is its absorptivity.

The frequency dependent reflectivity of a media $R(\omega)$ can be calculated as

$$R(\omega) = \left|\frac{\tilde{n}(\omega)-1}{\tilde{n}(\omega)+1}\right|^2 = \frac{(n(\omega)-1)^2 + \kappa(\omega)^2}{(n(\omega)+1)^2 + \kappa(\omega)^2}. \qquad (2.8)$$

2.1.3 Dielectrics

In a dielectric material, all electrons are bound to lattice atoms to a first approximation. In order to absorb incident photons in such a material, some electrons must be elevated to higher states than their present energy states. In wide-band-gap dielectrics, however, all energy states within the valence band are filled with electrons. Therefore to elevate an electron to a higher state, the band gap has to be bridged and the electron needs to be excited into the conduction band. Fig. 2.2 depicts such process known as linear absorption.
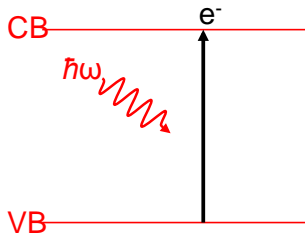
Fig. 2.2 - Linear absorption of incident photon from Valence Band (VB) into Conduction Band (CB)

The dependence of linear complex refractive index of dielectrics on the light frequency, or wavelength, is governed by the Lorentz-model [67]. It describes the resonances of the dipoles with respect to the light frequency based upon a harmonic oscillator model and the equation of motion of the bound electrons. Thus the linear complex refractive index for dielectrics can be modeled as

$$\tilde{n}(\omega) = \sqrt{1 + \frac{Ne^2}{m\epsilon_0} \frac{1}{\omega^2 - \omega_0^2 - i\Gamma\omega}}, \qquad (2.9)$$

with Γ the damping coefficient, also related to the absorption, of the media, by

$$n^2(\omega) + \kappa^2(\omega) = 1 + \frac{Ne^2}{m\epsilon_0} \frac{\omega^2 - \omega_0^2}{(\omega^2 - \omega_0^2)^2 - \Gamma^2\omega^2} = 1 + \chi^{(1)'}, \qquad (2.10)$$

$$2n(\omega)\kappa(\omega) = \frac{Ne^2}{m\epsilon_0} \frac{\Gamma\omega}{(\omega^2 - \omega_0^2)^2 - \Gamma^2\omega^2} = \chi^{(1)''}. \qquad (2.11)$$

For most dielectric materials it can be found that there are no resonances or absorption peaks in the spectral range investigated here, since their energy gap $E_g > 4\ eV$. However, if the photon energy of the incident light becomes large enough to allow absorption to take place, the absorbed intensity $I(z)$ with propagation distance z is given by Beer's Law as

$$I(z) = I_0 e^{-\alpha z} \left[10^{-4} \frac{W}{cm^2}\right], \qquad (2.12)$$

with I_0 being the initial intensity at the incident surface. Moreover, it can be found that the absorption coefficient α in Equ. (2.12) can be calculated as $\alpha = \frac{2\kappa\omega}{c}$.

It should be noted that this model is an idealized treatment of dielectrics. In practice a more complex picture should be applied, which will be discussed later Section 2.2.

2.1.4   Metals

Metals can be characterized as the opposite of dielectrics with regard to electron availability in the crystal lattice [68]; they possess an abundance of free electrons, often called the free electron

gas of metals. Due to this free electron gas, metals can be treated as plasma containing heavy, stationary ions (here the atoms of the metal lattice) and light electrons, which are free to move in the lattice.

2.1.4.1   Absorptivity and Reflectivity of Metals

Since the electrons move freely in the metal, there is no restoring force when an electromagnetic (EM) wave interacts with the electron cloud. Therefore, the refractive index model introduced by Lorentz must be modified by removing the restoring force term containing $\boldsymbol{\omega_0}$.This led to the Drude-model proposed by P.Drude in 1900 [69] as

$$\tilde{n}(\omega) = \sqrt{1 - \frac{Ne^2}{m\epsilon_0} \frac{1}{\omega^2 + i\gamma\omega}}.$$

(2.13)

In general, the reflectivity $R(\omega)$ given by Equ. (2.8) for metals follows the trend shown in Fig. 2.3. One can derive an expression for a frequency at which the reflectivity of metals changes significantly[67]. This frequency is known as the plasma frequency ω_p, indicated in Fig. 2.3 by the vertical red line, and can be calculated as

$$\omega_p = \left(\frac{Ne^2}{\epsilon_0 m_0}\right)^{1/2} \left[\frac{rad}{s}\right].$$

(2.14)
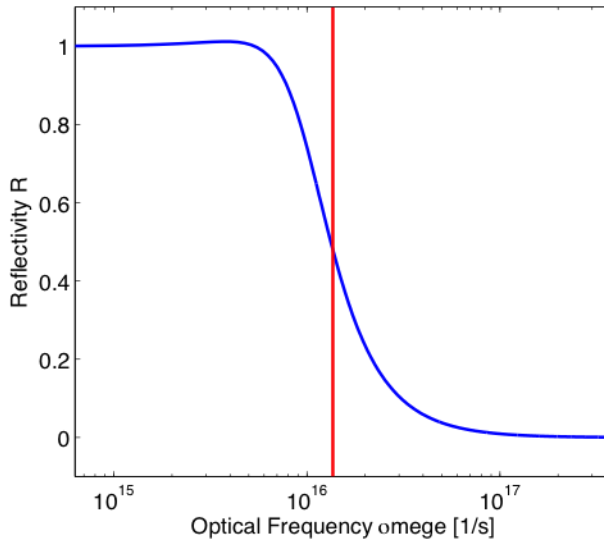
Fig. 2.3 - Graph of frequency-dependent reflectivity for a metal,

If the angular frequency of the incident electro-magnetic wave ω_i is less than the plasma frequency ω_p, the wave is fully reflected. If $\omega_i > \omega_p$, the reflectivity decreases sharply and the EM wave is transmitted through the metal.

2.1.4.1.1 Particle Picture

The full reflectivity of a metal can also be explained by a more intuitive interpretation of the interaction of the electron gas with an incident wave. In this picture, the electrons of the metal oscillate due to an incident EM wave on the metal surface. However, due to the Maxwell Equations boundary condition on the material interface, only the orthogonal part of the incident wave with respect to the interface is allowed to penetrate the metal surface. That causes the electrons to oscillate only parallel to the surface. When a charge is accelerated and decelerated, it emits radiation in a donut-like pattern with no emission in the direction of its motion and maximum emission in the orthogonal direction to its axis of motion. Since the electron gas consists of numerous charges, which all radiate in a donut-like shape but are dislocated slightly from each

16

other, one can show that the reemitted waves from the electrons only interfere constructively in one direction orthogonal to the metal surface. Due to a rapid exponential decay of the field strength inside the metal, the complete energy must be reflected back from the metal. The superposition of that reflected wave and the parallel part of the incident wave with respect to the interface cause the known trajectories of reflected light waves on metal surfaces (Fig. 2.4).
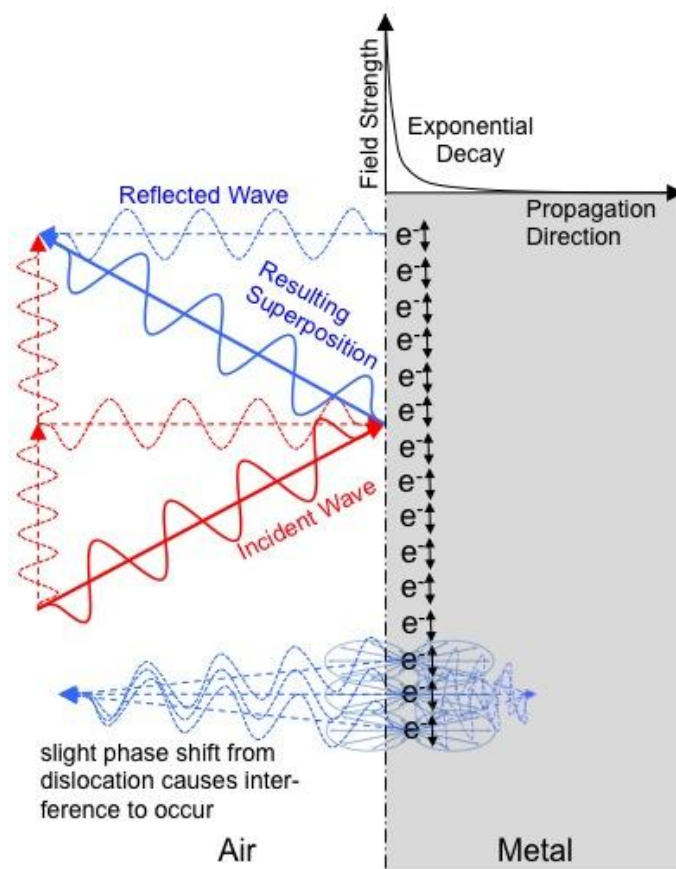
Fig. 2.4 - Scheme of reflection on metal surface due to electron oscillation from incident wave

2.1.4.1.2 Electron Scattering Time

The electron scattering time τ, defined as the average time between collision of electrons with impurities or phonons [70], is difficult to measure directly. However, it is the limiting parameter

17

of the electrical conductivity σ of a material, which is much less difficult to measure. Therefore, measuring the electrical conductivity offers a simple method of determining the electron scattering time.

The AC conductivity of metals is given by [67]

$$\sigma(\omega) = \frac{\sigma_0}{1 - i\omega\tau} \left[\frac{S}{m}\right]. \qquad (\,2.15\,)$$

Here σ_0 is the DC conductivity given as [67]

$$\sigma_0 = \frac{Ne^2\tau}{m_0} \left[\frac{S}{m}\right], \qquad (\,2.16\,)$$

with N being the free electron density of metals. This number is equal to the number of atoms in a unit volume of the particular metal (in the order of 10^{28} m^{-3}) multiplied by its valency, the number of allowed bonds to form for that metal. For most metals, as well as semiconductors, the electron scattering time τ is in the range of 10^{-14} to 10^{-13} seconds.

2.1.4.1.3 Skin Depth

The field strength of an EM wave will decay exponentially within a metal in order to satisfy the boundary conditions of the Maxwell Equations. This phenomenon is known as the skin effect of metals. The skin depth is the characteristic distance in which the field strength of the incident EM wave decays to a value of e^{-1} of its initial value. If an approximation for low frequency $\omega\tau \ll 1$ is valid, the skin depth can be calculated as [67]

$$\delta = \sqrt{\left(\frac{2}{\sigma_0 \omega \mu_0}\right)} \; [m], \qquad (\,2.17\,)$$

with $\mu_0 = 4\pi \times 10^{-7} \, H/m$ being the magnetic permeability of free space.

2.1.5   Semiconductors

Considering some important modifications, the light-matter interaction in semiconductor materials can be treated similar to the interaction in metals. The band structure of a semiconductor material differs slightly from that of a metal. Even though the conduction band is similar, the valence band contains holes. Holes are electronic state vacancies in the lattice structure, of which three types have been defined [71], light (*lh*) and heavy (*hh*) hole bands, and the split-off (*SO*) hole band. The *lh* and *hh* bands connect at $k = 0$ but each possesses a different dispersion. The *SO* band does not connect with the *lh* and *hh* bands as a result of spin-orbit interaction and is split-off by an energy Δ_0. In contrast to metals, these hole bands modify the structure of the valence band as shown in Fig. 2.5.

Additionally, the electron mass used in the free electron model of metals has to be adjusted to account for the presence of holes when applying this model to semiconductors. The effective mass has been reported in many references [72].
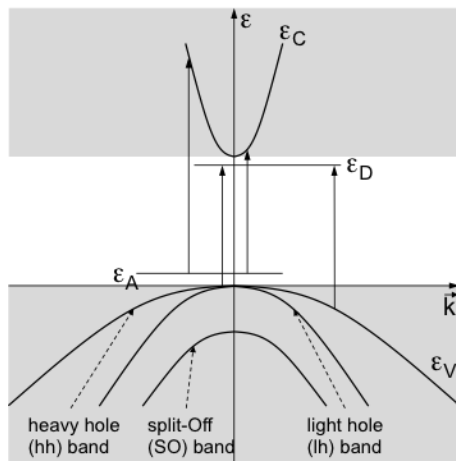
Fig. 2.5 – Figure of the band structure of a semiconductor containing light and heavy holes

In a semiconductor, intervalence band transitions are possible between the *lh* and the *hh* band, the *SO* and the *hh* band as well as the *SO* and the *lh* band. These transitions do not require a change of momentum of the hole and therefore are a highly probable mechanism for the absorption of incident light. A schematic picture of that absorption process is shown in Fig. 2.6(a). On the contrary, the intraband excitation of free electrons requires a change in momentum and is therefore only possible with the occurrence of a scattering event, depicted in Fig. 2.6(b). Both of these effects are known as free carrier absorption and occur in the NIR and IR above ω_p, where the material is expected to be transparent.
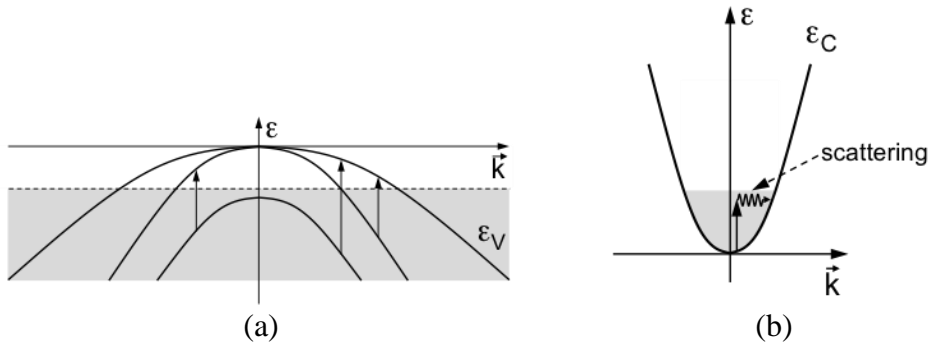
Fig. 2.6 – Figure of (a) intervalence transitions due to light absorption and (b) intraband transitions of free carriers

The complex refractive index $\tilde{n}$ of a semiconductor can then be expressed using a modified free electron model given as [67]

$$\tilde{n}(\omega) = \sqrt{\varepsilon_{host}(\omega) - \frac{Ne^2}{m_e^*\varepsilon_0}\frac{1}{\omega^2+i\gamma\omega}},$$

(2.18)

with $\varepsilon_{host}(\omega)$ and m_e^* being the dielectric constant of the host material in the transparent region and the effective electron or hole mass, respectively. In most semiconductor $\varepsilon_{host}(\omega)$ can be

assumed to be $n^2_{transparent}$ due to $\kappa = 0$ in this spectral region. From that one can deduce the free carrier absorption coefficient assuming $\omega\tau \gg 1$ as

$$\alpha_{free\ carrier} = \frac{Ne^2}{m_0^* \varepsilon_0 nc\tau} \frac{1}{\omega^2}. \qquad (2.19)$$

Equ. (2.19) depicts the ω^{-2}-dependence of the free carrier absorption, which is also depicted graphically in Fig. 2.7(a). In addition, due to the presence of free carriers, the reflectivity can hit zero in the mid-IR region, depicted in Fig. 2.7(b).

(a)   (b)
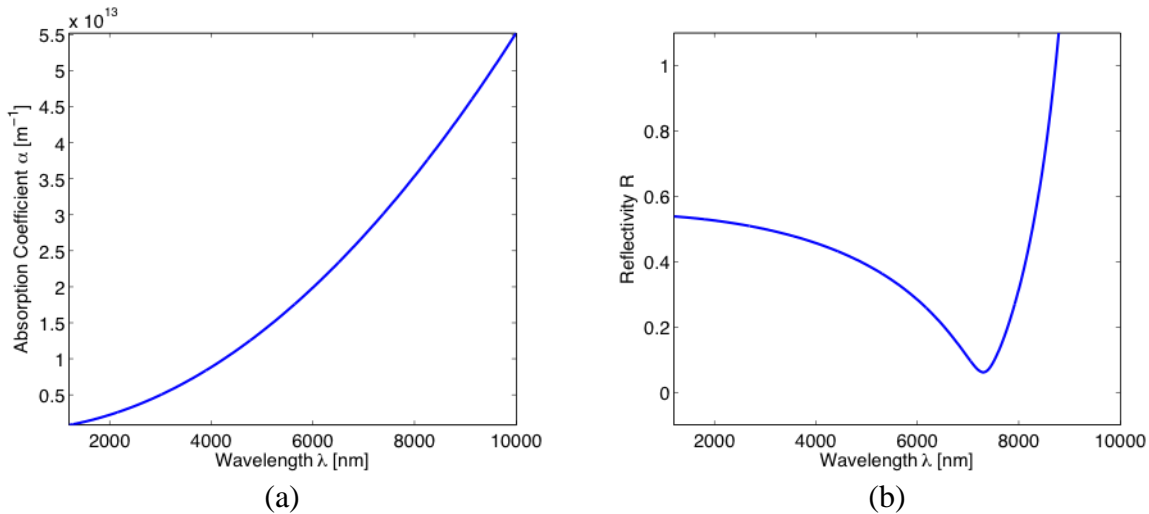
Fig. 2.7 - Graphs of (a) the free carrier absorption coefficient and (b) the reflectivity as a function of wavelength for Silicon with a dopant concentration of $10^{25}\ m^{-3}$

Aside from interband and free carrier absorption, another absorption mechanism exists in semiconductor materials, namely impurity absorption. This absorption denotes the transition of a free charge from donor or acceptor levels of induced dopants into the conduction band. The energy gap here is a few tens of milli-eV's, which is on the order of room temperature energy levels.

2.2   Ultrafast Light-Matter-Interaction

The development of the Ti:Saph femtosecond laser based chirped pulse amplification (CPA) by Mourou in 1985 [73] generated a renewed research initiative into ultrafast light-matter interaction after some limited initial research using colliding pulse lasers earlier. The new laser was easier to build and to maintain than previous employed ultrashort-pulsed colliding-pulse dye lasers. It also generated more pulse energy at shorter pulse durations and could be deployed as a tabletop system. In the following section the light-matter interaction process is explained for such ultrashort laser pulses. In this short-pulse-regime the interaction phenomena have to be reconsidered. One, the intensity levels are sufficiently high to enable non-linear processes. Two, the pulse-durations are on the same time scales as the interaction times of the fundamental constituents of the matter.

2.2.1   Ultrafast Material Response

The general time scale of ultrashort material processing is on the order of a few picoseconds or less. Such pulse durations are in the range of fundamental interaction times of the constituents of matter itself [74]-[76], such as electron-electron and electron-phonon interaction, as illustrated in Fig. 2.8.
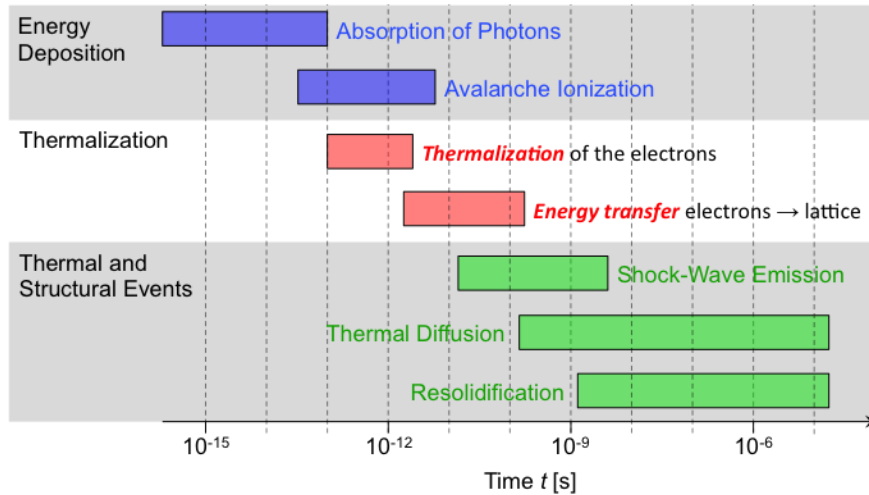
Fig. 2.8 - Time scale of typical events due to ultrafast laser irradiation of matter[74], [75], [77]

As illustrated in Fig. 2.8, thermal and structural events in the material are temporally decoupled from the deposition of energy, thus enabling a non-thermal material-processing regime.

2.2.2   Non-linear Absorption Processes

Looking beyond the temporally dependent material response (compare Fig. 2.8), ultrashort pulsed lasers are capable of producing ultra-high peak powers (in the order of GW peak power) and consequently, non-linear phenomena, such as non-linear absorption, take place. Such non-linear absorption of photons in the focal region of a beam has enabled new processing techniques as first reported by Davis *et al.* [7] and Mazur *et al.* [78] in 1996 for the modification of bulk dielectrics. The techniques rely solely on the non-linear absorption in the focal volume, which was not possible with longer pulsed radiation, as compared in Fig. 2.9.

Besides such applied research initiatives in bulk modification of transparent dielectrics, the general field of fundamental light-matter interaction science [55], [79], [80] as well as ultrafast

23

laser material ablation [81] has been studied in further detail due to the availability of the Ti:Saph

CPA laser system.

(a)   (b)
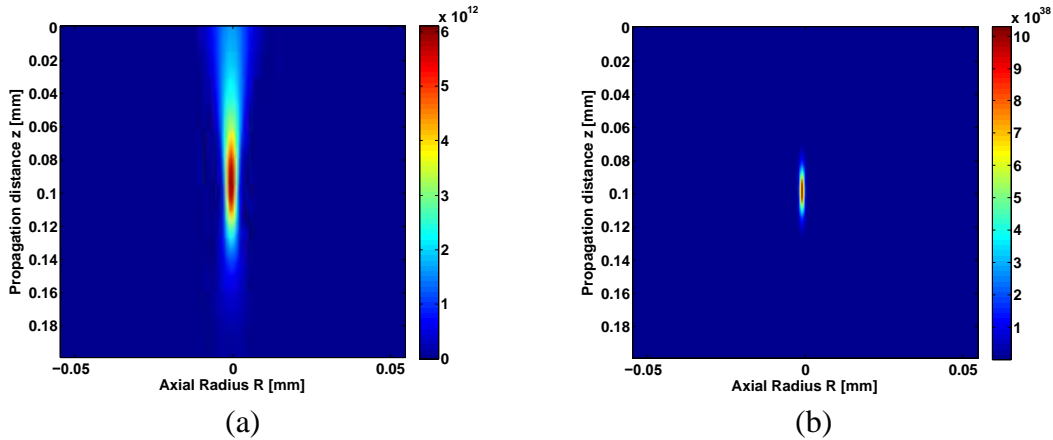
Fig. 2.9 – Simulated laser-induced electron density due to linear (a) vs. non-linear (b)

absorption in Fused Silica, incident beam propagates from top to bottom and is focused

with 20X NA 0.4 objective and a pulse energy E_p of 1 μJ

2.2.2.1   Nonlinear Refractive index

Following the invention of the laser, the constant scaling of peak intensities (and

corresponding optical frequency electric field) over the last half century has forced

(mathematically) a more rigorous approach to the treatment of fundamental optical properties.

Especially the polarizability of a material to an incident optical field and the experienced refractive

index have to be reconsidered.

With the exception of some non-centrosymmetric crystals, most materials possess a

centrosymmetry [66]. Therefore, when material polarization is expressed as a series expansion, the

second order term has to vanish[2], which simplifies Equ. (2.3). At intensities beyond $10^{12}\frac{W}{cm^2}$, higher than third order terms are generally negligible, hence the polarization can be expressed as

$$\vec{P}(z,t) = \epsilon_0 \left[\tilde{\chi}^{(1)} + \tilde{\chi}^{(3)} |\vec{E}(z,t)|^2 \right] \vec{E}(z,t).$$
(2.20)

The tensor characteristic of the susceptibility can be dropped for most media, thus the higher order expression for the complex refractive index is given as [66]

$$\tilde{n}(\vec{E}) = \sqrt{1 + \chi^{(1)} + \frac{3}{4}\chi^{(3)}|\vec{E}|^2}\,.$$
(2.21)

This result can be expanded to

$$n(I) = 1 + \frac{1}{2}\chi^{(1)} + \frac{3}{8}\chi^{(3)}I$$
(2.22)

using a power series and considering the linear terms. From the previously introduced relation, Equ. (2.7) , it can be found that the refractive index can now be expressed as

$$n(I) = n_0 + n_2 I(z,t)\,,$$
(2.23)

where n_0 is the linear refractive index of the medium and $\boldsymbol{n_2}$ is the intensity dependent nonlinear refractive index of the medium.

2.2.2.2 Critical Self-Focusing

Critical self-focusing is caused by the intensity dependence of the non-linear refractive index as introduced in Equ. (2.23) and the spatial (commonly Gaussian) intensity profile of the laser beam. In such cases, it becomes apparent that the center of the beam experiences a higher

---

[2] $P^{(2)} \rightarrow -P^{(2)}; E \rightarrow -E;$ but $\chi^{(2)} \rightarrow \chi^{(2)}$ [82]

$$-P^{(2)} = \epsilon_0 \chi^{(2)}(-E)\cdot(-E) = P^{(2)} \rightarrow \chi^{(2)} \equiv 0 \rightarrow P^{(2)} = 0$$

instantaneous refractive index than the peripheral parts of the beam, which is equivalent to passing through a positive lens.

The critical power for self-focusing P_{cr} if defined as the power at which a balance between self-focusing and diffraction of a propagating pulse is achieved. If the incident power exceeds the critical power, $P_{cr} < P_{incident}$, catastrophic damage occurs in the sample material. The critical power can be calculate as [66]

$$P_{cr} = \frac{\pi(0.61)^2\lambda_0^2}{8n_0 n_2} \tag{2.24}$$

Catastrophic self-focusing is especially a challenge in semiconductor materials, since the non-linear coefficients in these materials are much larger than in dielectrics.

2.2.2.3 Non-linear Absorption

The absorption of NIR laser energy by a wide-band-gap dielectric, where the photon energy is less than the band gap energy of the material, relies on non-linear processes. In such case, several photons must be absorbed simultaneously to promote an electron from the valence band into the conduction band. Since the electron can occupy only virtual states in-between the valence and conduction band, the photons have to be incident within the Rayleigh scattering time of the electron, on the order of approximately 5 fs. In general, the rate for the occurrence of such process is very low. However, at intensity levels readily achievable using ultrashort-pulsed irradiation, the process becomes sufficiently efficient. The equation governing the process is given as [83]

$$\frac{dI(z)}{dz} = -\sum \alpha_k I_0^k, \tag{2.25}$$

with α_k being the non-linear absorption coefficient of the kth order necessary to overcome the band gap. A very similar equation can be found for the rate of free electron generation as

$$\frac{dN_{PI}(t)}{dt} = \sigma_k I(t)^k, \tag{2.26}$$

with σ_k the kth order absorption cross-section coefficient.

Depending on the specific laser wavelength and light intensity, one of two non-linear absorption mechanisms dominates: multi-photon ionization (MPI), depicted in Fig. 2.10(a), or tunneling ionization, Fig. 2.10(b). In the case of MPI, several photons are absorbed simultaneously to bridge the energy band gap. For tunneling ionization the incident photons distort the electron's Coulomb well, therefore giving rise to a finite probability that the electron tunnels through the barrier according to its wave function.

(a)   (b)
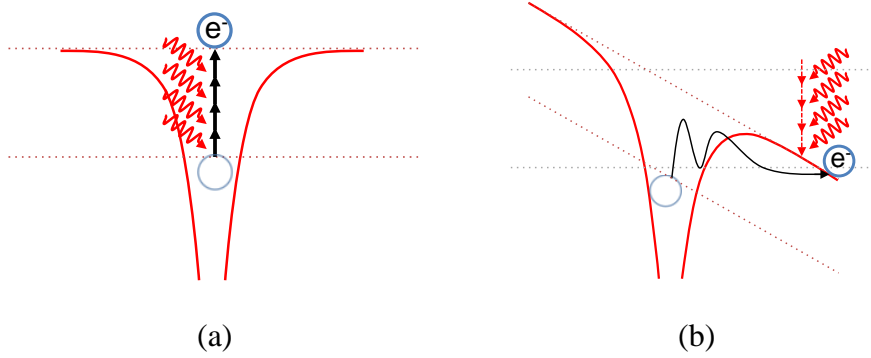
Fig. 2.10 – Scheme of multi-photon ionization (MPI) (a) and tunneling ionization (b)

The Keldysh parameter [84] predicts which of the two absorption mechanisms, MPI or tunneling ionization, is most probable. It is given by

$$\gamma = \frac{\omega}{e}\left[\frac{m_e c n \epsilon_0 E_g}{I}\right]^{1/2}, \tag{2.27}$$

with m_e, n, ϵ_0 and E_g being the effective mass of the electrons, the refractive index of the material, the free space permittivity, and the band gap energy, respectively. In general, MPI occurs for a Keldysh parameter value above 1.5 and tunneling ionization for a value less than 1.5. Fig. 2.11 depicts the Keldysh parameter for different wavelengths in silicon (solid lines) and Fused

Silica (doted line) for common focal intensities. The horizontal black line denotes the value of 1.5. As the graph clearly shows, for longer wavelength, as well as smaller bandgap energies, the ionization shifts from MPI ($\gamma > 1.5$) towards tunneling ionization ($\gamma < 1.5$). In the intermediate region around a Keldysh parameter of 1.5 a combination of both is also possible [85].
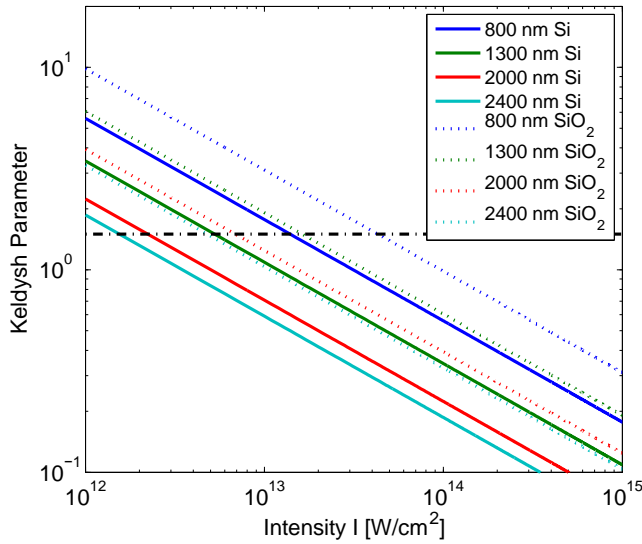
Fig. 2.11 - Graph of the Keldysh parameter for common focal intensities in Si (solid lines) and SiO₂ (doted lines)

If there are free charge carriers available in the material avalanche ionization can occur. That is, an electron sequentially absorbs a sufficient number of photons to acquire enough energy to promote another electron from the valence into the conduction band by impact ionization. The initial free charge carriers, also called 'seed' electrons, originate from either photo-ionized electrons from the leading edge of the pulse, impurities in the material or lattice error. The rate of electron generation due to avalanche ionization is [85]

$$\frac{dN_{aval}(t)}{dt} = \alpha I(t) N(t), \qquad (2.28)$$

where α is the avalanche ionization coefficient. The process is schematically shown in Fig. 2.12. Here the requirements on the absorption conditions are more relaxed, in that the photons can be absorbed sequentially and do not need to have the same wave vector.
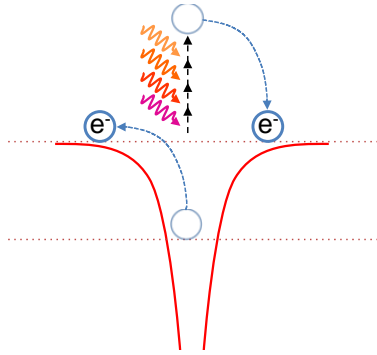
Fig. 2.12 - Schematic of impact ionization mechanism

The absorption of ultrafast laser radiation often involves at least two of the previously described processes. MPI or tunneling ionization can provide seed electrons in the conduction band for avalanche ionization to follow. Therefore, the total rate of free electron generation, $W(t)$, can be written as the sum of both ionization types

$$W(t) = \frac{dN(t)}{dt} = \sigma_k I(t)^k + \alpha I(t) N(t). \tag{2.29}$$

Due to the short temporal duration of the incident radiation the involved processes are non-equilibrium processes. Therefore special care has to be taken when applying approximations and models developed for longer pulse or cw-radiation.

2.2.2.4 Non-linear Propagation and Absorption Model

It is of great interest to predict the electron density in the focal volume due to an incident focused laser pulse. For that purpose a propagation and absorption model was developed using the previously introduced Equ. (2.23) and (2.29). A common approach for such model is based on

the Split-Step Beam Propagation Method (BPM). A significant number of publications can be found using such method or a variation [86]-[88]. However, common to such approach is a paraxial approximation for the z-propagation of the pulse, restricting its validity to low numerical aperture focusing conditions.

To allow for high numerical aperture focusing, a method based on the complex beam parameter was developed. Essentially, the beam path was calculated first based on the focusing geometry, and then an ultrashort pulse propagating in time and space was superimposed. At each step in time the non-linear interaction processes were calculated. The technique is limited to Gaussian beam. In addition, even though self-focusing was accounted for, diffraction and defocusing due to the generated electrons were ignored. The model also accounts for plasma reflection of off the electron cloud and electron recombination.

Fig. 2.13(a) depicts the estimated electron density N_e at the end of the pulse using this method in the bulk of Fused Silica. The focusing objective had a numerical aperture of 0.65, the pulse energy was $E_p = 1\,\mu J$ at a center wavelength of $\lambda_c = 800\,nm$, the pulse duration was $\tau = 100\,fs$, and the physical focusing depth was set to be $t_f = 100\,\mu m$.
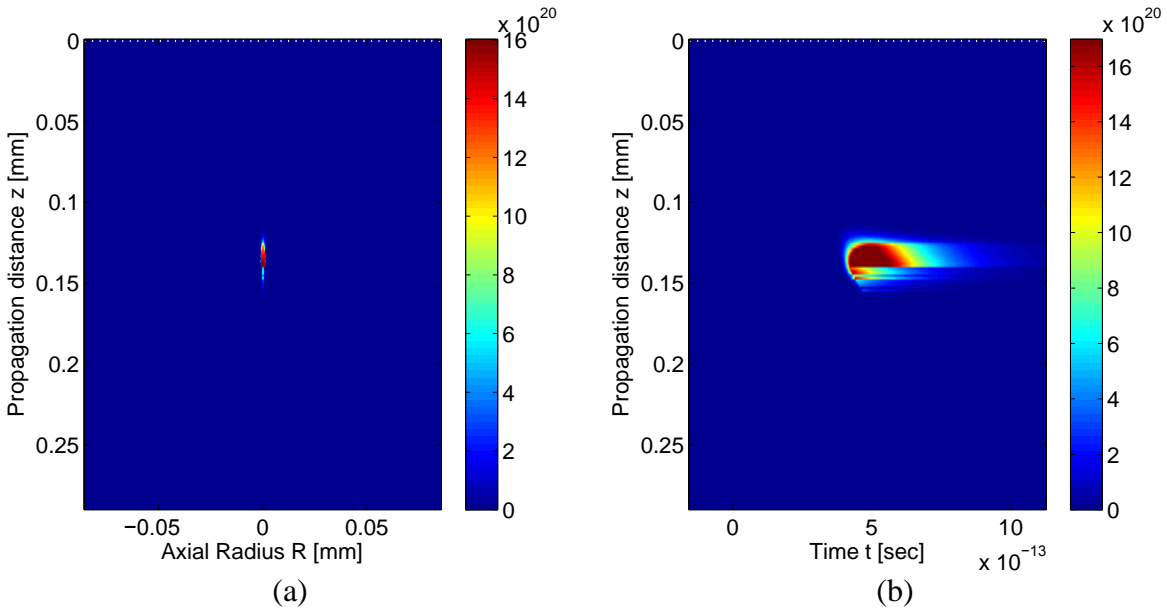
Fig. 2.13 - Graphs of the simulated electron density in a Fused Silica sample due to ultrashort pulse irradiation

The generation of electrons only occurs in the focal volume, as Fig. 2.13(a) indicated. The maximum electron density during the pulse duration reached $N_e = 3.5 \cdot 10^{21} \ cm^{-3}$. In addition, Fig. 2.13(b) predicts the temporal profile of the electron density, here depicted for the axial position $r = 0$ position. Clearly apparent in this graph is the onset of plasma reflection at a propagation distance of approximately 140 μm. Moreover, the simulation also reveals the percentage of absorbed energy of the incident pulse, here approximately 2.3% through photoionization and approximately 6.5%, for a total of 8.8% of the incident energy. This also illustrates that photoionization provided the seed-electron for the following avalanche ionization because no impurities were present at the start of the simulation.

2.2.3 Laser-Plasma Interaction Mode

2.2.3.1 Plasma Absorption and Reflectivity

During the irradiation of wide-band-gap materials, non-linear absorption processes create an electron-plasma within the focal volume. The interaction of this plasma with the incident laser field can be described using the Drude-model [70]. This model can also describe the light interaction in doped semiconductors that inherently contain free electrons in the conduction band. The major difference between the Drude-model for the description of metals and the one considered for the generation of a free electron plasma is its electron density, and therefore the specific plasma frequency of each. As shown in Fig. 2.3, the plasma frequency of most metals is in the UV region of the spectrum. Using Equ. (2.14) one can easily see, that the plasma frequency during the generation of the laser-induced plasma shifts, as illustrated in Fig. 2.14.
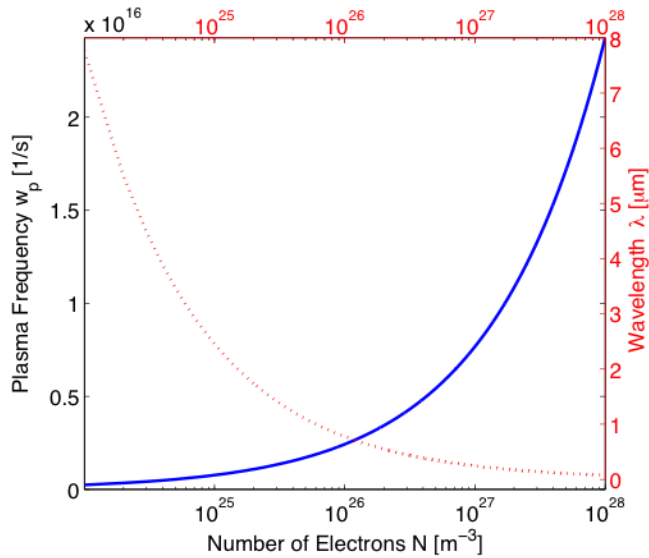
Fig. 2.14 - Graph of the plasma frequency ω_p as a function of electron density

In a similar fashion one can calculate the reflectivity of such laser-induced plasma at a given laser wavelength, shown in Fig. 2.15. It becomes apparent, that the reflectivity of the plasma

increases significantly for higher electron densities. The point at which the reflectivity reaches unity is known as the critical plasma density.
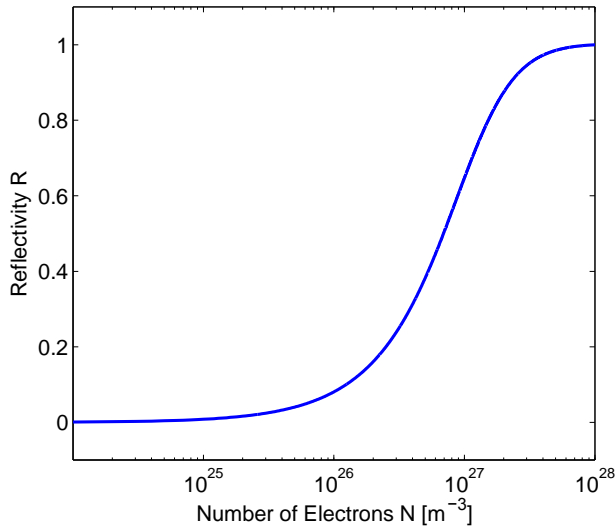
Fig. 2.15 - Graph of the plasma reflectivity R as a function of electron density N at a given laser wavelength of $2.4\ \mu m$

When the critical plasma density is reached, the incident radiation is entirely reflected, and therefore, within this simple model, the plasma cannot absorb any further energy from the incident beam. However, because of inherent plasma density gradients, laser energy will be absorbed within the peripheral plasma regions where the density is lower. The propagation length within this below critical density region is sometimes called the 'scale length' of the plasma.

2.2.3.2 Two-Temperature-Model

Within the regime of ultrashort pulse durations investigated here, the initial energy exchange between the incident laser radiation and material occurs solely within the electron system, as illustrated in Fig. 2.8. Therefore we are interested in the temperature evolution of the electron system throughout the laser pulse duration. The excited electron system will relax by interacting

with the lattice through electron-phonon relaxation. During the relaxation process the electron temperature T_e decreases while the lattice temperature T_L increases. For ultrashort laser pulses, this process takes place mainly after the laser pulse has passed. The temperature dependence of the two systems can be modeled using the Two-Temperature-Model (TTM), first introduced for metallic materials by Kaganov, Lifshitz and Tanatarov in 1956 [89]. It was later refined for the use with ultrashort laser radiation in dielectrics by Anisimov *et al.* [90], since there is no initial electron bath available in such materials. The TTM is given as set of couple differential equations [91]

$$C_e(T_e)\frac{\partial T_e}{\partial t} = \nabla[k_e(T_e) \cdot \nabla T_e] + S(z,t) - G(T_e - T_L),\qquad (2.30)$$

$$C_L(T_L)\frac{\partial T_L}{\partial t} = G(T_e - T_L),\qquad (2.31)$$

with C_e and C_L as the specific heat of the electron and lattice system, respectively.

Here $\nabla[k_e(T_e) \cdot \nabla T_e]$ describes the Drude-like model of the plasma, $S(z,t)$ denotes the source term, describing the energy absorption due to the incident laser pulse, and $G(T_e - T_L)$ is the coupling term between the electron and lattice system. Using the TTM, a simple illustration of the temperature evolution of electrons and lattice due to ultrashort laser pulses is shown in Fig. 2.16.
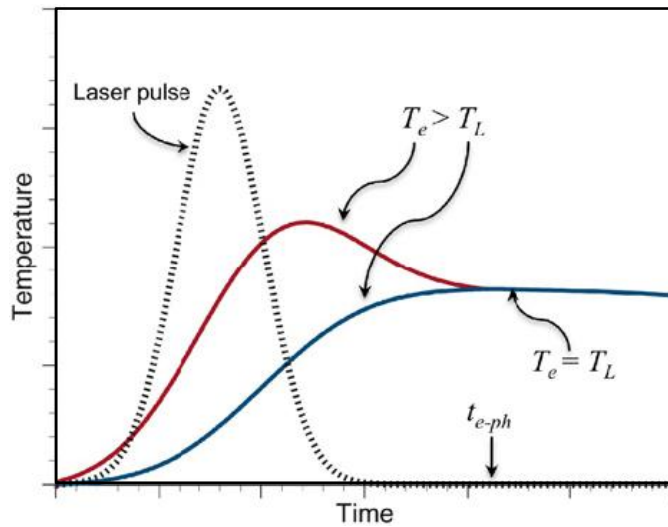
Fig. 2.16 - Schematic graph of the temperature evolution of electron and lattice system due to an ultrashort laser pulse using the Two-Temperature-Model [adapted from [92]]

2.2.4   Thermal vs. Athermal Material Interaction

In a steady state situation in which a photon beam is incident on a material, the classical laws of thermal conduction apply. In such a case, three principal mechanisms of thermal interaction could occur sequentially: heating of the lattice; melting of the heated region, and boiling and evaporation of the matter. The phase diagram in Fig. 2.17 shows the various possible transitions, the green arrow depicts the case of classical heat conduction. In a macroscopic picture, thermal energy transfer, thermal conduction or heat flow will occur from the point of the incident energy towards the surrounding material. Thus, after an initial transient state an equilibrium conditions will take place between incident energy and energy dissipation from the incident into the surrounding region. This type of light-matter interaction is a solely thermal interaction process and governed by the laws of classical thermo-dynamics.
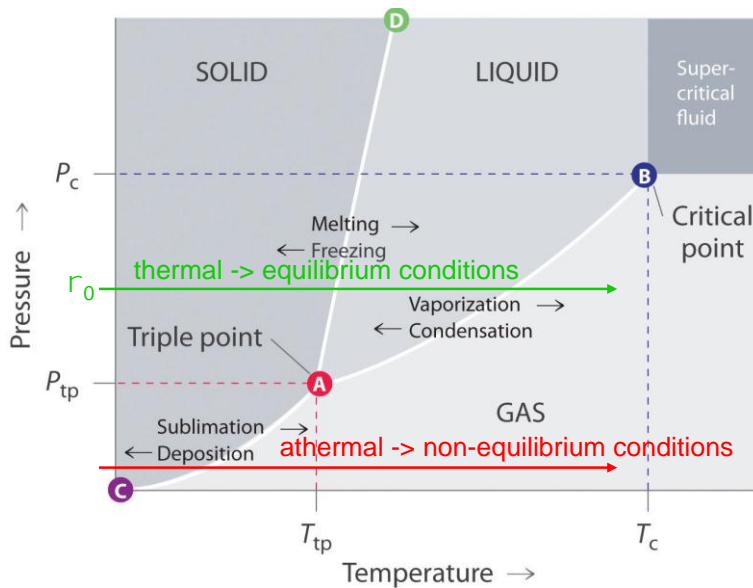
Fig. 2.17 - General phase diagram of three-phase matter [adapted from [93]]

The collision time between electrons and atoms of the material lattice is on the order of 10^{-14} to 10^{-12} seconds. If the pulse duration is on the order of or shorter than the collision time, the equilibrium state will not take place during the pulse duration and therefore the classical laws of thermo-dynamics do not apply. In such case transient phase changes may occur such as solid to vapor transition. The process is known as athermal interaction between light and matter. In general, athermal interaction is considered for material processing using ultrashort laser pulses.

2.2.5   Material Surface Interaction Mechanisms

Material ablation and surface structuring was one of the first applications of lasers in industry and is still a major application field of laser material processing. For example in many industrial environments, metal cutting and welding relies on *cw-* and long-pulsed laser systems.

Ultrafast laser radiation has unique advantages when interacting with matter, which opens new horizons, especially in material processing. The extremely high peak intensities enable the processing of new materials like ceramics or composite compounds, which are difficult to process

otherwise using conventional techniques. Such processes will be discussed in more detail in the following section.

2.2.5.1   Material Surface Modification Thresholds

A surface threshold behavior can be defined for either modification or ablation with respect to an incident optical density, the so-called fluence. A distinction between modification and ablation has to be drawn here since modification of the material can be achieved without material removal, i.e. by melting a surface layer. Below this modification threshold fluence the material is essentially unchanged[3]. When the threshold fluence is reached however, permanent modification can be introduced. Fig. 2.18 shows an example of a modified and ablated area on the surface of an intrinsic Silicon surface after ultrashort laser irradiation. The image on the left hand side depicts a microscope image of the region recorded at 100X magnification; the right one depicts the measured topological profile of the irradiated area. It is apparent that the material is ablated in the center region but surrounded by a region that is photo-expanded and therefore only modified.

---

[3] It should be pointed out that an accumulative effect of several pulses below threshold fluence could still lead to permanent modification of the material.
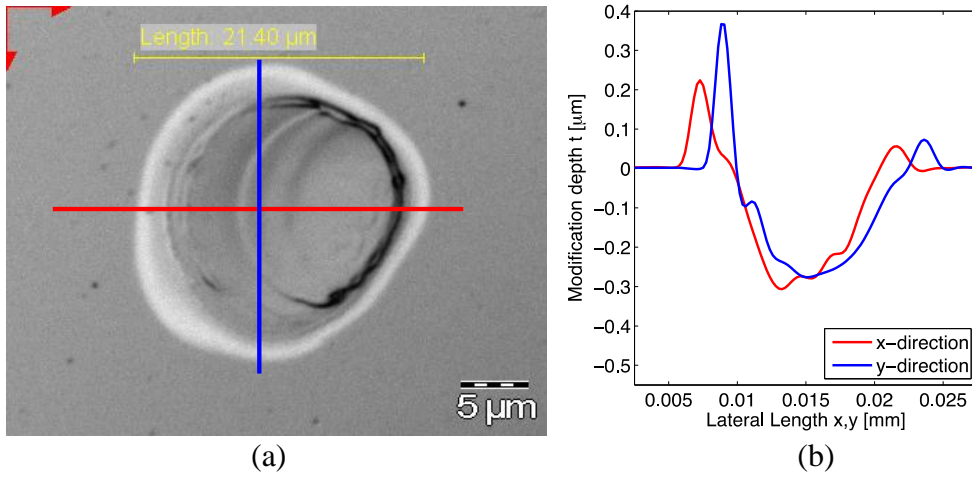
Fig. 2.18 - (a) 100X light microscope image of an ablation spot on an intrinsic Silicon surface resulting from ultrashort pulsed irradiation; (b) measured surface profile of the same spot [adapted from [94]]

A common technique to determine the modification/ablation threshold of a material is described by Liu[95]. We adapted this technique for measurements of the modified area at varying incident fluences. The following equation describes the relation between such measured area and the laser fluence

$$A(F) = \frac{\pi}{2}\omega_0^2 \cdot \ln\left(\frac{F}{F_{th}}\right),$$

(2.32)

with F_{th} and ω_0 as the threshold fluence and the beam radius at the focus. In a double-logarithmic plot, this equation presents a straight line that can be fitted (blue line), returning the values for the beam radius and the threshold fluence. An example plot is shown in Fig. 2.19. The surface modification/ablation threshold depends strongly on the type of material (solid, dielectric, metal or semiconductor) as well as the pulse duration and laser wavelength.
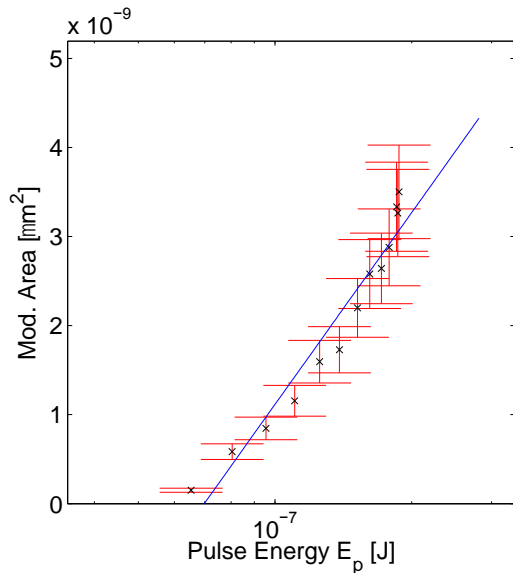
Fig. 2.19 - Graph of fitted threshold fluence for modification, here for Fused Silica

In the case of dielectric materials, ultrashort laser radiation introduced a different interpretation of ablation and modification thresholds. With longer laser pulses ($\tau > 10\ ps$), the threshold values are most commonly determined statistically since the energy absorption process is dominated by heating of conduction-band electrons at defect sides followed by avalanche ionization and energy transfer to the material lattice [96]. The advent of ultrashort laser radiation allowed direct ionization of valence band electrons into the conduction band by multi-photon-ionization without the need of a defect site, which led to a more empirical threshold value for modification/ablation [55], [80]. Ultrashort radiation also changed the understanding of the light-matter interaction process for semiconductor materials. For *cw* and long pulse irradiation, the interaction phenomena of this type of solid were interpreted separately from dielectrics and metals. When using ultrashort radiation, however, semiconductors can be interpreted as metallic materials (see Section 2.2.3), because their interaction behavior is similar to such in the ultrashort-pulsed regime [97].

Another important aspect of ablation or surface structuring is the penetration depth of the radiation from the surface into the material. Two generally different cases have to be considered when dealing with ultrashort laser radiation. For dielectrics it can be stated that the absorption depth depends strongly on the focusing geometry. Therefore, absorption[4] will take place in a region where the local field intensity is strong enough to allow non-linear absorption processes to take place. On the contrary, in metals the penetration depth is small, given by the wavelength dependent skin depth of the material (Equ. (2.17)). In the case of semiconductors, the previously applied approximation for skin effect $\omega\tau \ll 1$ breaks down and a modified expression has to be found. The understanding of the process, however, is still very limited since almost no research has been conducted so far.

2.2.5.2 Material Ablation

Material ablation occurs when matter is either directly removed by material disintegration following energy deposition and thermodynamic relaxation phenomena or indirectly by means of an established plasma at the material surface. In the former case, the ionization process on the surface generates free electrons, which can be ejected from the material quickly into the surrounding space due to their high velocity, leaving behind positively charged matter. If the charge is strong enough, the remaining matter will non-thermally explode, giving rise to a so-called Coulomb Explosion [97]. This phenomenon has so far only be observed with dielectric

---

[4] It is assumed that the incident photon energy is insufficient to directly bridge the energy band gap and therefore interband absorption will not occur.

materials, since metals and semiconductors posses a natural bath of free electrons neutralizing the repulsive force of the positive charges of the remaining matter.

Beyond the electronic ejection of matter from the irradiated spot, there is also a thermal process, which allows melt expulsion and vaporization of matter. Its characteristic time scale is much larger than in the case of Coulomb Explosions because the lattice has to be thermalized first, see Fig. 2.8. For ablation, however, the slow thermal processes have lower ablation rates compared to ultrashort pulse ablation [75], [98]. The ejection mechanism is also different for ultrashort and longer pulsed radiation. It has been shown that for femtosecond pulses, the process is driven by direct solid-plasma transition [4], [81]. An illustration of the general mechanisms of the energy deposition and material removal process is shown in Fig. 2.20(a). Nevertheless the phase change of the ejected material is directly from solid to plasma, a very thin molten layer in between the two phases exists. The graph in Fig. 2.20(b) depicts the thickness of the expected molten layer in aluminum as a function of time for varying laser fluences.

In the case of nanosecond or longer pulses the material has sufficient time to fully thermalize and therefore sequentially passes through all phase states as depicted in Fig. 2.17. The material ejection here is mainly driven by boiling and evaporation from a liquid phase [80], [81]. Therefore the molten layer is much thicker than for ultrashort pulse laser ablation.
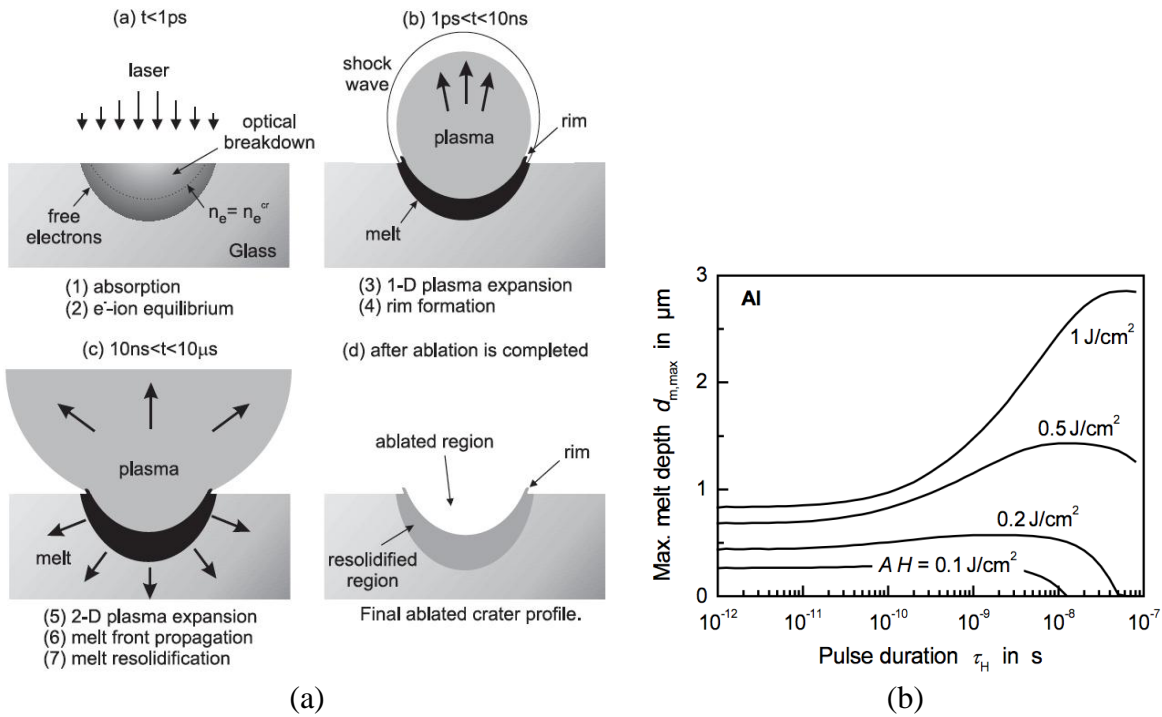
Fig. 2.20 – (a) Schematic illustration of physical processes during laser material ablation with ultrashort laser pulses [adapted from [99]]; (b) expected melt layer thickness of aluminum for ultrashort pulse laser ablation and varying laser fluences [adapted from [100]]

The short interaction time of ultrashort radiation with matter decouples the energy deposition and the thermal dissipation processes of the deposited energy within the material lattice. Moreover, since the phase of the material changes directly from solid to plasma, there is virtually no melt ejected at the ablation site that would redeposit on the surface. This results in an appreciable reduction of the heat-affected-zone (HAZ) surrounding the ablated region and hence a decrease in achievable feature size [81], [98]. Examples of surface ablation on dielectrics with femtosecond and nanosecond pulses are shown in Fig. 2.21. In both processes approximately the same fluence was used to irradiate the sample.

(a)	(b)
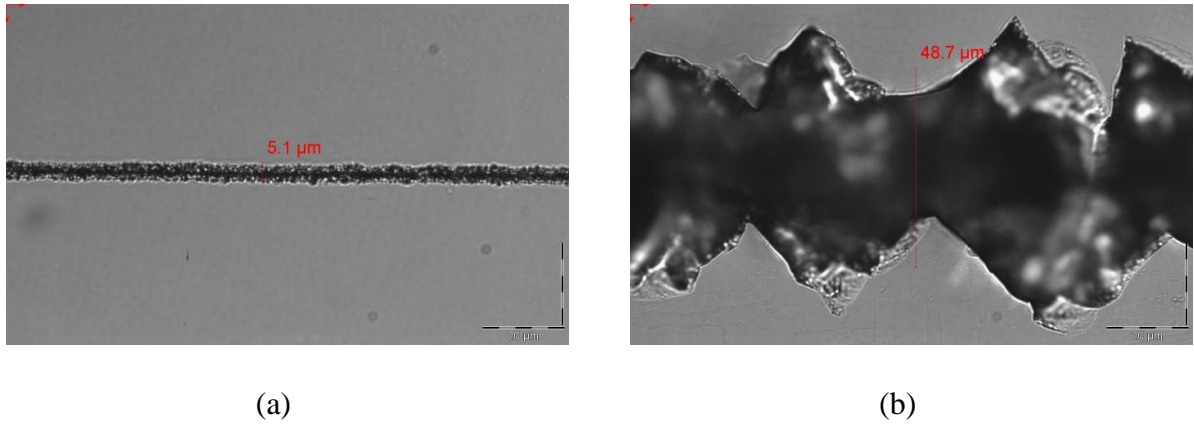
Fig. 2.21 – Image of a ablation track on a dielectric material surface using a microscope objective with a NA 0.5 and laser radiation with the fluence of approximately $F = 100 \, J/cm^2$, (a) femtosecond laser radiation, (b) nanosecond laser radiation [adapted from [101]]

The large intensity inherent to ultrashort radiation enables one to process at dimensions smaller than the diffraction limit of light. This can be achieved by tailoring the parameters of the incident radiation in a way such that only the peak of the Gaussian field exceeds the threshold for modification/ablation will in return also reduce the achievable feature size [102], as shown in Fig. 2.22.
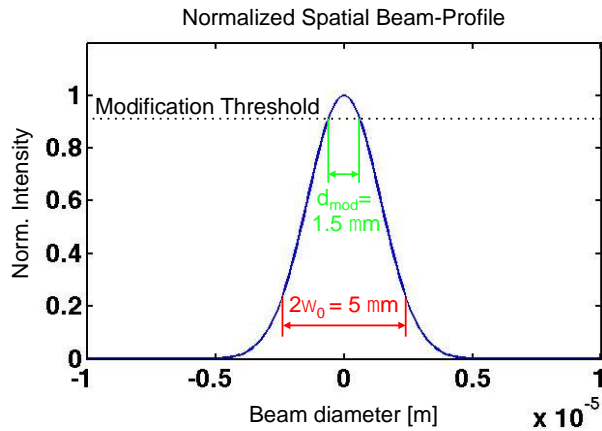
Fig. 2.22 - Reduced modification diameter due to modification threshold when using ultrashort radiation [adapted from [101]]

Plasma etching is rather uncommon using ultrashort lasers since an effective heating of the plasma cannot be achieved using such laser systems. It should however be pointed out that the generation of a plasma on the surface can reduce the efficiency of the direct ablation processes since the plasma can shield the material from the incident energy [103].

2.2.5.3 Surface Texturing

Besides ablation, surface texturing or patterning is an important field, as it can influence how a material interacts with its surroundings. A commonly used example for motivating such laser-based material texturing is the Lotus effect, a naturally occurring phenomena in which nano-structures prohibit water and dirt from adhering on the surface of Lotus flower leaves. When irradiating a surface with ultrashort radiation, periodic nanostructures can be generated as well, often called ripples or LIPSS for Laser Induced Periodical Surface Structures. These ripple structures possess periodicities well below the incident wavelength as opposed to their counterparts generated using longer pulsed laser radiation [104]-[106]. The origin of these structures generated with ultrashort radiation has yet to be fully understood, though several

44

theories are being developed at this time [107]-[109], and their fabrication requirements have been well studied.

2.2.6   Material Bulk Interaction Mechanism

Non-linear absorption in the focal region allows for local modification in bulk of transparent material. This technique, introduced by Davis [7] and Mazur [78], was quickly adopted by numerous researchers to fabricate 3D devices. It is based on the local laser-induced modification of the refractive index or the lattice structure in amorphous or crystalline dielectrics, respectively. Three typical modification regimes have been generally accepted by the research community (Table 2-1).

Table 2-1 - Laser modification regimes in transparent dielectrics

Type I	Type II	Type III
Isotropic refractive index change (amorphous dielectrics)	Anisotropic refractive index change (amorphous dielectrics)	*Void formation* (amorphous and crystalline dielectrics)
→ Δn isotropic with positive or negative sign → Fusion and non-uniform solidification	→ Alternations of positive and negative Δn at sub-wavelength scale ("nano-gratings") → Birefringent formation	→ Low-density core (Δn<0) embedded in a denser shell (Δn>0) → Explosive expansion of the hot electrons and ions → Nano-cracks or amorphization in the focal volume

Several causes for these modifications have been suggested, though agreement about their contribution to the overall modification does not yet exist within the research community. Among such causes are the reordering of bonds [110], the generation of defects, namely self-trapped excitons (STE), followed by the generation of non-bridging oxygen-vacancies (NBOHC) [111], the generation of color centers (E' centers) [112], [113], and the redistribution of material constituents [114]. The induced change in refractive index depends on the particular material, ranging from 10^{-1} in Chalcogenides to 10^{-4} in Fused Silica. Since the modification is limited to the focal region of the incident beam, a translation of the sample relative to the focal spot allows the generation of 3D structures in the material. A general schematic of the 3D ultrafast laser writing technique is shown in Fig. 2.23.

Nowadays a broad variety of applications for such techniques exist, from fabrication of waveguides in various transparent dielectrics [115]-[117], integrated photonic circuits such as beam splitters [118]-[121], to active optical components like amplifiers or even waveguide lasers [10], [122]-[124]. It should be pointed out that there are no reports on non-destructive direct refractive index change in crystalline dielectrics. Nevertheless, using nano-cracks, an effective negative refractive index change can be induced.

The above-described modifications can also influence the susceptibility to etchants, either due to chemical material changes or due to increased surface area, as in the case of nano-cracks. Thus, the fabrication of microfluidic devices has been reported using 3D ultrafast laser writing combined with post-process etching[125].

46
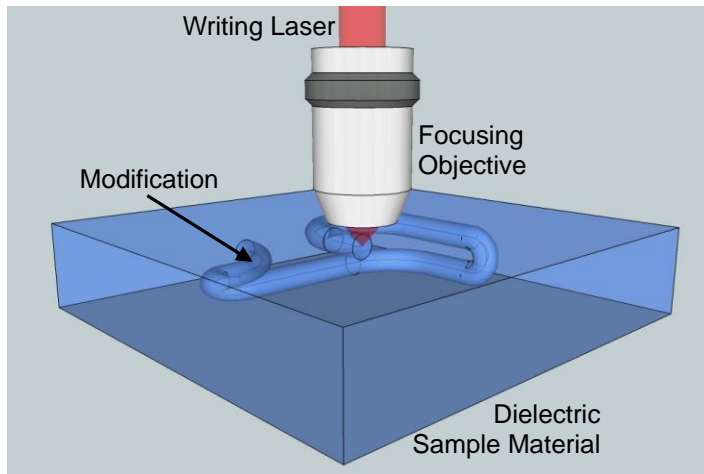
Fig. 2.23 - Schematic of 3D ultrafast laser writing in transparent material

2.2.7   Heat-Accumulation

2.2.7.1   The Mechanism of Heat-Accumulation

An important advantage of ultrashort laser radiation is the reduction of the HAZ due to the decoupling of energy deposition and energy dissipation by thermal conduction, as depict in Fig. 2.24.
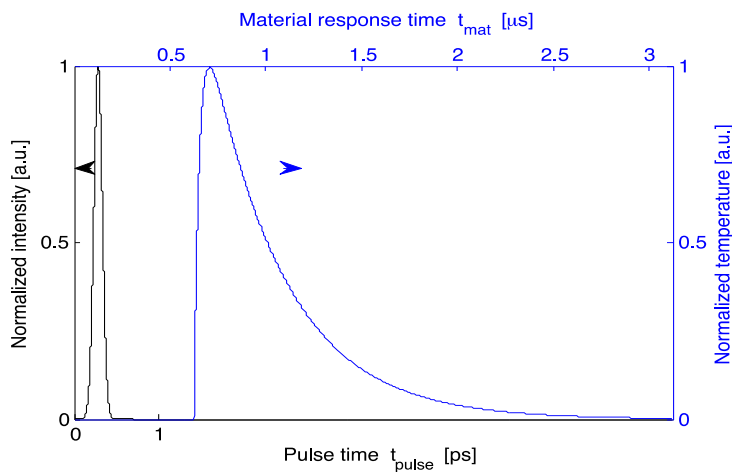
Fig. 2.24 – Model of energy deposition and thermal material response; black curve represents the incident pulse (bottom scale) and the blue curve represents the thermal response time of the material due to the incident pulse [adapted from [101]]

47

If the repetition rate of the laser increases to the point at which the period between pulses is shorter than the energy dissipation time of the material, than heat will build up in the focal volume. This process is referred to as heat-accumulation (HA). This heat build-up can be very significant, allowing the local temperature in the voxel to rise to several thousand Kelvin, as reported by several researchers [126]-[128]. The material properties are of significant influence for this process. Not only the dissipation time of the induced energy in the material but also the melting point of the bulk material influences the effect HA has during the irradiation process. Due to the high local temperature originating from HA, the effect is usually easy to recognize during the irradiation process in transparent[5] media because it is accompanied by a strong white light emission, as compared to the emission from the electron plasma also seen during irradiation. The exact origin of this emission is not yet known, but believed to result from the blackbody radiation of a hot object in the focal volume in this case. An example of such emission is depicted in Fig. 2.25.
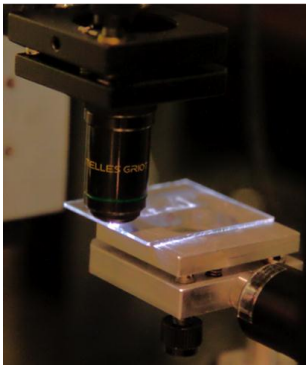
Fig. 2.25 – White glow of HA during the irradiation of dielectric material with high repetition rate ultrashort pulses [adapted from [101]]

---

[5] to visible light

2.2.7.2 Heat Accumulation Model

To predict the thermal response of a material, a model has been developed based on spherical 1D time-variant heat diffusion equation [127]

$$\frac{\partial}{\partial r}\left(r^2 \frac{\partial T(r,t)}{\partial r}\right) = \frac{r^2}{D} \frac{\partial T(r,t)}{\partial t}, \tag{2.33}$$

with r, $T(r,t)$, and D being the radial position from the center of the focal volume, the space- and time-dependent temperature and the heat diffusion coefficient of the material. The assumption of a spherical expansion is valid because the heat-affected volume is much larger than the focal volume of the tightly focused beam.

The difficulty however, is the estimation of the initial temperature. As mentioned previously, the energy deposition into the material from a single incident pulse occurs through the electron system on a time scale of few hundred femtoseconds. The time-scale for heat-accumulation effects is much longer than the light-matter interaction process. Therefore, a valid prediction of the initial temperature cannot be based on the TTM. For this HA model, energy conservation between the absorbed energy and the thermal energy available for the initial temperature was assumed. Furthermore, the thermal energy input was assumed to be a Dirac impulse in time, modeling the ultrashort laser pulse. The spatial distribution of the initial temperature profile was set to be spherically Gaussian, resulting from the Gaussian energy profile of the focused beam. Therefore the initial temperature change is given by [127]

$$\Delta T(r, t = 0) = \frac{E_0}{C_p \rho} \oint_0^\tau exp\left\{\frac{r^2}{w_0^2}\right\}, \tag{2.34}$$

with E_0, C_p, ρ, and τ as the normalization coefficient between the absorbed energy and the spherical volume integral, the specific heat capacity and density of the material, and the pulse

duration, respectively. The beam waist w_0 was calculated from the NA of the focusing optic assuming diffraction limit using

$$w_0 = 1.22 \frac{\pi\lambda}{NA}.$$

(2.35)

Fig. 2.26 depicts the temperature evolution in space and time according to the developed model for Fused Silica. Fig. 2.26(a) shows the material response to a single laser pulse with a pulse energy of $E_p = 500 \ nJ$, Fig. 2.26(b) illustrates the thermal accumulation and diffusion of 50 of such pulses at the repetition rate of $f_{rep} = 500 \ kHz$. The model clearly indicates the rise of the peak temperature due to the storage of energy in focal volume.

(a)   (b)
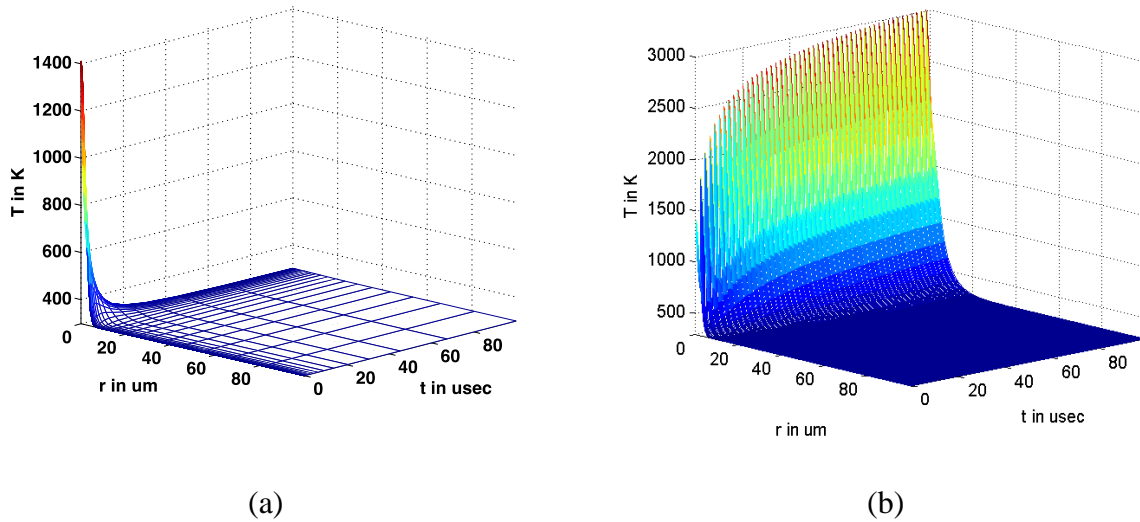
Fig. 2.26 - Heat diffusion based on 1D time-variant model; (a) single pulse with an energy of $500 \ nJ$, and (b) 50 pulses at $500 \ kHz$ repetition rate with an energy each of $500 \ nJ$ in Fused Silica

2.2.7.3 Advantages and Disadvantages of Heat-Accumulation

There are several advantages when utilizing HA in ultrafast material processing. An established field of application is the inscription of material modification inside dielectrics for light

guiding structures, commonly referred to as waveguide-writing but not limited to just waveguides. Traditionally, index modifications were introduced into dielectrics using low rep. rate laser systems, since such systems were available at the advent of ultrafast laser material processing (UFLMP). The shape of the introduced modification, however, is highly dependent on the energy distribution in the focal volume, which leads to elongated modifications. Such are not ideal for wave-guiding, as a more radially symmetric shape would be appreciable [129]. Using the high rep. rate regime with the HA effect allows for a radially-symmetric shape, since the modification is driven by the thermal melting from the center of the irradiated volume [128]. Moreover, it has been shown that the absolute value of index change introduced using the HA effect can be significantly higher than in the low rep. rate regime [128]. In addition, simply due to the increased repetition rate in the HA regime, processing times for the inscription of photonic devices can be reduced dramatically [130].

Drawbacks of the HA effect include an increased HAZ. In some applications the local melting within the central focal region is disadvantageous since it negates other desirable features. For example, for selective etching applications, nano-gratings are required to increase the etch-ratio of the irradiated area with respect to its surrounding [131]. Here, HA would erase the nano-gratings due to the material melting process.

3 LASER SOURCES FOR ULTRASHORT MATERIAL PROCESSING

In this section challenges and limitations are discussed that arise due to the laser sources employed in material processing with ultrashort pulses. A closer look will be taken at the generation of IR wavelengths between $1\ \mu m$ and $2.6\ \mu m$ using optical parametric amplification.

3.1 Generation of Ultrashort Pulsed

3.1.1 Low Repetition Rate Laser Sources

The main laser source used in this study was a SpectraPhysics Spitfire system. This laser system is a Master-Oscillator-Power-Amplifier (MOPA) layout based on CPA [132], [133]. Nano-joule pulses were generated at tens of MHz repetition rate from a passively mode-locked master oscillator. The output pulses from the oscillator are then stretched in a grating stretcher, pulse picked and amplified in a power amplifier laser system, and finally recompressed in a grating compressor assembly. A general schematic of the system is shown in Fig. 3.1.

The output wavelength λ_{center} of this Ti:Saph-based laser system [51] was centered at $810\ nm$. The pulse-generation method in the master oscillator is based on Kerr-Lens mode-locking, providing ultrashort pulses with a measured pulse duration of $\tau = 70\ fs$ and an energy of approximately $E_p = 3.5\ nJ$ per pulse. The output beam was horizontally polarized owing to the presence of a Brewster-cut crystal and Brewster-cut prisms in the laser cavity. The repetition rate of the oscillator was measured to be approximately $f_{rep} = 84\ MHz$ given by the length of its cavity with $L = 1.78\ m$ due to the round trip time as

$$f_{rep} = \frac{c}{2L}\ [Hz] \qquad (3.1)$$

The pulse stretcher and compressor were based on a Martinez [134] and a Treacy [135] design, respectively.
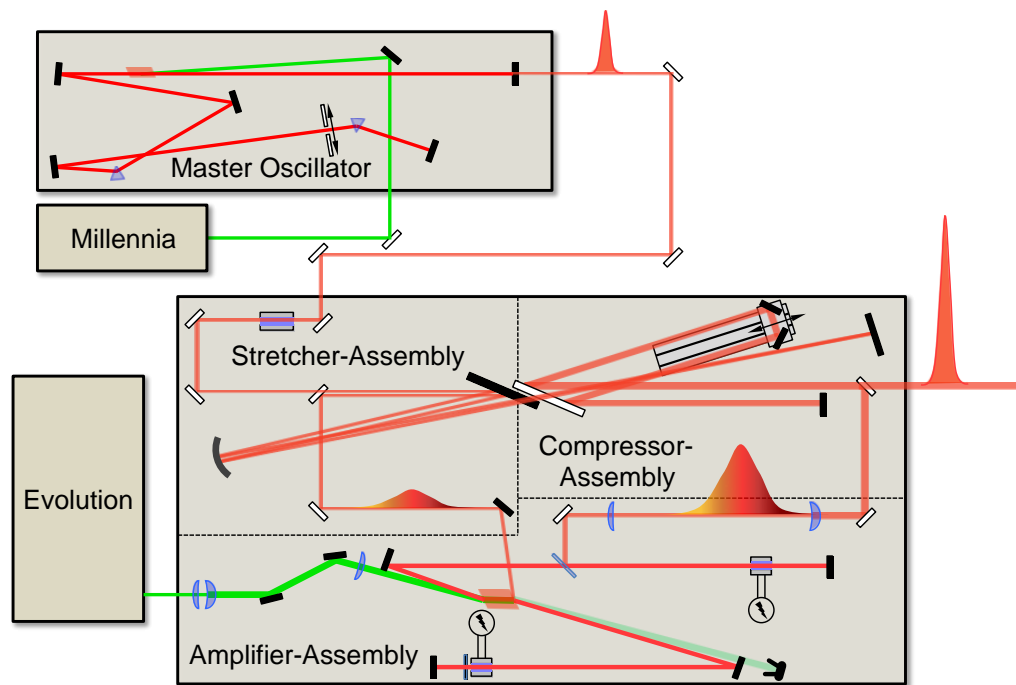
Fig. 3.1 – Schematic of SpectraPhysics Spitfire laser system

The repetition rate is reduced to 1 kHz before amplification. There are two reasons for the reduction of the repetition rate. One, the amplification process is accomplished by passing the stretched pulsed several times through the gain medium in amplifier cavity, which reduces the maximal possible repetition rate. Second, and most important, the thermal load on the optics would cause thermal lensing and eventually damage if the desired pulse energy would be achieved at the full oscillator repetition rate. Pulse-picking was accomplished using a fast switching Pockels cell inserted in the amplifier cavity, which in its high-state rotates the polarization of the beam. A second fast-switching Pockels cell also inserted in the amplifier cavity outputted the pulse after the amplification process. The repetition rate of the amplifier output can be adjusted by changing the trigger rate of the Pockels cells. The output repetition rate can be set using the following formula

$$f_{rep\,final} = \frac{1000\ Hz}{M} \qquad\qquad (3.2)$$

with M being an integer number. The pulse duration after compression has been measured to be approximately 100 fs time-bandwidth limited. The Spitfire output spectrum was measured using an OceanOptics HR2000 spectrometer and is shown in Fig. 3.2. The achievable pulse energy at the compressed output of the CPA laser system was $1\ mJ$.
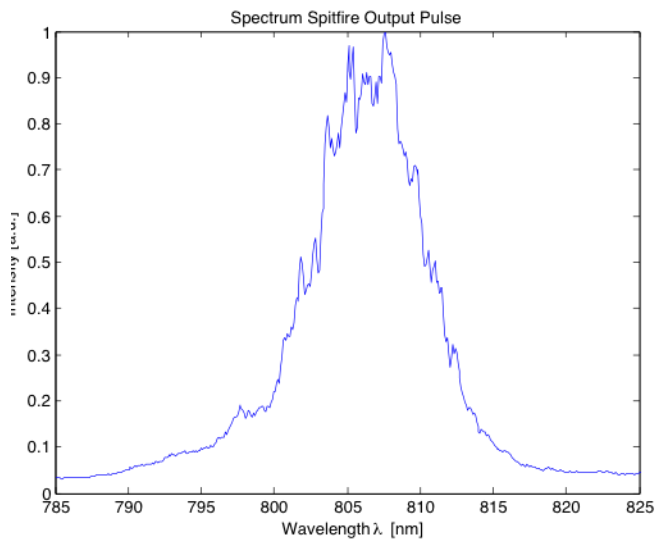
Fig. 3.2 - Spectral content of $100\ fs$ output pulse from Spitfire laser system

The beam profile at the Spitfire output was recorded using a Spiricon SP-980M beam profiler camera. The profile is slightly elliptical, as depicted in Fig. 3.3. The elliptical shape results minuscule astigmatism at the output of the amplifier cavity, mainly due to the position axial position of the pump beam focus inside the gain crystal. The long propagation through the compressor made the ellipticity visible in the beam profile. Further optimization of the beam profile after the output could be realized using a spatial filter or relay imaging a pinhole, however this technique did not enhance the achievable processing results in the past.

The compressed output beam is also passed through an external fast shutter with a switching time of $3.4\ ms$. The shutter was synchronized with the laser and thus allowed for single shot operation of the laser system.
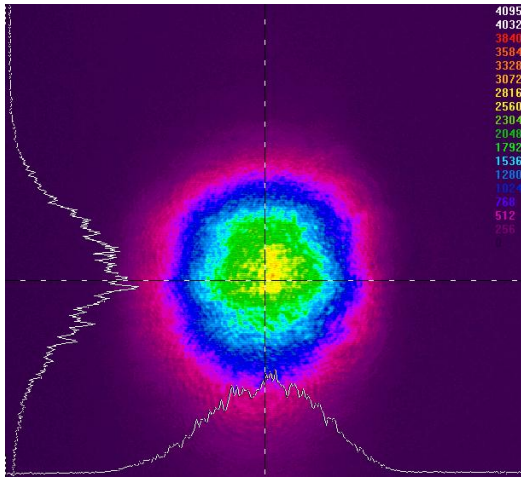
Fig. 3.3 - Measured beam profile of the Spitfire laser

3.1.2   Generation of IR Ultrashort Pulses

The Spitfire laser provides pulses with a center wavelength $\lambda_{center} = 810\ nm$. Non-linear techniques were required to generate pulses with center wavelength in the IR between $1\ \mu m$ and $2.6\ \mu m$. Parametric down-conversion of the $800\ nm$ pulses is required to reach the desired IR spectral range beyond $\lambda_{IR\ start} \geq 1100\ nm$. The process used to achieve this down-conversion is optical parametric amplification using the Spitfire laser as a pump source. A commercial Optical Parametric Amplifier (OPA) by Coherent (OPerA X) is used to generate pulses with a center wavelength variable in the range between $1150\ nm$ and $2630\ nm$. Due to the nonlinear conversion of the pump pulse one expects the mid-IR output pulse energy to be significantly less than the input pulse energy. In the past the employed setup achieved a conversion efficiency of approximately 10% in the signal beam and 8% in the idler beam, providing IR pulse energies

around one order of magnitude lower than the input pump pulse energy. The theory of DFG is detailed in the next section.

3.1.2.1 Nonlinear Frequency Generation

As established before, nonlinear effects can be utilized to generate sum and difference frequencies of light beam. Here the theory of such conversion is detailed.

Starting at Equ. (2.3) and using an optical field such as [66]

$$\tilde{E}(t) = E_1 e^{-i\omega_1 t} + E_2 e^{-i\omega_2 t} + c.c., \tag{3.3}$$

one can determine the occurring frequency components for second-harmonic, sum-frequency and difference-frequency generation by investigating the second order polarization term $\tilde{P}^{(2)}(t) = \epsilon_0 \chi^{(2)} \tilde{E}(t)^2$ as

$$\tilde{P}^{(2)}(t) = \epsilon_0 \chi^{(2)} [E_1^2 e^{-2i\omega_1 t} + E_2^2 e^{-2i\omega_2 t} + 2E_1 E_2 e^{-i(\omega_1 + \omega_2)t} +$$

$$2E_1 e^{-i(\omega_1 + \omega_2)t} + c.c.] + 2\epsilon_0 \chi^{(2)} [E_1 E_1^* + E_2 E_2^*]. \tag{3.4}$$

From this equation it becomes apparent that the terms of for second-harmonic, sum-frequency, difference-frequency generation and optical rectification are given by

$$P(2\omega_1) = \epsilon_0 \chi^{(2)} E_1^2$$

$$P(2\omega_2) = \epsilon_0 \chi^{(2)} E_2^2$$

$$P(\omega_1 + \omega_2) = 2\epsilon_0 \chi^{(2)} E_1 E_2 \tag{3.5}$$

$$P(\omega_1 - \omega_2) = 2\epsilon_0 \chi^{(2)} E_1 E_2^*$$

$$P(0) = 2\epsilon_0 \chi^{(2)} (E_1 E_1^* + E_2^* E_2^*)$$

3.1.2.2 Phase-Matching in Collinear Geometry

The concept of phase-matching can readily be understood when considering the case of a two-wave interaction, as follows. Nevertheless, the same concepts are valid for a three-beam wave interaction such as OPA implemented in the OPerA.

The refractive index of a medium $n(\omega)$ is dependent on the EM-wave frequency. Thus it becomes clear that the newly generated frequency ω_2 will experience a slightly different refractive index than the initial frequency ω_1. Therefore the accumulated phases of each beam will start to walk-off with propagation distance. However, the initial beam will still cause the generation of light at ω_2, which now will be out of phase with previously generated light at ω_2. The worst case becomes when the phase of the two frequencies is off by $\frac{\lambda}{2}$, since at that point the intensity of light at ω_2 decreases to 0, due to destructive interference. Hence phase-matching between the initial and generated light beam has to be achieved. In general phase-matching can be accomplished by angular tuning of an birefringent crystal so that [66]

$$\frac{1}{n_e(\theta)^2} = \frac{sin^2\theta}{\tilde{n}_e^2} + \frac{cos^2\theta}{n_o^2} \tag{3.6}$$

Since in the here used OPA the beams were propagating collinear, only this case is considered. Thus phase-matching can only be accomplished over short propagation distances z, or by using a technique called quasi-phase-matching. For quasi-phase-matching the nonlinear medium is stack in a way that the refractive index positively and negative shifts the phase of the generated light so that a step-like increase in generated light intensity can occur due to the absence of destructive interference.

3.1.2.3   Difference Frequency Generation (DFG)

In general, DFG is equivalent to optical parametric amplification, with the difference that for DFG the pump and the signal or idler beam have similar input energies where as for OPA the pump has significant more input energy than the signal or idler, which ever is chosen as the second input beam.

The process of DFG occurs only on materials possessing a non-zero second order susceptibility $\chi^{(2)}$. A basic scheme of the process is shown in Fig. 3.4.
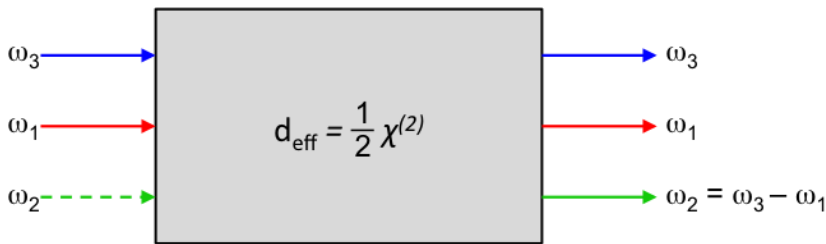
Fig. 3.4 - Schematic of non-linear DFG

The energy transfer in the medium can be described by 3 coupled amplitude equations [66], two of which are

$$\frac{dA_1}{dz} = \frac{2id_{eff}\omega_1^2}{k_1 c^2} A_3 A_2^* e^{i\Delta kz},$$ (3.7)

$$\frac{dA_2}{dz} = \frac{2id_{eff}\omega_2^2}{k_2 c^2} A_3 A_1^* e^{i\Delta kz},$$ (3.8)

where A_1, A_2 and A_3 are the amplitudes of the signal, idler and pump beam respectively, d_{eff} is the effective nonlinear coefficient of the conversion material, also see [136], and ω_1, k_1, ω_2 and k_2 are the angular frequency and wave-vector of signal and idler beam. For simplicity it is only the case of perfect phase-matching considered

$$\Delta k = k_3 - k_1 - k_2 = 0. \tag{3.9}$$

Furthermore, for the third amplitude equation it is assumed that the pump amplitude A_3 is strong and thus undepleted during the conversion process

$$\frac{dA_3}{dz} = 0 \rightarrow A_3(z) \cong A_3. \tag{3.10}$$

Further differentiation of Equ. (3.8) and replacement of $\frac{dA_1^*}{dz}$ on the right-hand side yields

$$\frac{d^2 A_2}{dz^2} = \frac{4\omega_1^2 \omega_2^2 d_{eff}^2}{k_1 k_2 c^4} A_3 A_3^* A_2 \equiv \kappa^2 A_2. \tag{3.11}$$

This equation has the general solution

$$A_2(z) = C\,sinh(\kappa z) + D\,cosh(\kappa z), \tag{3.12}$$

with C and D determined by the boundary conditions of the system. It can be found that $A_2(0) = 0$ and $A_1(0)$ is specified. With these boundary condition the system can be solved such that [66]

$$A_1(z) = A_1(0)cosh(\kappa z), \tag{3.13}$$

$$A_2(z) = i\sqrt{\frac{n_1 \omega_2}{n_2 \omega_1}} \frac{A_3}{|A_3|} A_1^*(0) sinh(\kappa z). \tag{3.14}$$

An illustration of the physical meaning of this result is depicted in Fig. 3.5.

(a)

(b)
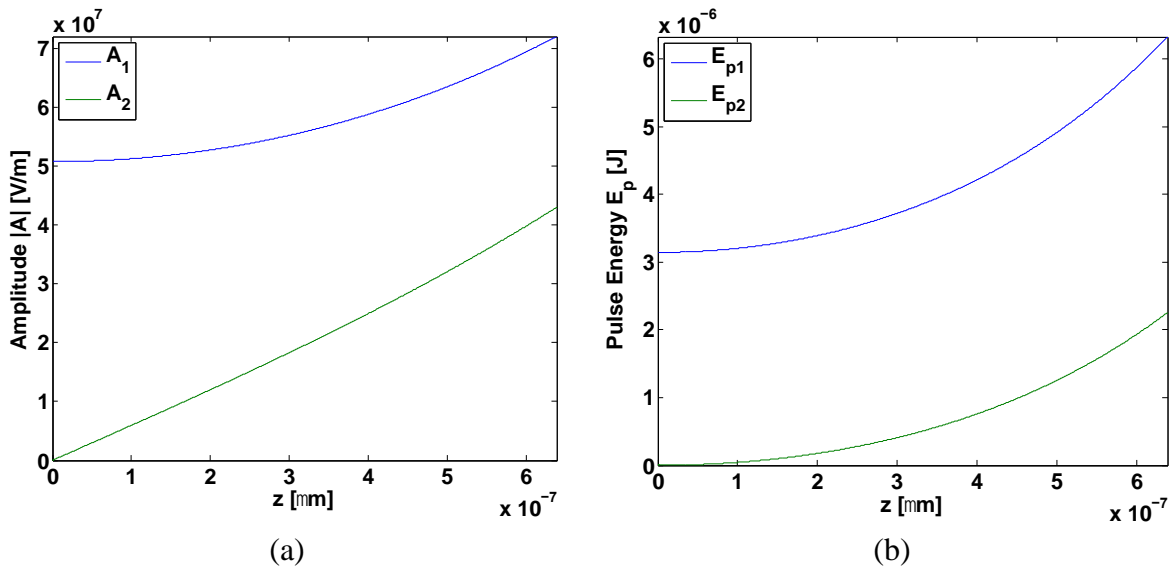
Fig. 3.5 - Illustration of the conversion from DFG using a BBO crystal, $0.3\ mJ$, $100\ fs$ pulses for perfect phase matching

3.1.2.4 Coherent OPerA

The schematic diagram of the Coherent OPerA OPA is depicted in Fig. 3.6.
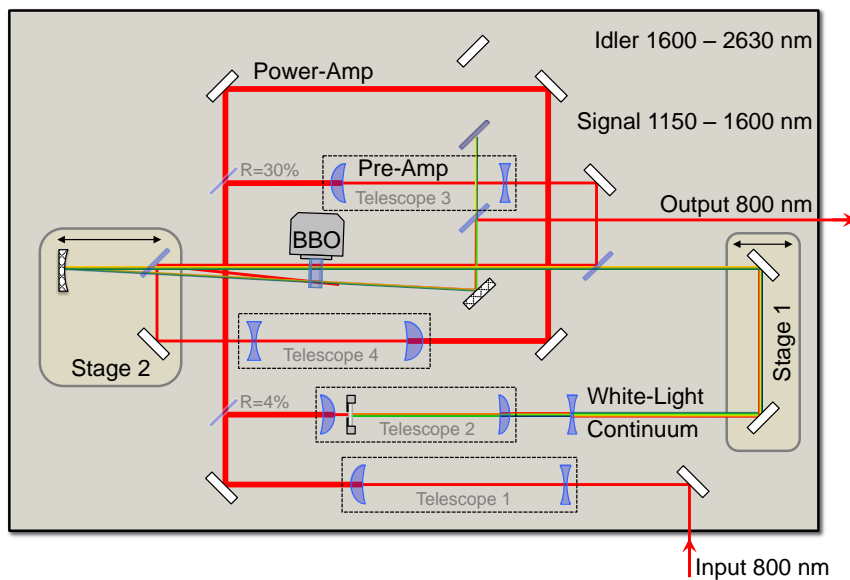
Fig. 3.6 - Scheme of Coherent OPERA OPA

As is shown in the figure, the OPA provides the output of the $810\ nm$ pump, signal and idler pulse simultaneously.

A small part (approximately 1 %) of the input pump pulse from the Spitfire CPA laser system was first focused into a Sapphire plate to generate a white-light continuum. This continuum provided the seed for the desired IR wavelength. It was afterwards focused into a BBO crystal, which was mounted on a rotary positioning stage for angular tuning. The white-light continuum beam was in the BBO crystal spatially and temporally overlapped with the so-called $810\ nm$ pre-amplifier beam (approximately 30 % of original input). By rotating the BBO crystal, phase-matching conditions could be achieved for the desired signal or idler wavelength. If the pulses of pre-amp and white-light continuum were time-synchronized using stage 1 (Fig. 3.6), sufficient energy transfer occurred from the pre-amp beam to the desired IR wavelength. In a second amplification stage, the power amplifier beam, consisting of the rest of the input energy at $810\ nm$, was also time-synchronously (stage 2, Fig. 3.6) superimposed with the generated IR radiation in a second pass through the BBO crystal. The phase matching condition in the BBO crystal was already set due to the pre-amp process. Finally, dichroic mirrors were used to split the desired wavelengths for pump, signal and idler beam to the marked outputs.

The input pulse into the OPA possessed a time duration of approximately $100\ fs$ and was nearly time-bandwidth limited. That means that the spectral content of the pulses supported exactly the time-duration of the pulse. However, changing the center wavelength of the pulse into the IR region while maintaining the desired pulse duration requires an increased spectral content. Therefore, if one assumes that the pulse maintained the property of being nearly time-bandwidth

limited, one can measure the output spectrum of the pulse and back-calculate the temporal width using the following equation for a Gaussian pulse

$$\tau = \frac{1.44 \cdot \lambda^2}{c \cdot \Delta\lambda}.$$

(3.15)

The OPA output spectrum was recorded using an OceanOptics NIR spectrometer. A measured spectrum and beam profile of the $2\,\mu m$ output of the OPA are depicted in Fig. 3.7. Using Equ. (3.15), the pulse duration can be calculated to be $\tau(@2\ \mu m) \le 192$ fs.

(a)   (b)
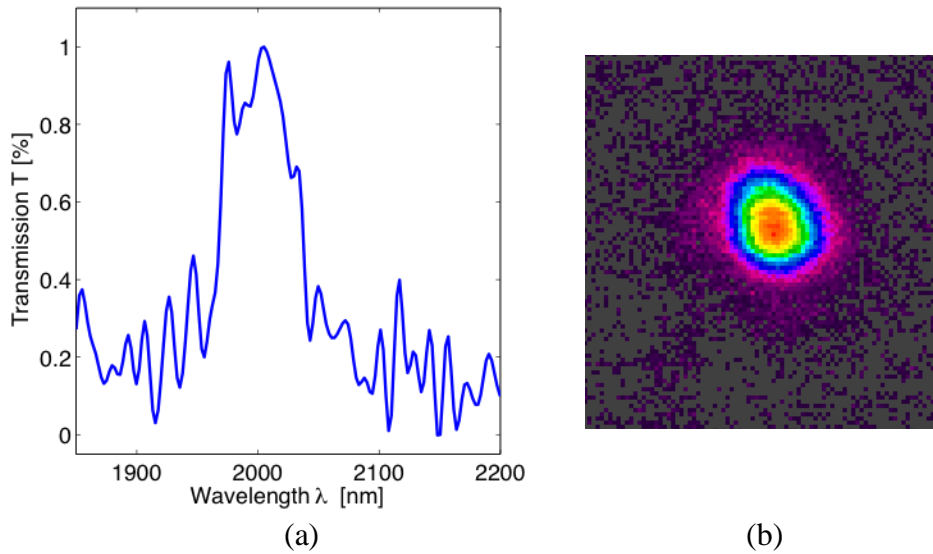
Fig. 3.7 – Illustration of (a) a measured spectrum and (b) a measured beam profile from OPA output at $2.0\,\mu m$ center wavelength

Besides maintaining sufficient bandwidth, the output beam profile is of significant interest. The output beam profile was measured using a Spiricon PyroCAM beam profiler and found to be somewhat elliptical, as already observed from the output beam of the Spitfire system.

3.1.3 High Repetition Rate Laser Sources

The obvious limitation of the used laser sources so far is the low repetition rate. In the following lasers sources used for high repetition rates are detailed.

The laser sources used to generate such high repetition rate ultrafast radiation were (i) an IMRA FCPA μJewel D-400 fiber laser system, FCPA stands for Fiber Chirp Pulse Amplification and denotes that the system is fiber based, (ii) an Amplitude Satsuma fiber laser system and (iii) an Amplitude t-pulse 500 solid state laser system. A summary of the specifications of the high repetition rate laser sources is given in Table 3-1.

Table 3-1 – Overview of laser parameters of high repetition rate radiation sources

Laser Parameter	IMRA FCPA μJewel	Amplitude Satsuma	Amplitude t-pulse 500
f_{rep}	0.1 to 5 MHz	1 to 5 MHz	9.2 MHz
λ_{center}	1043 nm	1030 nm	1030 nm
τ	350 to 450 fs	$\leq$ 400 fs	$\approx$ 500 fs
$P_{avg\ out}$	0.4 W	5W	5 W

3.1.3.1 IMRA FCPA μJewel D-400

The IMRA FCPA μJewel D-400 system [www.imra.com/pdf/fcpa.pdf] was an all-fiber-based laser system. A general schematic layout of such system is shown in Fig. 3.8. The fiber-based oscillator is described in [137]. The free-space compression of the output pulse was achieved in an external compressor. The laser system was a turn-key, providing discrete pulse repetition rates between $100\ kHz$ and $5\ MHz$. The pulse duration was measured to be in the range of 350 to

$450\ fs$, depending on the repetition rate. The center wavelength of the Ytterbium-based laser is $\lambda_{center} = 1043\ nm$, thus, semiconductor materials such as GaAs or SiC with a band gap energy $E_g > 1.18\ eV$ are transparent for the incident laser radiation.
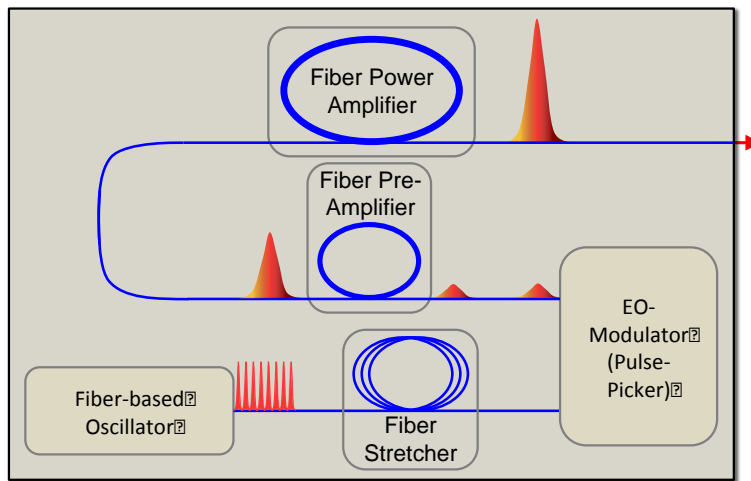
Fig. 3.8 - General scheme of all-fiber-based ultra-short pulsed laser system as used in IMRA FCPA µJewel D-400 laser system[138]

The advantage of this laser system was the capability of changing the repetition rate freely over a large range, giving rise to processing either in the low-repetition-rate or in high-repetition rate regime. Additionally, the fiber-based design ensured for one a very circular output beam profile and therefore a very good beam quality with $M^2 \cong 1$, as depicted in Fig. 3.9. It also made the laser system extremely robust against misalignment, increasing the laser up-time and reducing the necessity of maintenance.

The shortfall of this laser system was its rather limited available pulse energy with approximately $4\ \mu J$ at a repetition rate of $100\ kHz$. It should be pointed out that the laser supplied a constant maximum average power over its repetition rate range of approximately $P_{avg.max} = 400\ mW$. The relation between pulse energy, repetition rate and average power is giving by

$$E_P = \frac{P_{avg}}{f_{rep}} [J].$$

(3.16)
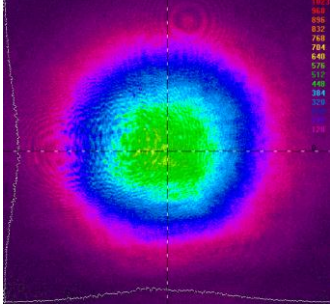
Fig. 3.9 - Measured beam profile of IMRA FCPA µJewel D-400 fiber laser system using a

Gentec Beamage beam profiler

From the equation it is apparent that the pulse energy will decrease inversely with repetition rate, therefore causing the pulse energy to fall below the material modification threshold at high repetition rates.

3.1.3.2 Amplitude Satsuma Fiber Laser

To extend the available pulse energy at high repetition rates, an Amplitude Satsuma fiber laser system [http://www.amplitude-systemes.com/client/document/satsuma_3.pdf] was used. The laser provided a constant output power $P_{avg\,out}$ of $5\,W$ over its full range of available discrete available repetition rates extending from $1\,MHz$ to $5\,MHz$. The pulse duration of the individual pulses τ was given by the vendor at installation of the laser with less than $400\,fs$. The center wavelength λ_{center} of this Ytterbium-doped fiber-laser system was $1030\,nm$. The system was equipped with an electro-optical (EO) modulator that allowed to control single pulse output to a continuous pulse train. The beam profile of the output beam, shown in Fig. 3.10, was comparable to the beam profile of the IMRA µJewel laser system close to $M^2 \approx 1$.
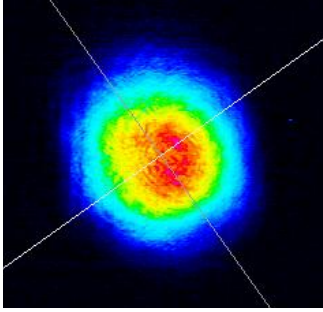
Fig. 3.10 – Measured beam profile of the Amplitude Satsuma laser system Gentec Beamage
beam profiler

3.1.3.3   Amplitude t-pulse 500 Solid-State Laser

The last radiation source used was an Amplitude t-pulse 500 Solid-State laser system
[http://www.amplitude-systemes.com/client/document/t-pulse_5.pdf]. Similarly the Amplitude
Satsuma, the laser provided an average output power $P_{avg\ out}$ of 5 W at a set repetition rate f_{rep}
of 9.2 MHz. The design of the laser system is solely based on the previously shown Kerr-Lens
mode-locked oscillator, however to decrease the repetition rate f_{rep} and increase the pulse energy
E_p the cavity length was greatly extended. The pulse duration τ was provided by the manufacture
with approximately 500 fs. The laser was based on diode-pumped Ytterbium-doped crystal and
therefore had a center wavelength λ_{center} of 1030 nm. The beam profile, shown in Fig. 3.11, was
not as circular as for the fiber laser system, but still close to $M^2 \approx 1$.
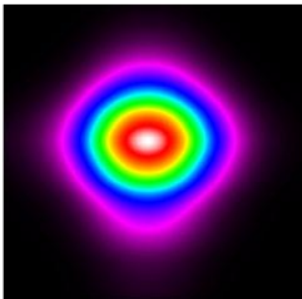
Fig. 3.11 - Provide beam profile of Amplitude t-pulse 500 beam profile by manufacture

3.2   Propagation of Ultrashort-Pulsed Gaussian Beams

Special attention had to be paid to the propagation of ultra-short pulsed laser radiation for material processing applications. Due to the broad bandwidth of the pulse dispersion can affect the temporal profile of the pulse. Therefore, temporal propagation phenomena shall be discussed in further detail in the following section.

3.2.1   Temporal Requirements

Inherent to ultrashort-pulsed radiation is an extended spectral content necessary to generate the short pulse duration. However, due to the frequency-dependence of the refractive index $n(\omega)$, temporal broadening resulting from pulse dispersion has to be taken into account. These effects are most severe for short pulse durations (more spectral pulse width) and often add up noticeable over long propagation distances or in high refractive index materials such as semiconductors.

There are several solutions to cancel temporal broadening resulting from dispersion. In most cases, keeping the propagation distances short reduces dispersion in air to a minimum. To compensate for longer propagation distances, applying negative chirp to the pulse is an easy solution, resulting in the shortest possible pulse on target. Often propagation in vacuum is not or only partly suitable, but will not only result in dispersion-free propagation but also reduces the probability of damaging beam steering optics due to surface ablation.

3.2.2   Chromatic Aberration of Ultrashort-Pulse Laser Radiation

Refraction on material interfaces is common challenge for laser radiation. Usually, chromatic aberration can be neglected since laser radiation is monochromatic. That challenge becomes significant with ultrashort-pulsed laser radiation due to the broad spectral content. An ultimate solution for chromatic aberration does not exist. Keeping the incident angle small reduces the effect on the processing results.

4 FEMTOSECOND PROCESSING OF TRANSPARENT DIELECTRICS

The first demonstrations of local material modification by femtosecond laser radiation inside a bulk transparent dielectric sample were published in 1996 by two groups, Davis *et al.* [7] and Mazur *et al.* [78]. Both researchers reported permanent refractive index modification in the focal region of a tightly focused femtosecond beam. Davis concluded that the translation of the sample relative to the focus beam would introduce 3D structures in the bulk glass such as waveguides. Therefore a new technique of 3D bulk structuring was found and thoroughly investigated in the following decade. This chapter will discuss the general principles, challenges and opportunities as well as advantages and disadvantages of this unique processing technique.

4.1 Principles of 3D Femtosecond Processing

4.1.1 Writing Directions

Based on the non-linear absorption mechanism described in Section 2.2.2, energy is solely absorbed in the focal region of a tightly focused ultrashort-pulsed laser beam inside the bulk of a transparent material. The energy deposition results in permanent modification of the material in focal volume. To create 3D structures, either the sample or the focus has to be moved, which is often referred to as the "femtosecond laser direct writing" (FLDW) technique. In the case of a moving beam, femtosecond-laser-scanners are commonly used as described in ref. [139]. The scanner, in general, contains fast, computer-controlled Galvo-mirrors, which steer the beam over the sample. The implementation of high NA objectives in such system however limits the available process area, which in return can be increased using combinations of 3D positioning stages and the scan-setup. During the experiments conducted in this thesis, such systems were not utilized.

Instead, the beam was kept stationary and the sample was moved with respect to the focus. In such way large areas could be processed in the material utilizing high NA focusing optics.

The first developed two-dimensional structures using the FLDW technique were only linear waveguides, therefore two general writing schemes were defined, depending on the translation direction of the sample. The first, longitudinal writing scheme refers to a translation of the sample in the same direction as the propagation direction of the incident laser beam. The second, transversal writing scheme describes a translation of the sample in an orthogonal direction with respect to the propagation direction of the incident laser beam [140]. Fig. 4.1 (a) and (b) depict the longitudinal and transversal laser direct writing scheme, respectively.

Sample Translation Direction

Sample Translation Direction

(a)   (b)
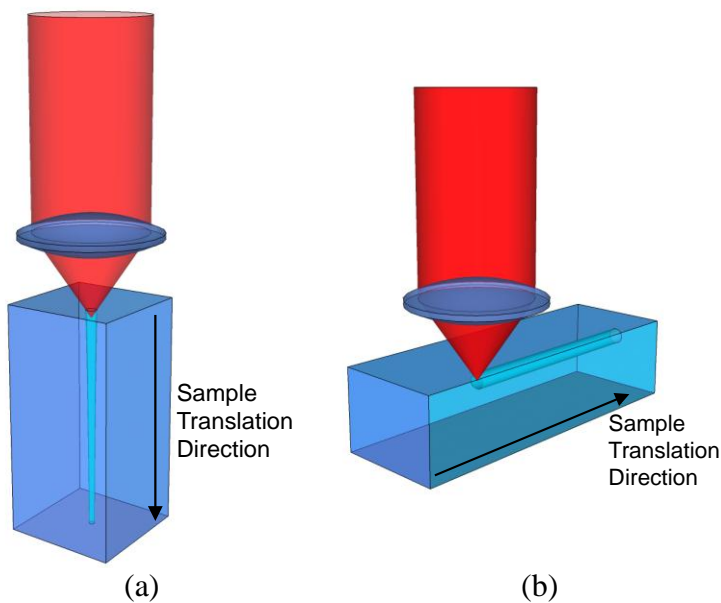
Fig. 4.1 - Schematic of (a) longitudinal and (b) transversal laser direct writing schemes

Each scheme possesses its own advantages and disadvantages. The longitudinal setup results in structures with a very circular modification profile [141], [142], however, the length of the introduced structure is limited by the working distance of the focusing optics used. The transversal

writing scheme overcomes that limitation; the length of the sample itself only determines the length of the structures. However, transversal writing causes the profile of the induced modification to be elliptical, similar to the cross-section of the energy absorption [119], [121], [143], [144]. The asymmetry of the generated structures can be reduced by either increasing focusing power of the used focusing optic or by astigmatic beam shaping of the incident writing beam. The later technique modulates the intensity profile of the beam in the focal region using (i) a slit close to the input aperture of the focusing optic [129], [145] or (ii) a telescope composed of cylindrical lenses before focusing the beam inside the bulk [146]. In both cases the effective focusing power in x- and y-direction is modulated due to the incident beam diameter on the input aperture of the focusing optic, causing an astigmatic beam in the focal region, hence the name. If the sample is translated orthogonally to the direction of the waist resulting from the less focused beam, circularly symmetric structures can be induced.

4.1.2   Focusing Conditions

Besides the influence on the geometrical symmetry of the generated structure, the focusing conditions are of major influence on the achievable results. Three points should be noted here, (i) influence of the refractive index of the sample material, (ii) the influence between the interface of the sample material and the surrounding material, and (iii) the influence of aberrations.

4.1.2.1   Refractive Index of Sample Material

The refractive index n of the material to be processed causes a reshaping of the focusing geometry. It is well established that the beam waist w_0 and therefore the focus diameter D_f remains unchanged but the distance from the interface to the beam waist s_{focal} shifts according to

the optical path length in the sample material. Furthermore, the Rayleigh length z_R increases with increasing refractive index of the sample according to

$$z_R = \frac{\pi n w_0^2}{\lambda_0}.$$

(4.1)

Thus, the ratio of beam waist and Rayleigh range increases linearly with the refractive index of the sample material and hence an increased ellipticity of the focal volume occurs. Therefore, the introduced structure becomes increasingly asymmetric between the direction of the beam waist and the direction of the Rayleigh length.

4.1.2.2 Influence of the Interface

Fresnel reflections on the interface between the sample and the surrounding medium are a common challenge when passing beams through transparent materials. Usually the total reflected power is not too significant, i.e. only 4% of the total incident power on a single interface of common glass and air. The reflected power can be calculated as

$$P_{\text{refl}} = P_{\text{inc}} \cdot R_{\perp/\parallel},$$

(4.2)

with the Fresnel reflection coefficient in orthogonal ($\perp$) and parallel ($\parallel$) direction as

$\perp$ $\qquad R_{Fresnel} = \left(\frac{n_1 \cos(\alpha_1) - n_2 \cos(\alpha_2)}{n_1 \cos(\alpha_1) + n_2 \cos(\alpha_2)} \right)^2,$

(4.3)

$\parallel$ $\qquad R_{Fresnel} = \left(\frac{n_1 \cos(\alpha_2) - n_2 \cos(\alpha_1)}{n_1 \cos(\alpha_2) + n_2 \cos(\alpha_1)} \right)^2.$

(4.4)

However, if the refractive index difference at the interface becomes large, the reflected part of the incident power becomes substantial. Moreover, since the TM polarized part of the focused beam experiences the Brewster angle phenomena, the function describing the reflected part has a dip at certain angles, distorting the focused energy distribution.

4.1.2.3 Focusing Aberrations

The design, and moreover manufacturing process of optical elements generally starts from a perspective of geometrical optics in which focusing and defocusing elements are for simplicity approximated by spherical shapes. Since this approximation lacks in real-life applications, aberrations occur and distort the intensity distribution of ideally focused beams.

The most concerning aberration of 3D laser fabrication is spherical aberration, however, in cases of mid-IR radiation, chromatic aberrations become significant as well. An example of an ideally focused and a distorted beam due to spherical aberrations in shown in Fig. 4.2 (a) and (b), respectively. The effect scales with the focusing power of the used optic, and hence is significant for high-NA microscope objectives as generally employed for 3D FLDW. The poor quality of the focal spot will therefore lead to a loss of accuracy in the fabrication process.

(a)   (b)   (c)
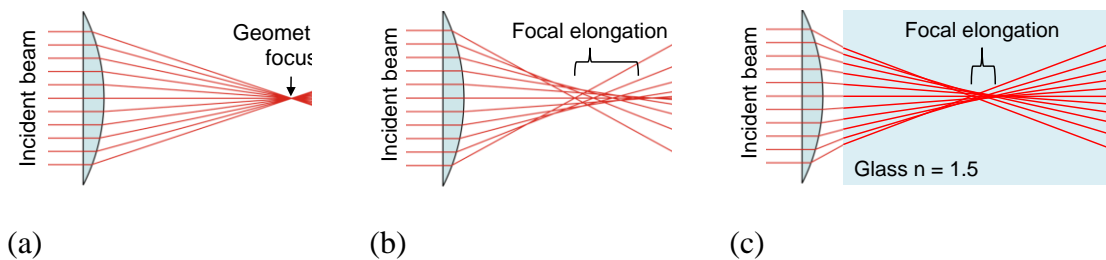
Fig. 4.2 - Influence of spherical aberration on the focusing capabilities of a beam; (a) geometrical approach, (b) focal elongation when focused in air and (c) in transparent dielectric

In commonly available objectives it is custom that spherical aberration is accounted for in the optical design, thus correcting it to reassemble the geometrical ideal case. When then used in the assumed operation condition, it typically results in a focusing region that is virtually

indistinguishable from a geometrically focused case. For commonly used microscope objectives such specified operation conditions are

- optics immersed in standard media (often air)

- use of standard cover slips

- transmission of a specified wavelength

In 3D FLDW these conditions are rarely given. The specified wavelength is normally easily corrected for by choosing an aberration-corrected objective specified for the used laser wavelength. Since FLDW is used to modify deep inside bulk material, the immersion in a standard media or the use of a cover slip is often not applicable. The focus is usually located inside a material with a higher refractive index than air. In such case, spherical aberrations will distort the focal region as depicted in Fig. 4.2 (c).

4.1.3   Influence of Processing Parameters

Obviously, there is a continuous space of processing parameters when structuring inside bulk material such as the sample material itself, the pulse energy E_p, the sample translation speed v_{sample}, the pulse repetition rate f_{rep}, the focusing power given by the effective NA of the optic used, the spatial overlap of adjacent spots S_{spot} or tracks S_{track} and the wavelength λ_0 of the incident radiation. Some of these parameters are dependent on each other. The overlap of spots is given by the ratio of repetition rate, translation speed and focus diameter as

$$S_{spot} = 1 - \frac{v_{sample}}{f_{rep}D_{focus}},$$

(4.5)

where as the overlap between tracks is given by the ratio of line offset Δs_{track} and focus diameter D_{focus} as

$$S_{track} = 1 - \frac{\Delta s_{track}}{D_{focus}}. \qquad\qquad (4.6)$$

Often changing one of these parameters influences the processing result significantly. Often the accumulated intensity of an area, also called the energy (or intensity) dose, is used for a better comparison of experimental results, given as

$$I_{accum} = \frac{E_p f_{rep}}{\pi w_0^2} \frac{1}{1-S_{spot}} = \frac{E_p f_{rep}^2 D_{focus}}{\pi w_0^2 v_{sample}} \left[10^{-4} \frac{W}{cm^2}\right]. \qquad\qquad (4.7)$$

However, most often a broad parameter study is necessary to investigate the influence of changing process parameter.

4.2   3D Laser Direct Writing Setup

The generally used processing setup is depicted in Fig. 4.3 consisting of an illumination source, an imaging system, the focusing optic and a 3D translation system for the sample movement.

The motion systems used for FLDW were computer controlled 3D stages ((i) VP-25XA, Newport; (ii) ALS-25, Aerotech) with a lateral resolution of < 0.1 µm. The software control of the motion enabled the translation of the sample along complex 3D paths to fabricate the desired structures. The employed focusing optics varied widely with a NA ranging from 0.1 to 0.65. In addition to common refractive objectives, also reflective Schwarzschild objectives were used to focus the radiation. Industrial CCD cameras were used to implement the imaging systems. A collinear path for the imaging and irradiation system was chosen to enable online imaging during the sample irradiation.
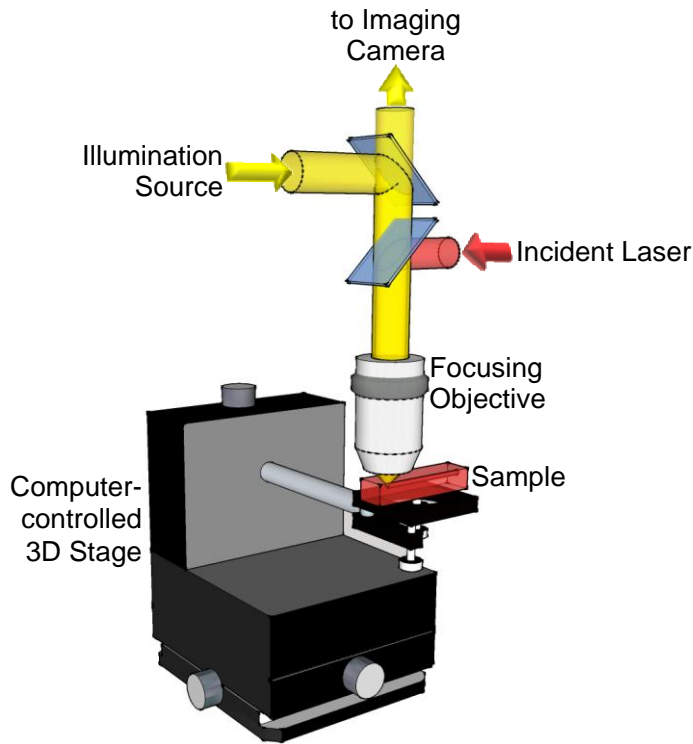
Fig. 4.3 - Scheme of the used 3D processing setup

A light valve composed of a half-wave plate and a polarizing beam splitter was used to control the incident pulse energy on the sample. Since the radiation from the laser output was linearly polarized, changing the relative rotary position of the half-wave plate allowed adjustment of the throughput of radiation through the beam splitter in a desired direction.

4.3   Generation of Photonic Devices in Telluride-Glass

The fabrication of photonic devices is a major application for 3D FLDW [147]. When using this technique, the only requirement on the host material so far was that it had to be transparent for the wavelength of the writing laser. Therefore, it is rather desirable to tailor the host material properties, beside transparency in NIR, to a specific application. For example, a host material that is easily doped is of advantage when fabricating a waveguide laser.

Telluride glass possesses some properties such as transparency in the mid-IR or dopant susceptibility, which makes it especially desirable for photonic device fabrication. However, until now, it was not possible to conserve its most promising properties such as mid-IR transparency and still enable 3D FLDW inside bulk Telluride glass.

This section will summarize the unique properties of this material as host and candidate for photonic devices and examine the suitability of the FLDW technique to create such devices.

4.3.1 Properties of Telluride-Glass

The range of available laser sources extends continuously, especially towards the longer wavelength region into the mid-IR. Many applications in medicine, bio-photonics or material processing can advance if laser sources in that region would be widely available. Besides the right dopant for sufficient pump conversion, a host material transparent in the mid-IR is needed. Telluride is one of the outstanding candidates to fulfill many of the desired requirements.

First and most important, Te-glass is transparent from approximately $5\ \mu m$ to the visible spectrum around $400\ nm$ [148]-[150]. That makes the glass family very interesting for photonic device applications in the mid-IR.

Also, Te-glass can accept a high concentration of dopant atoms [151], which makes it a prime candidate for photonic device fabrication purposes. Another often-useful property of Te-glass is the large non-linear refractive index. In Te-glass n_2 is usually one order of magnitude larger than in Fused Silica [151], [152], which greatly enhances processes like the Kerr Effect or Self-Phase-Modulation. The latter can provide a means to generate a broader emission spectrum for "white-light" generation in the mid-IR.

The ordinary refractive index of Telluride glasses is approximately **2**, which is higher than for standard glasses with a refractive index value of 1.5. However, light propagation in Telluride composition does not experience anomalous dispersion in the mid-IR region, which may give rise to compensate for pulse broadening in mid-IR fiber laser setups [153], [154].

A very commonly used technique of signal amplification in telecommunication applications is by Raman shift amplification. The Raman shift in Te-glass supersedes the achievable shifts in standard silica-based amplifiers fivefold with a much larger gain coefficient [155], [156]. Therefore, Te-based Raman amplifiers may pose a viable alternative to conventionally employed amplification systems.

Overall, the properties of Te-glass could provide a solution for many challenges in photonic and optical device fabrication and development.

4.3.2   Femtosecond Processing

As indicated, the properties provided by Te-glass compositions are very favorable for applications in photonic devices. On the contrary, 3D FLDW is a unique tool to fabricate photonic devices very fast and cheap, ideal for prototyping and development purposes. Hence, the combination of these fields yields the potential for great success. However, a thorough investigation on the influence of varying process parameters is required before such a success story can take place.

In the following, two points of interest were matter of detailed research:

- The modification threshold of Te-glass compositions and the favorable processing regime

- The maximal achievable refractive index change in the bulk glass

4.3.2.1 Modification Threshold and Processing Regime

To determine the processing regime, bulk Te-glass was irradiated at different repetition rates and pulse energies. It was determined that the bulk material modification threshold is approximately $100 \, ^{GW}/_{cm^2}$, shown in Fig. 4.4(a), which is a surprisingly low value compared to other dielectrics like Fused Silica or borosilicate glass with $35 \, ^{TW}/_{cm^2}$ and $25 \, ^{TW}/_{cm^2}$, respectively [157]. The reason for this large difference in threshold is the increased number of pulses, here 4×10^4, incident for the Te-experiment, whereas the data for Fused Silica and borosilicate glass referred to single pulse irradiation. It has been shown that for an increased number of incident pulse an accumulative modification threshold exists which is significant lower than the single pulse modification threshold [158]-[161].

Therefore the measured threshold should be referred to as the accumulative modification threshold. Fig. 4.4(b) shows the threshold for HA. Below a repetition rate of $f_{rep} = 1500 \, kHz$ the size of the modification increases with increased number of incident pulses, above this repetition rate the size remains constant. In addition, an extended outer ring around the center spot appears in the presence of HA, characteristic for the high repetition rate regime. This extended modification size is caused by the increased temperature in the focal volume and hence local melting during the processing in the high repetition rate regime, as demonstrated before by Schaffer [162], Gattass [77] and Eaton [127].
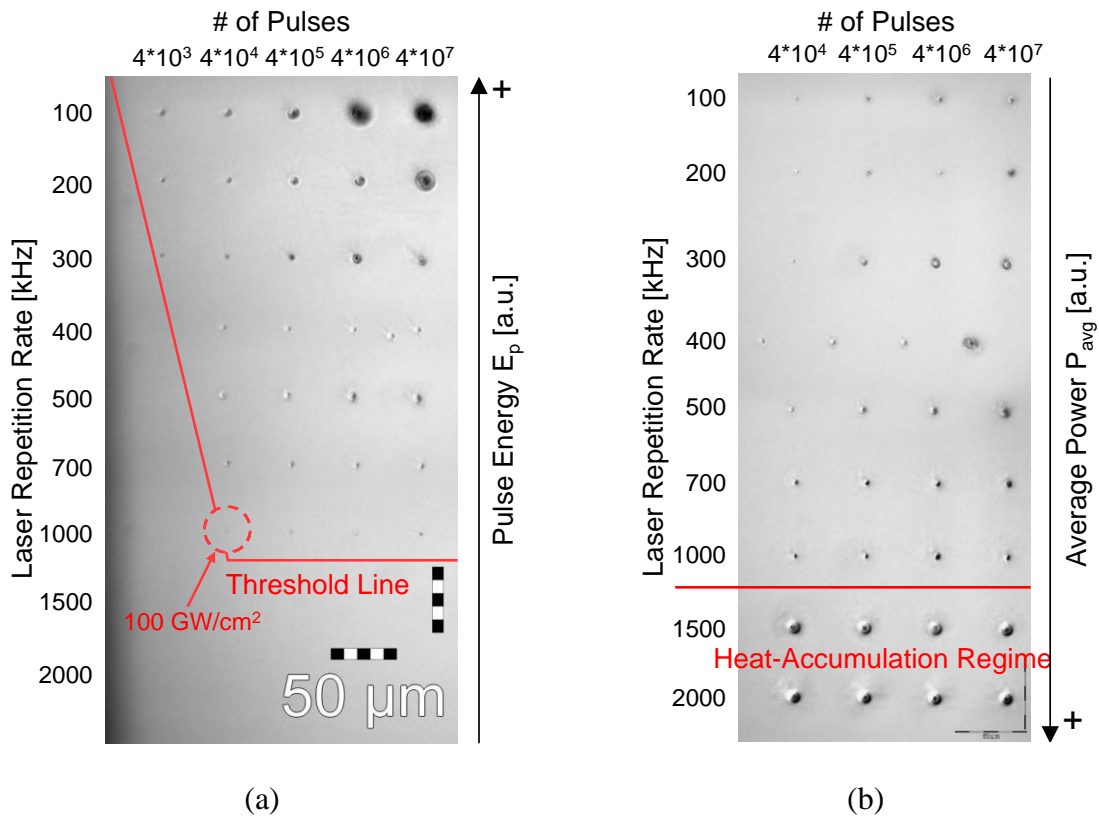
Fig. 4.4 – Confocal microscope images of threshold maps of investigated Te-glass composition, (a) at a constant avg. power of $100\ mW$ and (b) at a constant pulse energy of $200\ nJ$ over the range of the laser repetition rate, at a focusing depth of $150\ \mu m$ using a NA of 0.4 with approximately $350\ fs$ pulse duration

4.3.2.2   Refractive Index Modification

To investigate the change in refractive index, waveguides were written inside the bulk material using a transversal writing scheme, Fig. 4.1(b). Generation of waveguides was performed varying the following parameters

- pulse energy E_p

- translation speed v_{write}

- repetition rate f_{rep}

- numerical aperture (NA)

- focusing depth in the material from the sample surface t_{focus}

A simple far-field NA-measurement setup was employed, as described in [163], to investigate the achieved index change. An example of a recorded far-field image is shown in the inset of Fig. 4.5 and Fig. 4.6. It was found that a positive homogenous refractive index change, as typical for Type I modification (see Section 2.2.6), was induced for focusing NAs of 0.25, 0.4 and 0.65 in the low repetition rate regime at $f_{rep} = 100$ kHz, as depicted in Fig. 4.5. However, the largest change was achieved using an NA of 0.4. It is also curious to notice, that the fluence necessary to induce a homogenous change was approximately equal for an NA of 0.25 and 0.4, but approximately fourfold higher for an NA of 0.65.
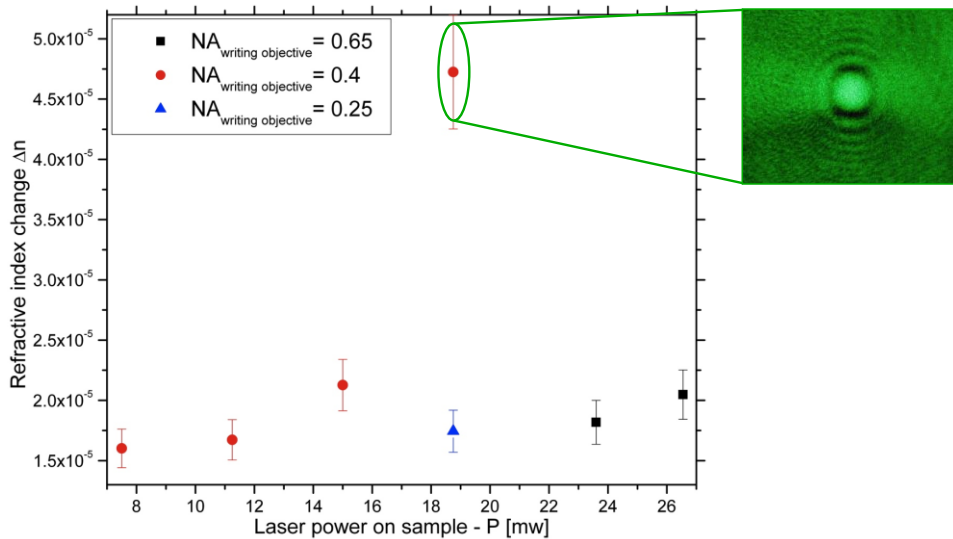
Fig. 4.5 – Graph of the homogeneous positive refractive index modification for the used focusing objectives derived from the farfield intensity distribution for a constant laser repetition rate of $100\ kHz$; inset: image of farfield intensity distribution used for waveguide NA measurement

Successful waveguiding was also obtained when irradiating the sample at a repetition rate of $f_{rep} = 1$ MHz close to the high repetition rate regime, as depicted in Fig. 4.6. The magnitude of the refractive index change here was approximately equal to the change when irradiating with 100 kHz repetition rate. However, from the shown graphs it is apparent that an increased energy leads to a higher index change, up to the point at which inhomogeneous modification takes place. A waveguiding shell surrounding a non-waveguiding core characterized this type II modification (images not shown).
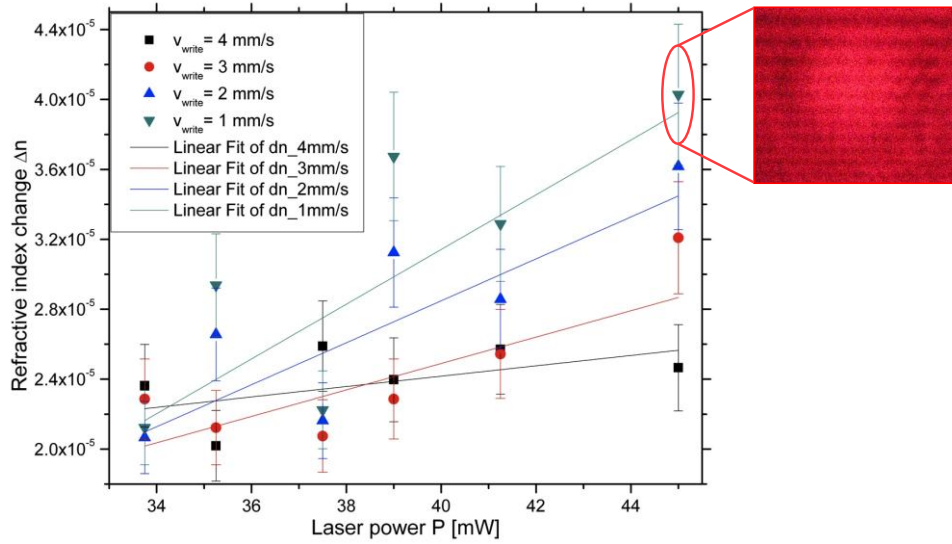
Fig. 4.6 – Graph of the dependence of the achievable refractive index modification as a function of sample translation speed for a constant laser repetition rate of $1\ MHz$; inset: image of farfield intensity distribution used for waveguide NA measurement

The largest refractive index change achieved that provided a wave-guiding structure was approximately $\Delta n_{\max guiding} \approx 5 \cdot 10^{-5}$. This value is two to three orders of magnitude lower than demonstrated for ultrashort-pulsed laser radiation induced refractive index changes in Fused

Silica [111], [164] or borosilicate glass [128], respectively. Nevertheless, the presented results showed for the first time wave-guiding structures in a non-phosphate Te-glass composition.

It should be pointed out here that an increase in induced refractive index change was observed when increasing the focusing depth for the irradiation process, shown in Fig. 4.7(a). This result is unexpected since the influence of spherical aberrations would distort the focusing volume and therefore reduce the energy per volume. Furthermore, due to the larger non-linear refractive index of Te-glasses self-focusing could be expected with increased focusing depth. The measurement of the depth of the induced modification revealed that self-focusing was not occurring during the irradiation process, as depicted in Fig. 4.7(b).

(a)   (b)
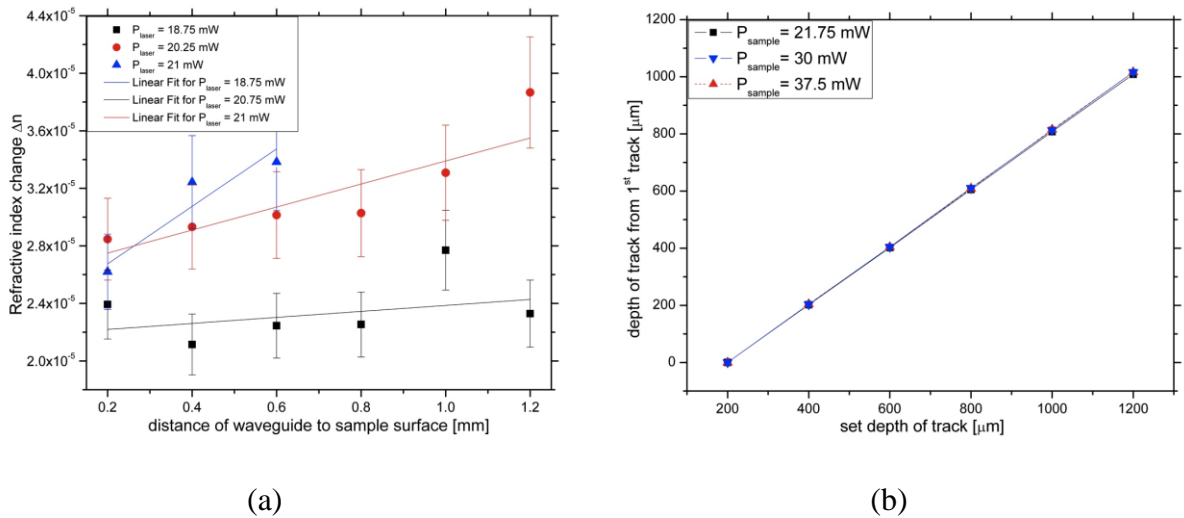
Fig. 4.7 – Graph of the dependence of the (a) achievable refractive index modification on the focusing depth with respect to the sample top surface and (b) actually measured focusing depth after irradiation at a constant laser repetition rate of $100 \; kHz$

The refractive index profile of the generated waveguides was measured using quantitative phase imaging [165]-[167]. It is apparent from Fig. 4.8 that an area of reduced refractive index surrounds the positive center of the modification. These findings are consistent with findings by

Fernandez *et al.* [168] and Nandi *et al.* [114], the latter suggested that a migration of La-stabilizer-atoms from the center region into the surrounding volume cause the modulation in refractive index change in this glass composition.
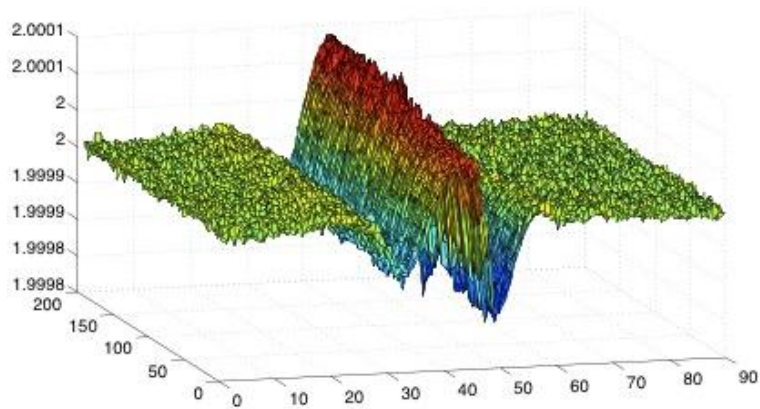
Fig. 4.8 – Graph of the refractive index profile of modification in Te-glass due to ultrashort-pulsed laser irradiation

5 NANO-FIBER GENERATION ON TRANSPARENT DIELECTRIC SURFACES

5.1 Introduction

As described in Section 2.2.7, there is a significant increase in local temperature in the focal volume when processing materials at pulse high repetition rates. This increased heat can quickly lead to local melting of the material [169], [170]. If the focal volume is in close proximity to the sample surface, the molten material can break through the surface and form fiber-like structures on the surface. The diameter of the generated fibers is in the nanometer scale, and the aspect ratio, which is the ratio of the width of the nano-fiber compared to its length, can be greater than 1:1000. Furthermore, the width of the fiber is approximately constant over its full length. Such formation of nano-fiber structures from the surface has not previously been observed using bulk femtosecond laser irradiation. The underlying mechanism that causes the formation of the nano-fibers by femtosecond irradiation is still under investigation.

However, similar nano-fiber formations have been reported using cw-radiation in combination with super-sonic gas jets [171]-[174] on soda-lime glasses and polymer materials. In these experiments a CO_2 laser at an emission wavelength of 10.4 μm was used to heat the sample material to a liquid state, then the gas jet was applied to draw the fibers from the liquefied volume. Even though the processing conditions are not precisely the same, Quintero *et al.* developed a mathematical model to describe the formation process.

The following chapter will detail the experiments and results of such nano-fiber formation due to high repetition rate ultrashort-laser pulse trains. Similarities between the here obtained experimental results and the result utilizing a super-sonic gas jet will be discussed.

5.2   Experimental Conditions

A wide range of processing parameters, such as pulse repetition rate, number of pulses, focusing depth, and incident average power, needed be covered to investigate the dependence of the nano-fiber formation on the irradiation condition.

5.2.1   Sample Irradiation Setup

For the subsequent experiments, the samples were irradiated using the previously described processing station (Chapter 4.2) providing the focusing objective, online imaging capabilities and computer-controlled motion system for sample positioning.

5.2.1.1   Pulse Repetition Rate Modulation

Three high repetition rate laser sources were used to conduct the nano-fiber formation experiments. At CREOL, an IMRA μJewel FCPA laser system and an Amplitude Satsuma fiber laser system were used. Both laser sources provided step-wise variable pulse repetition rates, ranging from 0.1 to 5 MHz and 0.5 to 5 MHz respectively. An Amplitude t-pulse 500 solid-state laser system was used to perform the experiments at the Bordeaux University. This laser source had a set repetition rate of 9.2 MHz. The laser sources are described in more detail in Chapter 3.1.3.

5.2.1.2   Number of Incident Pulses

Depending on the laser source, control over the number of pulses was realized by either an external mechanical shutter or a laser-integrated pulse-picker. This provides the ability to vary the incident number of pulses on the sample between 10^0 and 10^7, depending on the particular experiment.

5.2.1.2.1 External Mechanical Shutter

Pulse train durations of greater than $4\,ms$ could be achieved using an external mechanical shutter. The shutter was electronically controlled from within the software program that also controlled the motion of the 3D-stage. Therefore a synchronized motion to the incident pulse train could be accomplished.

5.2.1.2.2 Laser-Integrated Pulse-Picker

For pulse trains shorter than $4\,ms$ a pulse picker was necessary. It allowed single pulse control, and was also integrated in the setup such that it could be triggered from within the program that controlled the sample motion. Therefore synchronized motion and irradiation could be accomplished. The opening duration was externally controlled using a time-delay generator (Stanford Research Systems DG535) with a programmable time delay resolution of less than 10 ps.

5.2.1.3 Focusing Optics

Mitutoyo NIR long working distance objectives were used during the experiment to focus the laser radiation on and inside the bulk samples. Such objectives provided working distances larger than 10 mm at a high numerical aperture of greater than 0.5, and therefore did not prohibit or interfere with the formation of several hundreds of micrometers long nano-fibers on the sample surface. Unfortunately, due to the involved number of optical surfaces in these objectives the transmission was only approximately 50%.

The physical focus position was varied in $10\,\mu m$ steps ranging from 0 to $100\,\mu m$ inside the bulk sample with respect to the sample surface.

5.2.1.4 Incident Average Power

The incident average power P_{avg} was controlled using a light-valve as described in Section 4.2, or by modulation of the diffraction efficiency of the EO-module of the pulse picker. That allowed the incident average power to be varied between 0 and maximal 2.5 W. A graph that depicts the incident power on the sample as function of EO-voltage is shown in Fig. 5.1.
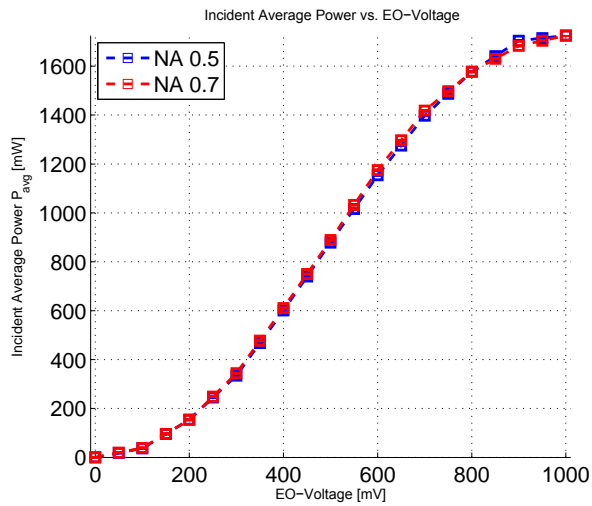
Fig. 5.1 - Graph of the incident average power as a function of the EO-module voltage of the pulse-picker

Table 5-1 below lists a summary of the covered processing parameter space during the experiment.

Table 5-1 - Range of processing parameters for nano-fiber formation experiment

Processing Parameter	Range
Repetition Rate f_{rep}	$0.1 - 9.2\ MHz$ (step-wise)
Number of Pulses $\#_{pulses}$	$1 - \infty$
Focusing Depth t_{focus}	$0 - 0.1\ mm$
Average Power P_{avg}	up to $5\ W$ laser output

5.2.1.5 External Field Setup

To investigate whether the ejected nano-fibers possess a charge during their formation or not, an irradiation experiment on EAGLE2000® was performed within an externally applied DC E-Field. A custom sample holder was designed that allowed to application of a DC voltage in the range from 0 to 1 kV using a Bertan Associates, Inc. Model 2025-03R high voltage supply, shown in Fig. 5.2. The EAGLE2000® sample was sandwiched between the two metal plates (brown parts in Fig. 5.2), while the voltage supply was connected to the metal screws.
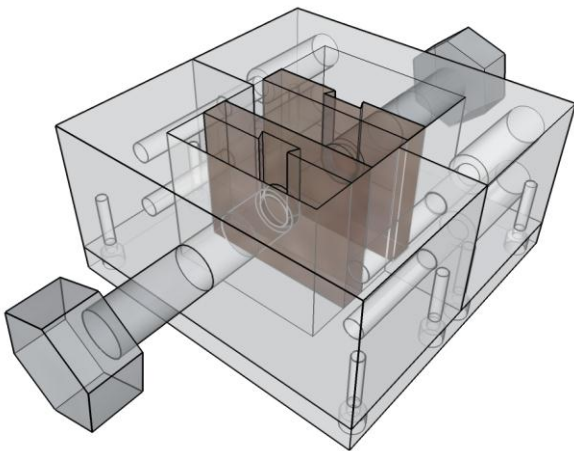
Fig. 5.2 - Custom designed sample holder to apply a DC E-Field during irradiation process

5.2.2 Material-Dependence of Nano-Fiber Formation

Moreover, to investigate the dependence of the nano-fiber formation on the material, these experiments were performed in five different materials with varying lattice structure and melting temperature. Of special interest was the influence of an amorphous or crystalline lattice, due to its implications on the heat conductivity of the material. A list of the investigated materials and their properties is given in Table 5-2.

Table 5-2 - Material properties of sample materials used in nano-fiber formation experiments

Material	Lattice Structure	Heat Conductivity $[^W/_{m \cdot K}]$	Specific Heat $[^J/_{kg \cdot K}]$	Melting Temperature $[K]$
Fused Silica SiO_2	amorphous	1.38	$0.703 \cdot 10^3$	2100
Fused Quartz SiO_2	crystalline	10.4	$0.733 \cdot 10^3$	2200
EAGLE2000®	amorphous	$0.8 - 1.4$	$(0.7 - 1.2) \cdot 10^3$	1100
FOTURAN®	amorphous	1.35	$0.88 \cdot 10^3$	1000
Sapphire Al_2O_3	crystalline	42	$0.756 \cdot 10^3$	2400

5.2.2.1 Material Properties of Used Dielectrics

Fused Silica and Fused Quartz are the simplest dielectrics with respect to their composition, being SiO_2. The two materials vary only in the lattice structure, amorphous and crystalline, respectively. The transmission edge of these materials was shorter than 180 nm as shown in Fig. 5.3. That wavelength corresponds to a bandgap energy of $E_g > 7\ eV$, using Equ. (2.1). Often a bandgap energy of $E_g \approx 9\ eV$ is reported in the literature [113], [175].

The commercial commonly used dielectric EAGLE2000® is a aluminumsilicate glass, containing beside it's base material SiO_2 (55%) addition compounds such as B_2O_2 (7%), Al_2O_3 (10.4%), CaO (21%), and NaO (1%). The energy bandgap of this glass is lower than that of Fused Silica, Quartz (compare Fig. 5.3), making it easier to process with the available laser photon energies. In addition, the melting temperature is lower compared to the other three materials, allowing heat accumulation effects to occur at much lower pulse energies. The transmission edge of this dielectric is at $275 \; nm$ (Fig. 5.3) and thus the bandgap energy is $E_g = 4.5 \; eV$.

FOTURAN® also consist of many additive glass modifiers [176], however, differs from the rest due to its silver dopant content. The energy bandgap of this glass composition is also $E_g = 4.5 \; eV$ as apparent from the transmission edge at $275 \; nm$.

As is Fused Quartz, Sapphire is also a crystalline dielectric. The band edge and bandgap energy are $140 \; nm$ [177] and $E_g = 8.8 \; eV$, respectively.
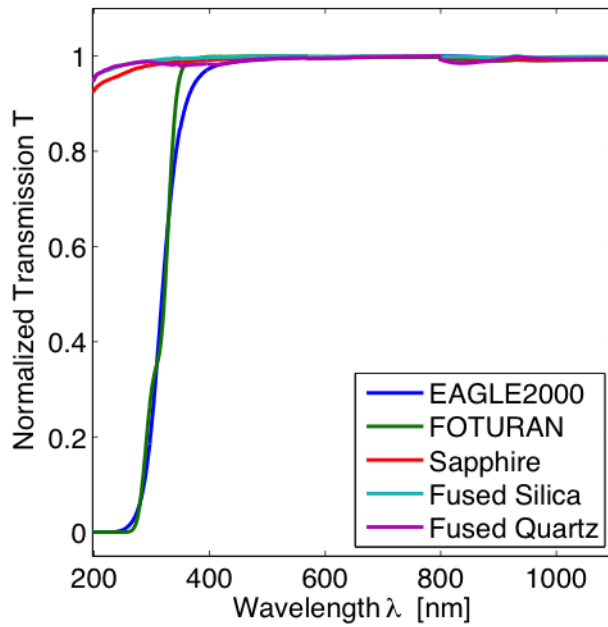
Fig. 5.3 - Measured transmission spectra of the used dielectrics

5.3   Observation

During the irradiation process a bright white light emission was apparent from the focal volume for some of the materials irradiated. Fig. 5.4 (a) shows images taken during the sample irradiation process for a pulse repetition rate of $f_{rep} = 9.2\ MHz$. Lowering the incident average power below a certain threshold value caused the bright emission to disappear, shown in Fig. 5.4(b). The particular threshold energy at which the white light emission occurred was material dependent and is listed in the Table 5-3 below.

Table 5-3 - Table of threshold pulse energy for white light emission to occur during irradiation process

Material	$E_{p\ threshold}\ [nJ]$
Fused Silica	82
EAGLE2000®	27
FOTURAN	27
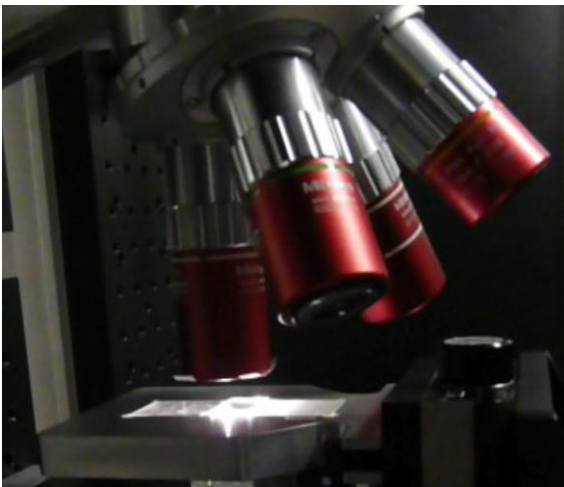
(a)
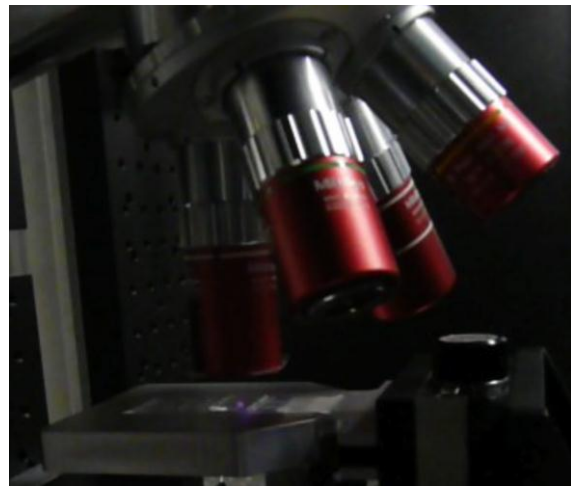
(b)

Fig. 5.4 – Images of light emission during the sample irradiation process with (a) strong white light emission and (b) weak emission at a pulse repetition rate of 9.2 MHz

To characterize the emission during the irradiation process spectra were recorded for various repetition rates, materials and incident average powers. Fig. 5.5 depicts such spectra exemplary for Fused Silica. The emission spectra from EAGLE2000® and FOTURAN® look, in general, similar to the spectra of Fused Silica.

Fig. 5.5(a) shows that the emitted intensity increases with increasing incident average power. The peak emission wavelength does not shift with average power. Fig. 5.5(b) shows the normalized

emission at five different repetition rates. It is noteworthy and unexpected that the peak wavelength also did not shift.

(a) (b)
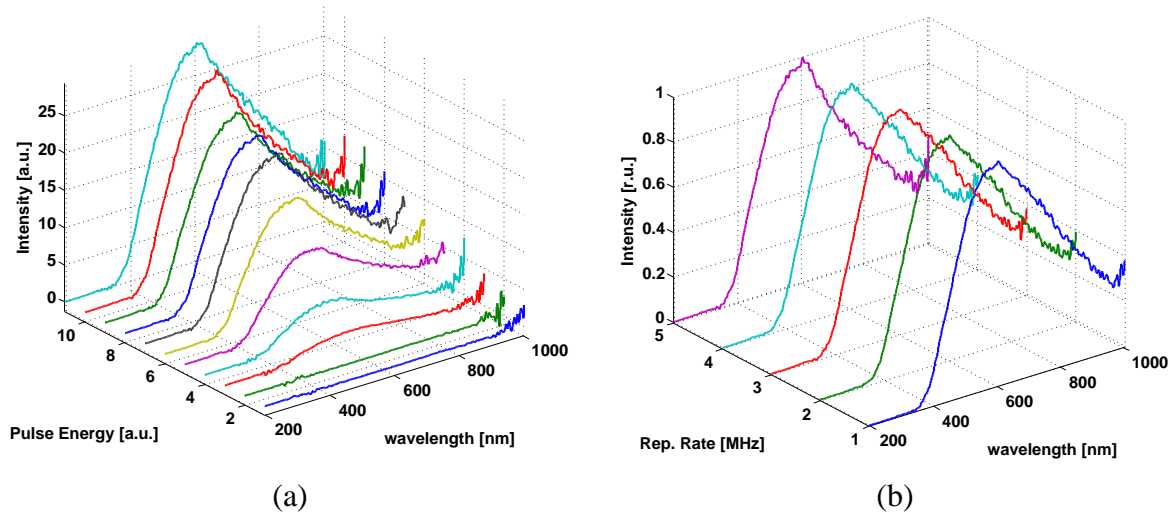
Fig. 5.5 – Recorded emission spectra during the irradiation process of Fused Silica at (a) different incident average power at $f_{rep} = 6.1\ MHz$, and (b) different repetition rates at maximal average power

After irradiation all processed areas on the samples were imaged using an Olympus BX-52 confocal microscope as well as a SEM. In addition, TEM was performed on some of the generated nano-fibers. The follow sub-section will detail the observations made for the various exposed materials.

5.3.1 Confocal Microscopy

An overview Differential Interference Contrast (DIC) image of the irradiation map was recorded for each processed focusing depth, shown for $100\ \mu m$ in Fig. 5.6. The laser radiation was incident from the top. Clearly visible is the change in modified area around the center spot in north-south direction due to the modulation of number of pulses. Less obvious is the areal change in east-west direction in Fig. 5.6 due to the modulation of incident average power. The overview

images were used to measure the z-expansion length of the modified region in the propagation direction of the incident beam. The value of the z-expansion length was assumed to be equal to the maximum focusing depth at which the modification broke through the surface. In a second measurement step, the dimensions of each irradiation site were recorded using maximum microscope magnification. An example is shown in the inset on the right of Fig. 5.6.
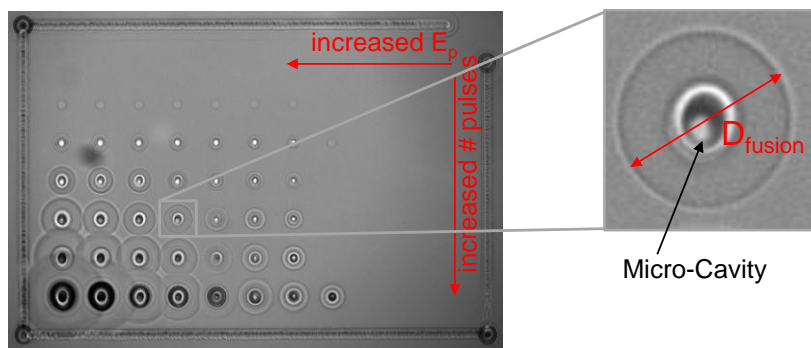
Fig. 5.6 – Confocal microscope image of irradiation map, right: single irradiation site

It was found, that most irradiation sites in Fused Silica, EAGLE2000®, and FOTURAN® developed an inner and outer structure when exposed to several pulses at high repetition rate. The inner structure at the center of the modified area is here defined as the core modification, most likely consisting of a micro-cavity. The outer ring structure around the core modification is defined as the fusion front diameter. It should be pointed out that crystalline Fused Silica, a.k.a. Fused Quartz, and Sapphire did not develop the outer structure but did form the inner micro-cavity.

In the following, the fusion front diameter and z-expansion length for Fused Silica, FOTURAN®, and EAGLE2000® will be discussed in detail.

5.3.1.1   Fused Silica

Fig. 5.7 and Fig. 5.9 illustrate the evolution of (a) the fusion front diameter and (b) the z-expansion length for Fused Silica at NA's of 0.5 and 0.7 respectively.

94
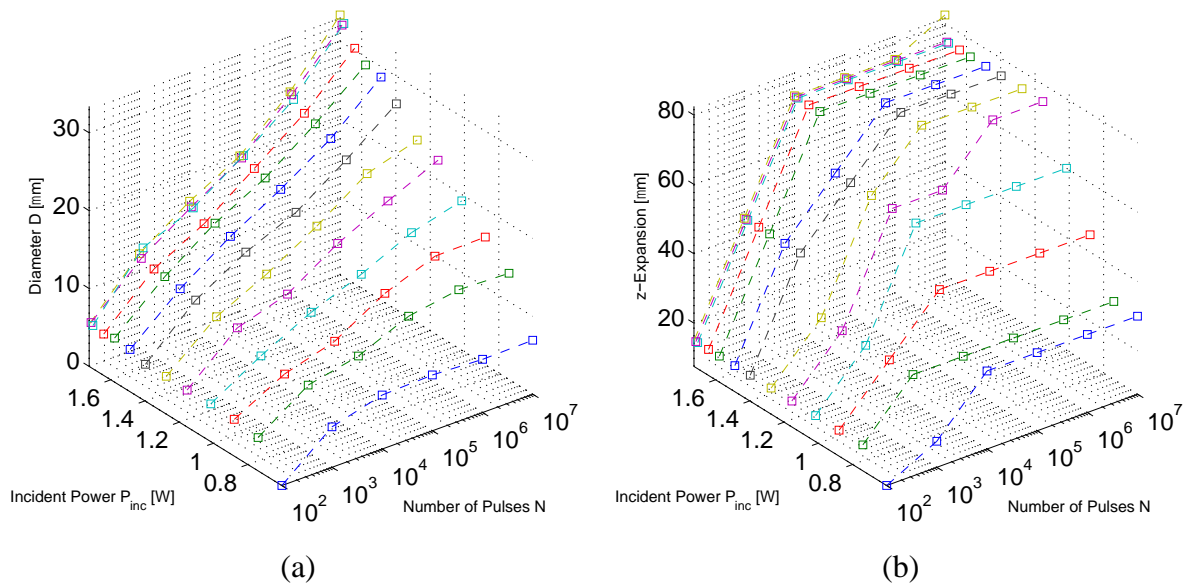
Fig. 5.7 – Measured values for (a) the fusion front diameter and (b) the z-expansion length
for Fused Silica at a objective NA 0.5

The dimensions on the graph in Fig. 5.7 clearly show that the z-expansion length extended
much faster than the fusion front diameter. To demonstrate this even further, Fig. 5.8 depicts a
direct comparison of z-expansion and fusion front diameter for incident average powers of 1.7 W
at NA's of 0.5 and 0.7 respectively. However, for a NA of 0.5 the z-expansion plateaued after
approximately 10^4 pulses at about 75 μm length in axial direction from the focusing plane towards
the incident beam, whereas the fusion front diameter continued to grow exponentially for sufficient
incident average power. At low incident average power the radial expansion also stopped quickly.
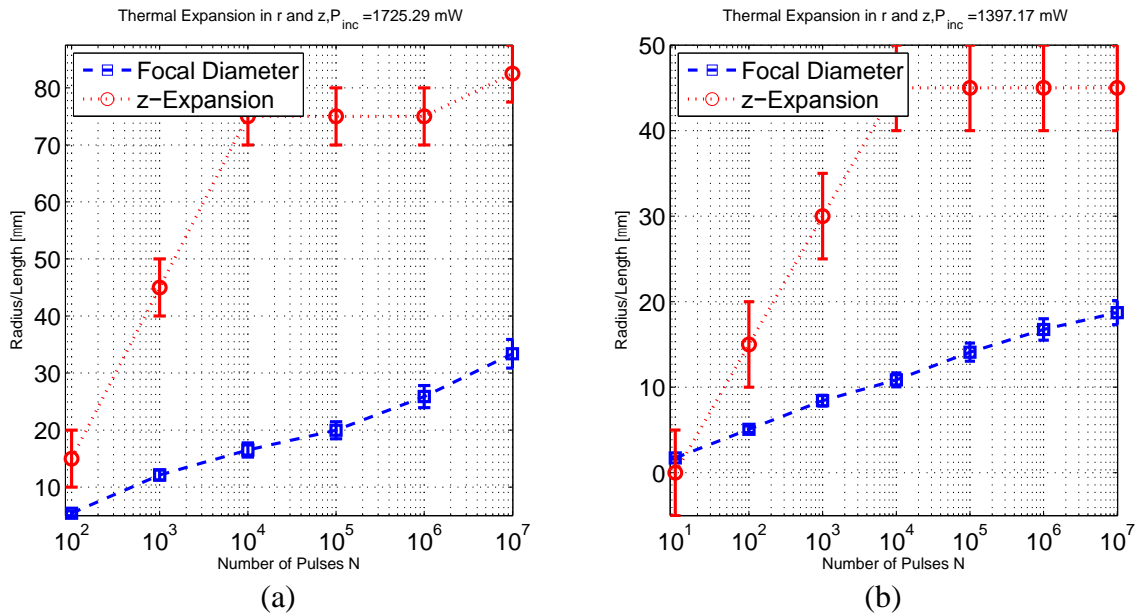
Fig. 5.8 – Comparison of the measured fusion front diameter and z-expansion for (a) NA 0.5 at 1.7 W incident power and (b) NA 0.7 at 1.4 W incident power in Fused Silica

As to the dependence on incident average power (Fig. 5.7), in the case of the z-expansion length, it appears the modification grew linearly with increased power to a maximum value and then plateaued as well. The fusion front diameter also grew linearly but did not reach a maximum value at which the growth stopped.

As the general same trend is observable for a stronger focusing using a NA 0.7 in Fig. 5.9, the z-expansion plateaus much earlier at an axial length of approximately 45 μm. As well as before, the growth of the fusion front diameter here was also exponential with respect to the incident number of pulses, however, at lower incident average power the modification growths plateaus as well as for a NA 0.5.

Fig. 5.9 – Measured values for (a) the fusion front diameter and (b) the z-expansion length
for Fused Silica at a objective Fused Silica NA 0.7

The dependence of the modification size in r- and z-directions as a function of the exposure
time is depicted in Fig. 5.10 for maximal incident average power. Here exposure time is directly
proportional to the number of incident pulses as

$$N_{pulses} = t_{exposure} \cdot f_{rep} \qquad (5.1)$$

The graph of Fig. 5.10(a) shows that the growth of the fusion front diameter was independent of
the repetition rate for $f_{rep} \geq 1\,MHz$. The z-expansion is slightly increased for $1\,MHz$ and
$9.2\,MHz$, as illustrated in Fig. 5.10(b).

In addition, both graphs show that the modification size decreased with repetition rate at low
number of pulses of $N > 10^2$.
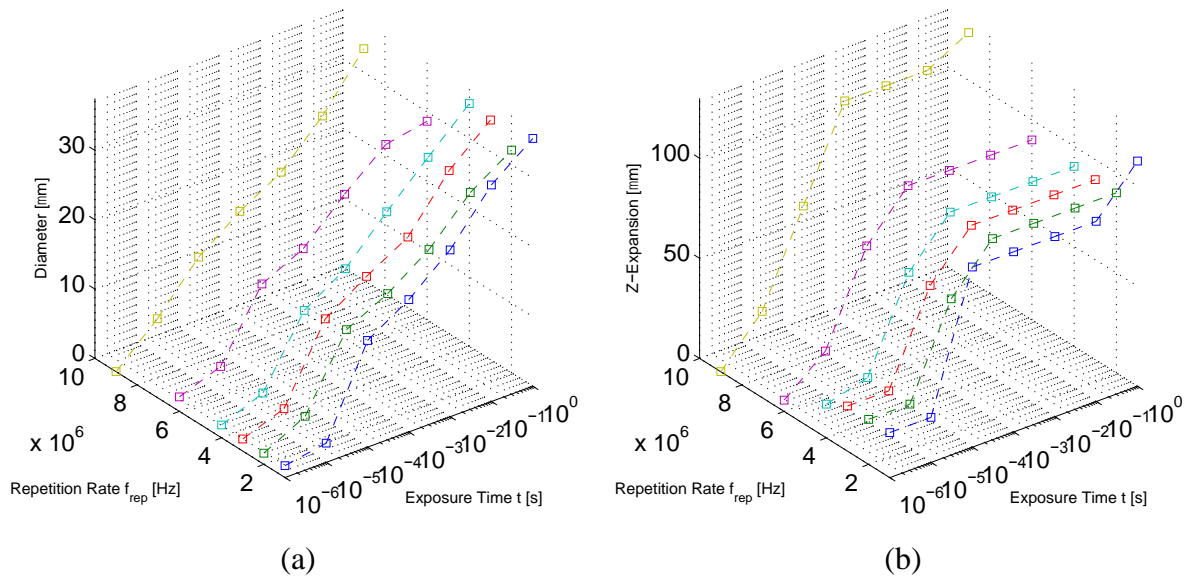
Fig. 5.10 – Graphs of (a) the fusion front diameter and (b) the z-expansion length vs. the pulse repetition rate for maximum incident average power at a NA 0.65 in Fused Silica

From the data in Fig. 5.10 can be concluded that the pulse energy is the driving factor for the modification size at low incident number of pulses. At an increased exposure time, and therefore large number of incident pulses, the heat accumulation effect take over and the modification size becomes solely dependent on the accumulated incident power, and therefore independent of repetition rate.

Applying the technique introduced first by Liu [95], it was possible to estimate the accumulated modification threshold for each modification site as a function of pulse repetition rate and number of incident pulses. Fig. 5.11 (a) shows the fitted graph. Corresponding to each threshold, the light-matter interaction diameter can be estimated, shown in Fig. 5.11(b). This value was a fitting parameter following the approach by Martin [178].
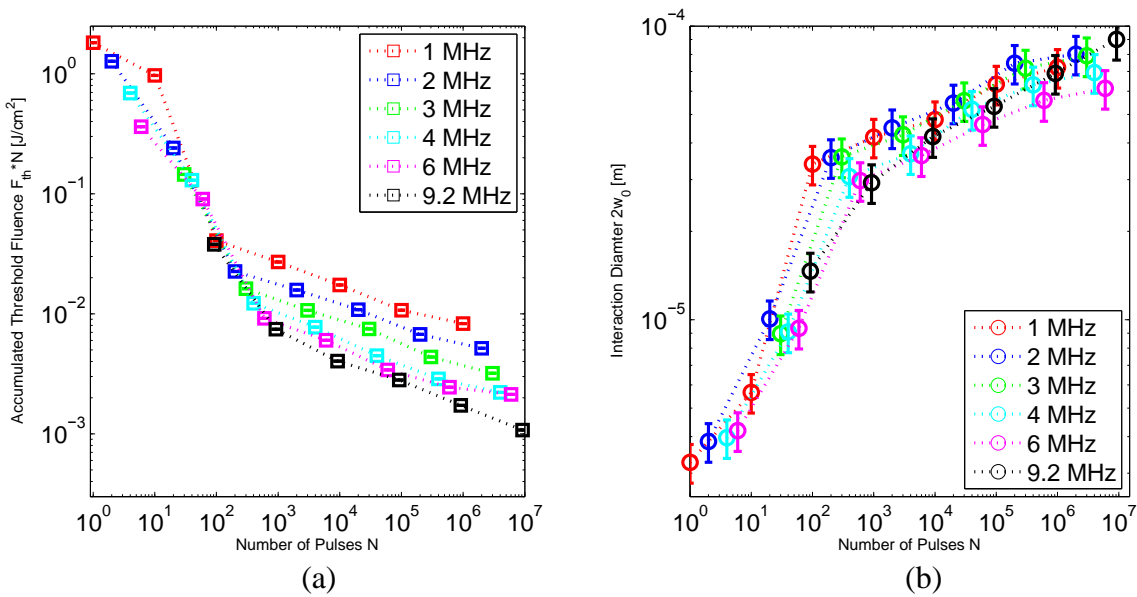
Fig. 5.11 – Fitted graphs of (a) bulk modification threshold fluence vs. the number of incident pulses for various repetition rates and (b) the corresponding interaction diameter in Fused Silica

Fig. 5.11(a) clearly shows that the threshold decreases with increased number of incident pulses of up to approximately $200 - 500$ independently of repetition rate. For a larger number of pulses the thresholds still decrease but with individual tracks for each repetition rate. Thereby, higher repetition rates lead to lower threshold fluences. The slope of the tracks is similar between the repetition rates. At the same time, the interaction diameter grew very quickly within approximately the first 500 pulses, after which the increase slows down significantly.

Jee *et al.* [179] reported prior that a function of the form

$$F_{th}\left(N\right) = F_{th}(1) \cdot N^{\xi-1}, \tag{5.2}$$

describes the dependence of the accumulated threshold fluence on the number of incident pulses. This function will not fully describe the results observed here for Fused Silica in the heat

accumulation regime. In fact, a super-position of two such functions would describe the system more accurate

$$F_{th\,1}\,(N) = F_{th\,1}(1) \cdot (N)^{\xi-1},$$ (5.3)

$$F_{th\,2}\,(N) = F_{th\,2}(1) \cdot (N)^{\varsigma-1}.$$ (5.4)

Miyamoto *et al*. [180], [181] reported a model at which the absorption scheme changes from a non-linear absorption regime for low repetition rates to a quasi-linear absorption regime at high repetition rate. The model suggests that the electron plasma will not decay in between pulses. The quasi-linear absorption at high repetition rates is then due to electron heating of the hot plasma in the absorption volume of the previous pulse. The suggested model also predicted the increased growth of the z-expansion towards the incident beam as observed in Fig. 5.8.

If one assumes the validity of the model suggested by Miyamoto then set of equations represents the slopes of the graph in Fig. 5.11(a) with Equ. (5.3) describing the threshold characteristics in the low repetition rate (non-HA) regime and Equ. (5.4) describing the threshold characteristics in the high repetition rate (HA) regime. It becomes then also apparent that $F_{th\,1}(1)$ and $F_{th\,1}(1)$ are the threshold fluences for the non-HA regime and the HA-regime in $[\frac{J}{cm^2}]$, respectively. A line fit of each regime is shown in Fig. 5.12. The fitting parameters used in Equ. (5.3) and (5.4) were $F_{th\,1}(1) \approx 1.51 \pm 0.44\,Jcm^{-2}$ and, listed as vector for the different repetition rates, $F_{th\,2}(1) = [0.071; 0.05; 0.041; 0.034; 0.027; 0.023]\,Jcm^{-2}$. $F_{th\,2}(1)$ clearly showed the reduced threshold fluence value for higher repetition rates suggesting the quasi-linear absorption scheme.
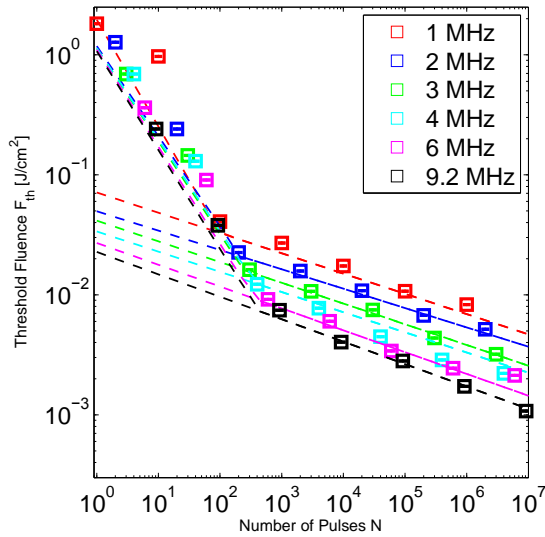
Fig. 5.12 - Graph of fitted threshold fluences functions according to Equ. (5.3) and (5.4) on Fused Silica for different pulse repetition rates

5.3.1.2 Aluminumsilicate glass EAGLE2000®

The previous established general dependencies of the fusion front diameter and z-expansion with respect to number of incident pulses and average power is also apparent in this aluminumsilicate glass, shown in Fig. 5.13. Again, the z-expansion (Fig. 5.13(b)) grew at a higher rate than the fusion front diameter (Fig. 5.13(a)). Due to the reduced bandgap energy the modification occurred at lower average power than in Fused Silica.
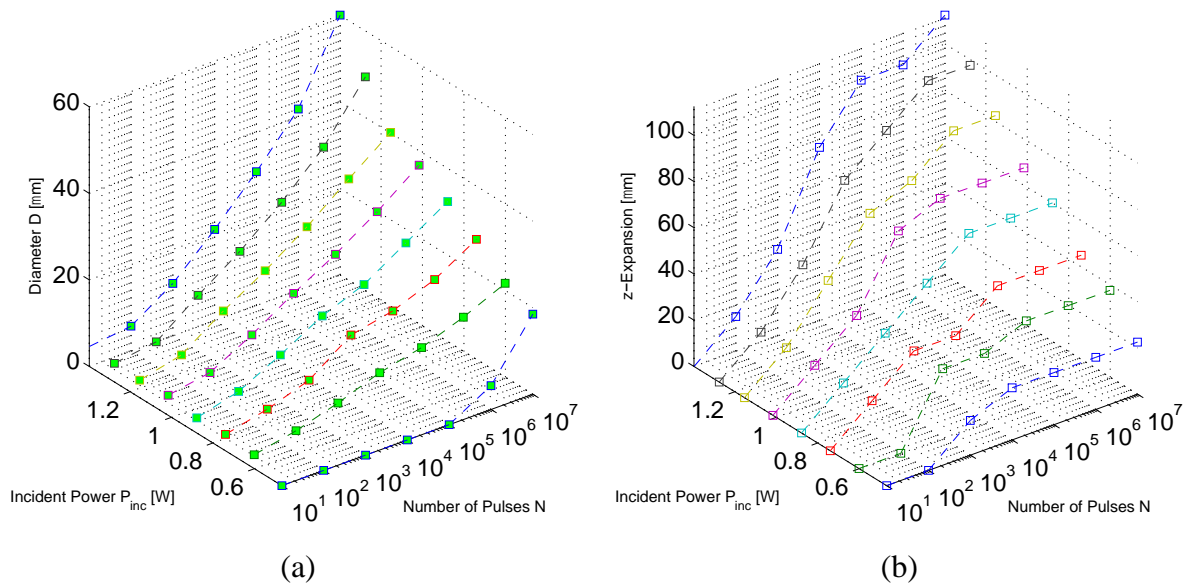
Fig. 5.13 – Measured values for (a) the fusion front diameter and (b) the z-expansion length for EAGLE2000® at a objective NA 0.5

Due to the increased thermal conductivity, the growth of the modified volume was faster than seen previously in Fused Silica. Fig. 5.13(a) shows a hyper-exponential growth with the number of incident pulses and a non-linear growth with incident average power. The z-expansion overall did not saturate with respect to the incident average power and the here-applied processing window as seen in Fused Silica. On the contrary, saturation of the modification size takes place quickly with respect to the number of pulses at lower average powers and becomes less prominent at higher powers.

The fusion front diameter was, as well as in Fused Silica, independent on the pulse repetition rate, depicted in Fig. 5.14(a). The z-expansion length occurs to have no functional dependence within the frame of the here-applied parameters, but overall follows a similar shape, shown in Fig. 5.14(b).
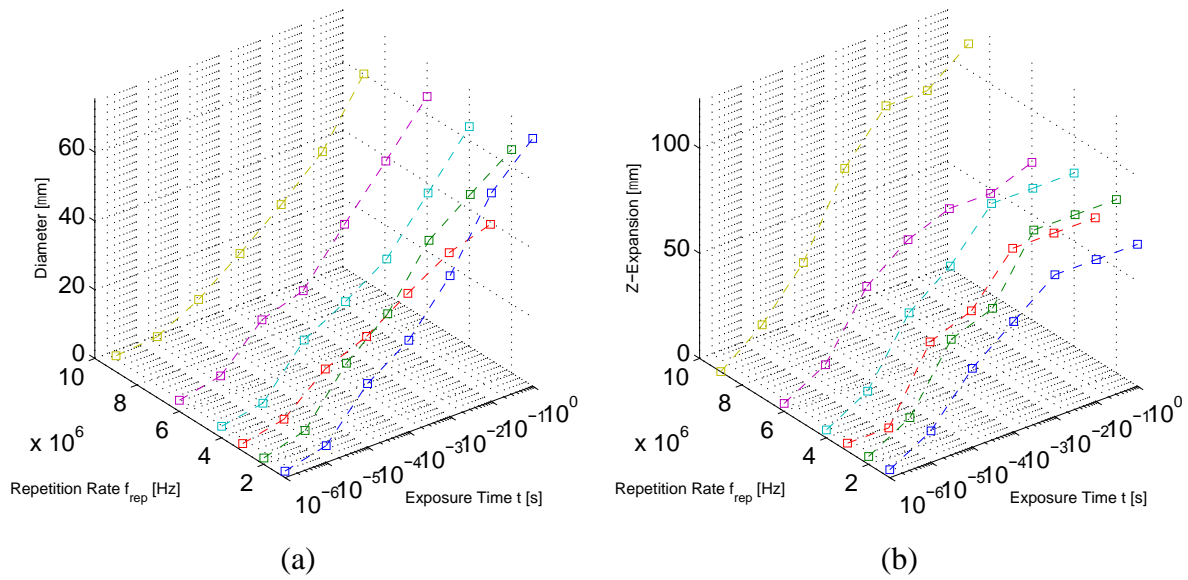
Fig. 5.14 – Graphs of (a) the fusion front diameter and (b) the z-expansion length vs. the pulse repetition rate for maximum incident average power at a NA 0.65 in EAGLE2000®

Fig. 5.15 illustrates the dependence of (a) the modification threshold fluence and (b) the corresponding laser-matter interaction diameter with respect to the number of incident pulses for varying pulse repetition rates. The clear shoulder, which was very apparent in the case of Fused Silica, is less obvious here. The cause for this is the increased heat conductivity in aluminumsilicate glass, and therefore the reduced heat diffusion time out of the focal volume. A graph of the fitted slopes according to Equ. (5.3) and (5.4) is shown in Fig. 5.1.
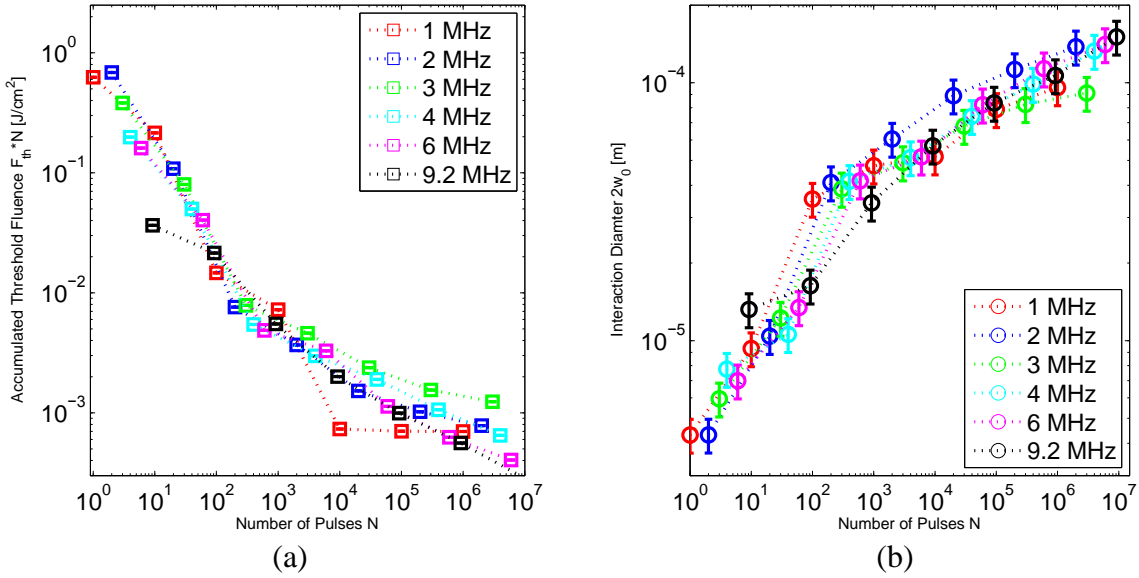
Fig. 5.15 – Fitted graphs of (a) bulk modification threshold fluence vs. the number of incident pulses for various repetition rates and (b) the corresponding interaction diameter in EAGLE2000®

The fitting parameters used were $F_{th\,1}(1) \approx 0.72 \pm 0.42\, Jcm^{-2}$ and, listed as vector for the different repetition rates, $F_{th\,2}(1) = [0.044; 0.049; 0.03; 0.027; 0.035; 0.03]\, Jcm^{-2}$.

It is worth noting that the threshold fluence for the non-HA regime decreased almost one order of magnitude but the threshold fluences for the HA regime were almost the same as observed in Fused Silica. That further supports the claim that the absorption scheme is material independent at high laser pulse repetition rates as it would be the case for electron heating.
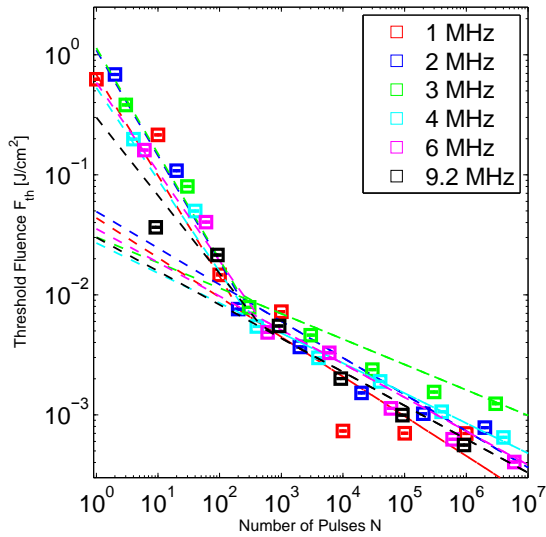
Fig. 5.16 – Graph of fitted slopes to the threshold fluence functions according to Equ. (5.3) and (5.4) on EAGLE2000® for different pulse repetition rates

5.3.1.3   FOTURAN®

In FOTURAN® the same general trend as established in the former materials was apparent, where the expansion in the propagation direction of the beam is much faster than the growths in the orthogonal plane, depicted in Fig. 5.13. Similar to aluminumsilicate glass the z-expansion had no clear saturation point within the here applied process parameters. Moreover, the growth of the fusion front due to the number of incident pulses is also hyper-exponential.

Fig. 5.18 depicts (a) the modification threshold fluence dependent on the number of incident pulses and (b) the corresponding light-matter interaction diameter at a pulse repetition rate f_{rep} of 9.2 MHz. The onset of the bend in the slope of the modification threshold occurred at approximately 10^5 accumulated pulses.
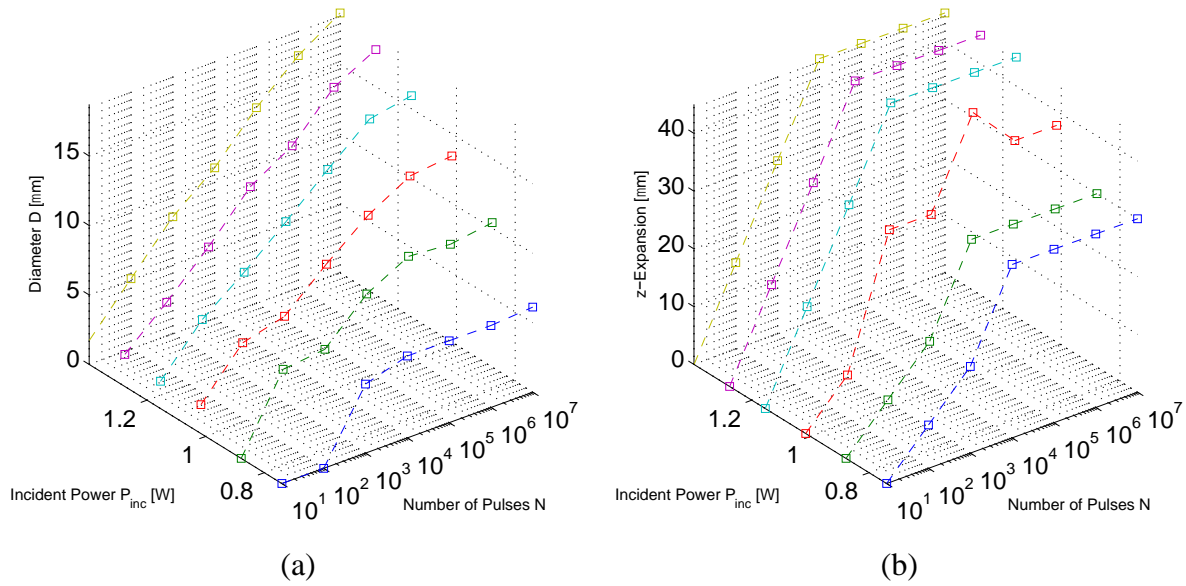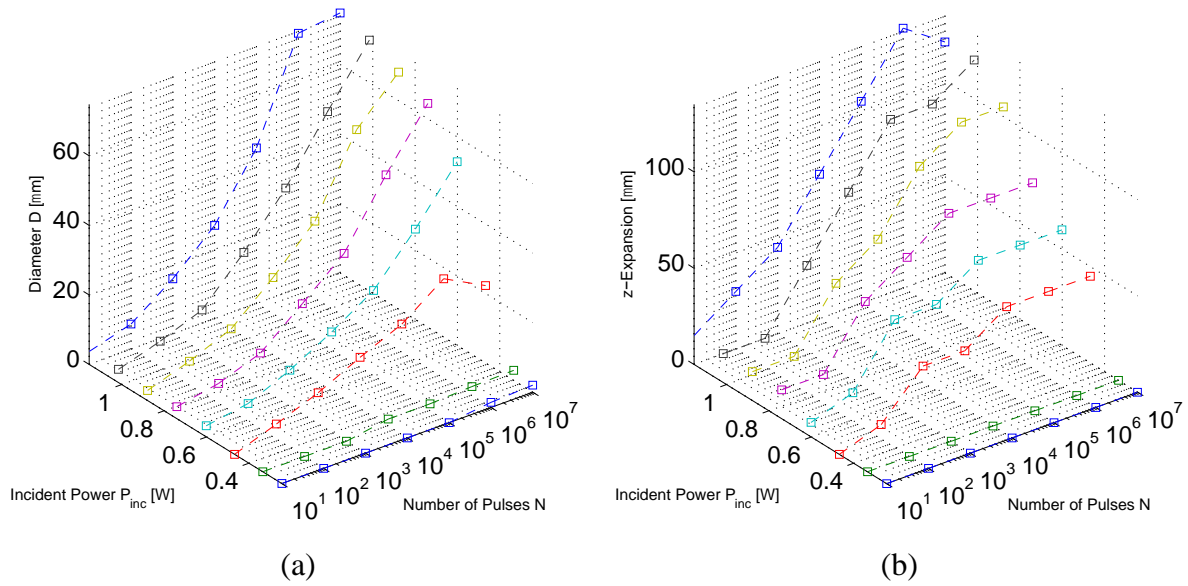
Fig. 5.17 - Measured values for (a) the fusion front diameter and (b) the z-expansion length

for FOTURAN® at an objective NA 0.5
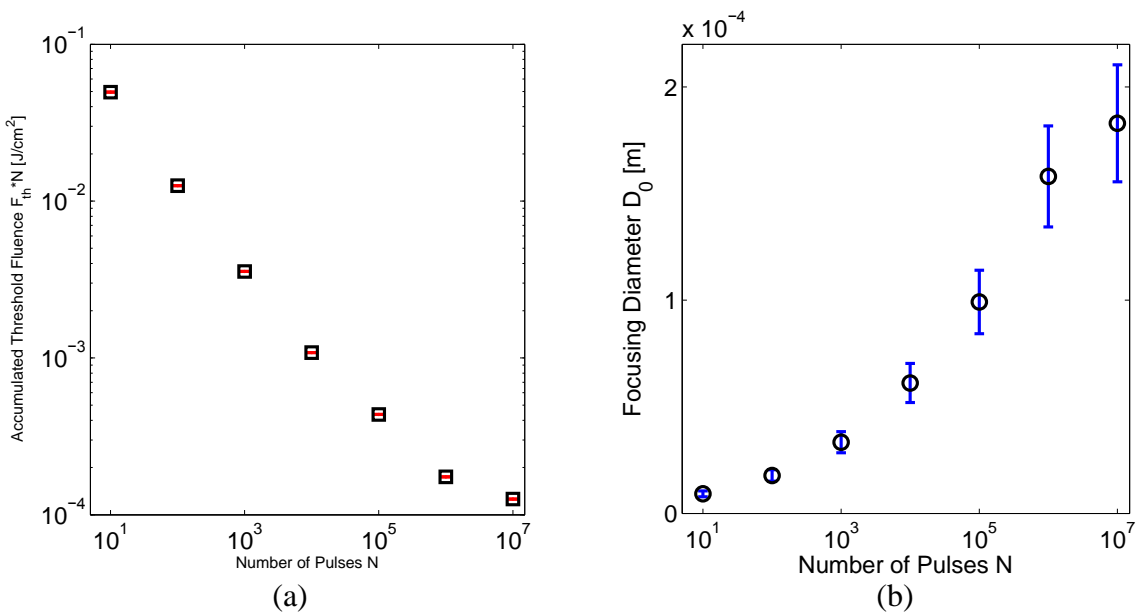
Fig. 5.18 - Graphs of (a) modification threshold fluence and (b) the corresponding light-

matter interaction diameter at a pulse repetition rate f_{rep} of 9.2 MHz in FOTURAN®

Fig. 5.19 depicts the fitted slopes to determine the threshold fluence for non-HA and HA regime. The fitting parameters used were $F_{th\,1}(1) = 0.13\,Jcm^{-2}$ and $F_{th\,2}(1) = 0.0015\,Jcm^{-2}$. These fluences are one order lower than observed for Fused Silica or EAGLE2000®. The cause was believed due to the low number of data points to determine the slope for the HA regime.
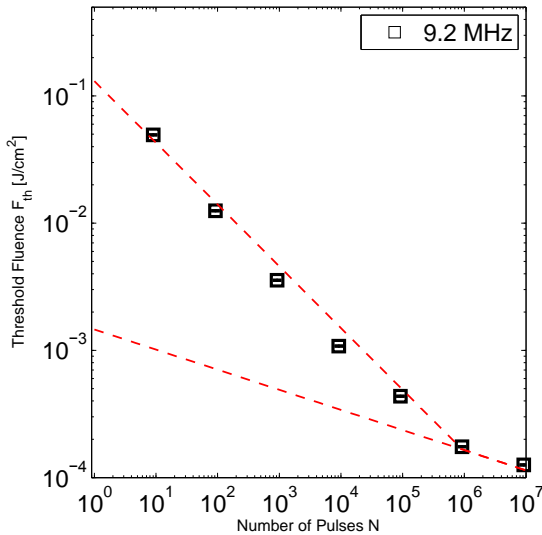
Fig. 5.19 - Graph of fitted slopes to the threshold fluence functions according to Equ. (5.3) and (5.4) on FOTURAN® at $f_{rep} = 9.2\,MHz$

5.3.1.4 Fused Quartz and Sapphire

In the cases of Fused Quartz and Sapphire no evidence of a fusion front was found, as the DIC images shown in Fig. 5.20 illustrate. The materials possess a very high thermal conductivity due to the crystalline lattice structure. This is assumed to result in the thermal energy being dissipated out of the focal region faster than the pulse-to-pulse time.
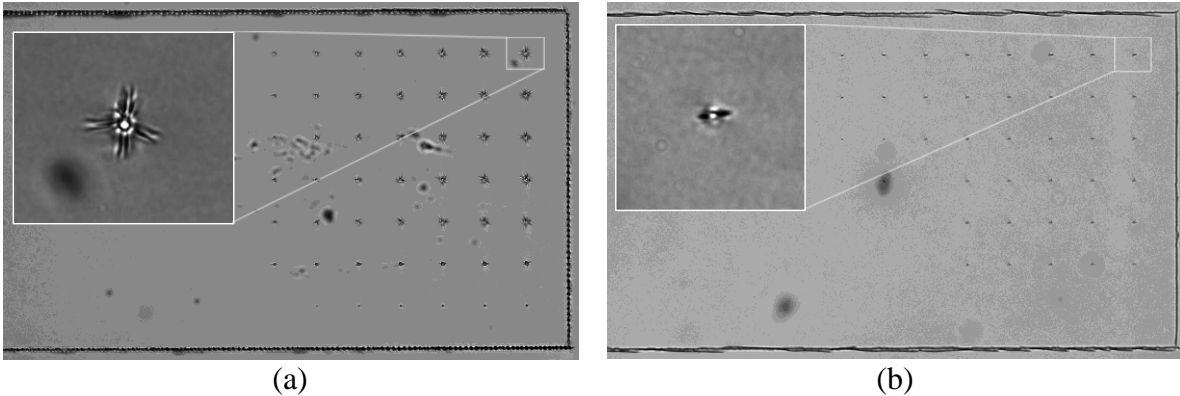
Fig. 5.20 - DIC images of (a) Fused Quartz and (b) Sapphire irradiated with high repetition rate fs-pulse trains; insets are magnified views of single irradiation sites, there is no evidence for the previously found fusion front

5.3.1.5   Radial Fusion Front Expansion

Using the model introduced in Chapter 472.2.7 for the accumulated heat in the focal volume, the expansion of the fusion front can be simulated. Fig. 5.21 shows the computational results (dashed lines) and the actual measured fusion front radii (circles) for Fused Silica, FOTURAN®, and EAGLE2000® at a pulse repetition rate of $9.2\ MHz$ when the maximum pulse energy suitable for the sample material was applied. Within each simulation the fusion front radius at each time step was assumed to be the radial point at which the local temperature reached melting temperature for the particular material.

The simulated radii of the fusion front were approximately two- to threefold overestimated even though the general trend can be seen. The reason for this overestimation is that the heat diffusion D was set as a constant; however, at such large changes in temperature this assumption will not hold.
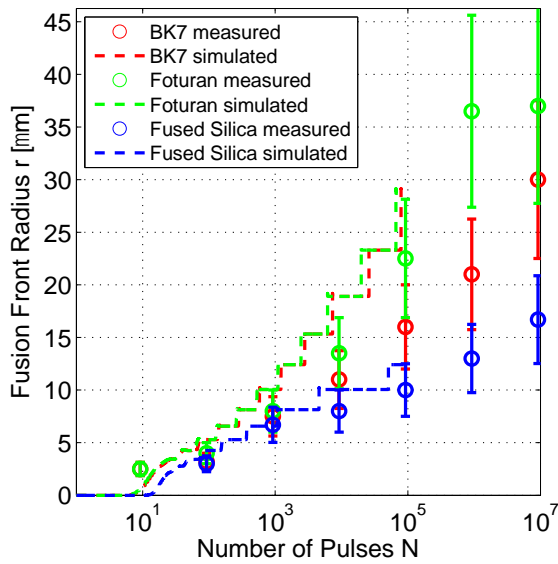
Fig. 5.21 – Graph of the Fusion Front expansion: Model vs. Measured Results

5.3.1.6 Nano-Fibers in the Confocal Microscope

If nano-fibers are formed on the surface of the irradiated sample they are visible under the confocal microscope as blurry string-like shadows. An example of such surface images is shown in Fig. 5.22. The red arrows in the image point towards the nano-fibers standing up from the sample surface.
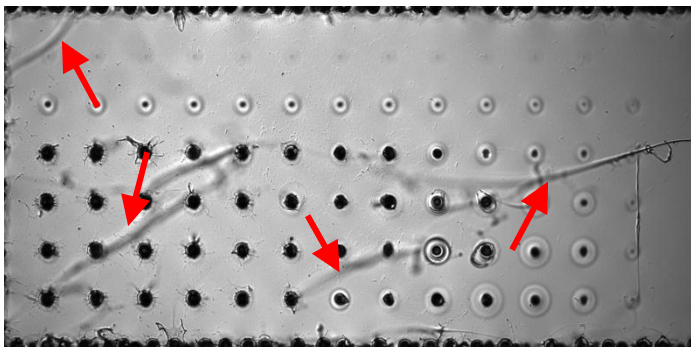
Fig. 5.22 - DIC microscope image of irradiated area on a Fused Silica sample, red arrows point to nano-fiber

Because of the dimensions of the nano-fibers, SEM was necessary to resolve their features. The result of SEM measurements will be detailed after the summary of the confocal microscopy.

5.3.1.7   Summary Confocal Microscopy

In summary it was found that there is an increased growth rate in axial z-direction towards the incident beam compared to the growth rate in the orthogonal radial plane. This results were in agreement with Miyamoto as well as Richter *et al*. [182], which both reported increased growth in the beam direction when using high repetition rate pulse trains. Moreover, for the first time there is clear evidence that supports a model based on a change in the absorption scheme when utilizing sufficient pulses at high repetition rates. It was shown that the slope of the threshold fluence decreased by two orders of magnitude when a quasi-linear absorption scheme due to electron heating becomes effective.

In addition, a thermal diffusion model based on HA effects within the focal volume was developed and produced good agreement with the measured result of the fusion expansion diameter.

5.3.2   Scanning-Electron Microscopy

Do to the small diameter of the nano-fibers, in the range of approximately $100\ nm$, SEM images were taken of the irradiated sample surfaces. It should also be pointed out, that the interest in this study lies on fibers originating from an intact sample surface and not resulting from a material surface explosion.

Four out of the five investigated materials developed nano-fiber, Fused Silica, Fused Quartz, EAGLE2000® and FOTURAN®, as depicted in Fig. 5.23. That also coincided with the simulation

result using the heat diffusion model (compare Chapter 2.2.7), in which the four materials that developed nano-fibers also reached melting temperature in the focal volume, shown in Fig. 5.24.
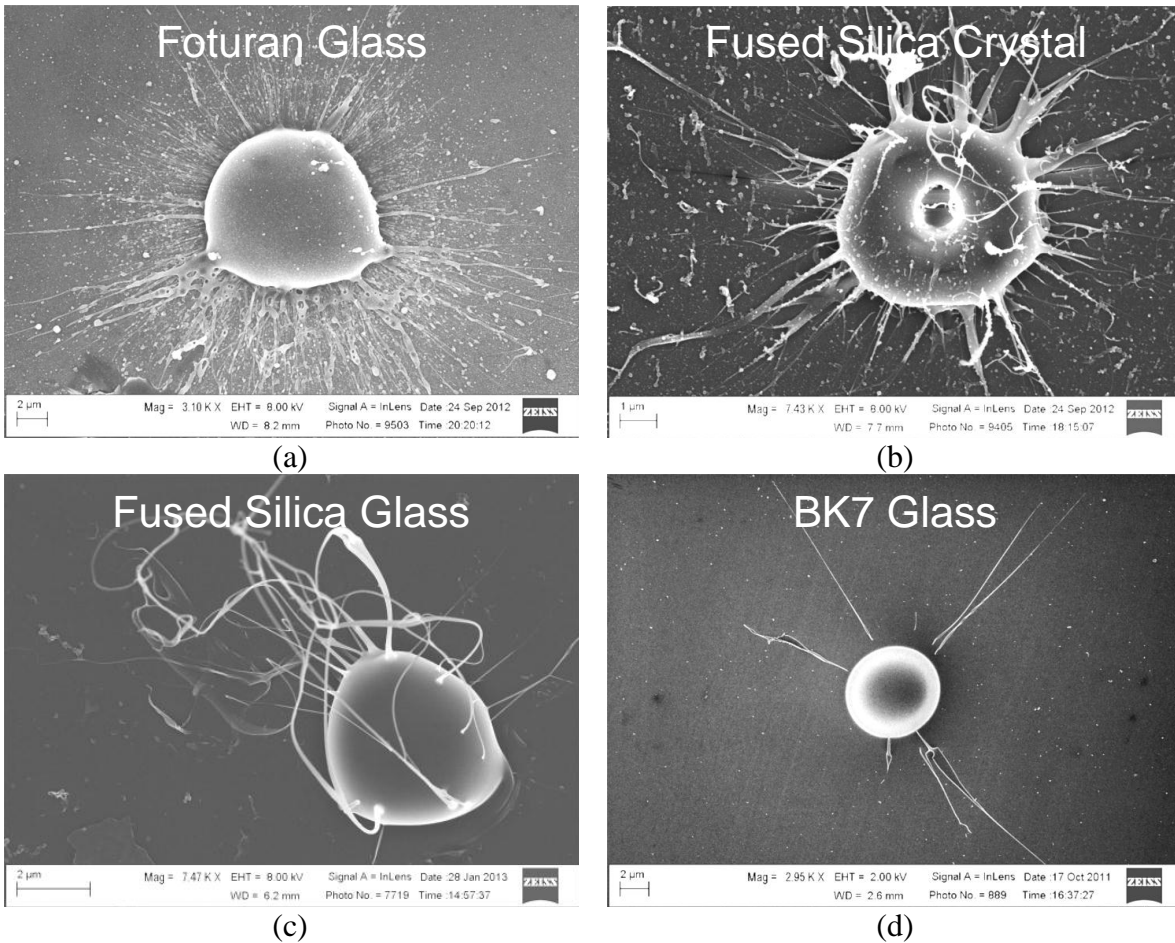
Fig. 5.23 - SEM images of nano-fibers formed on the surface of (a) FOTURAN® glass, (b) Fused Quartz, (c) Fused Silica glass and (d) EAGLE2000®

The maximal achievable aspect ratio of the nano-fibers varied greatly with the base material from approximately $1:100$ for FOTURAN® to over $1:1000$ for Fused Silica.
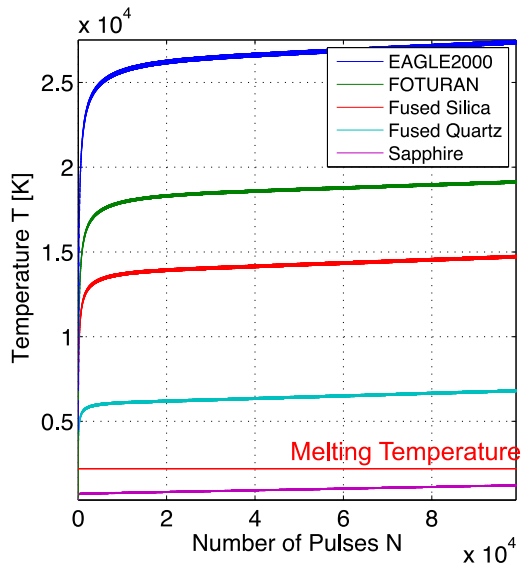
Fig. 5.24 - Graph of the simulated temperature at $r = w_0$ for investigated materials

Due to the nature of the SEM acquisition, all dielectric samples had to be coated with Palladium to allow the surface to become conducting and therefore prevent charge build-up during the image acquisition. Due to the coating process, many of the former free-standing nano-fibers became attached to the sample surface. However, in a few cases the nano-fiber did not attach to the sample surface, which allowed them to move around under the influence of the E-field during the image acquisition. This movement is shown in the series of SEM images in Fig. 5.25, and taken as proof that the nano-fibers indeed are freestanding.

<div align="center">(a)   (b)   (c)   (d)   (e)</div>
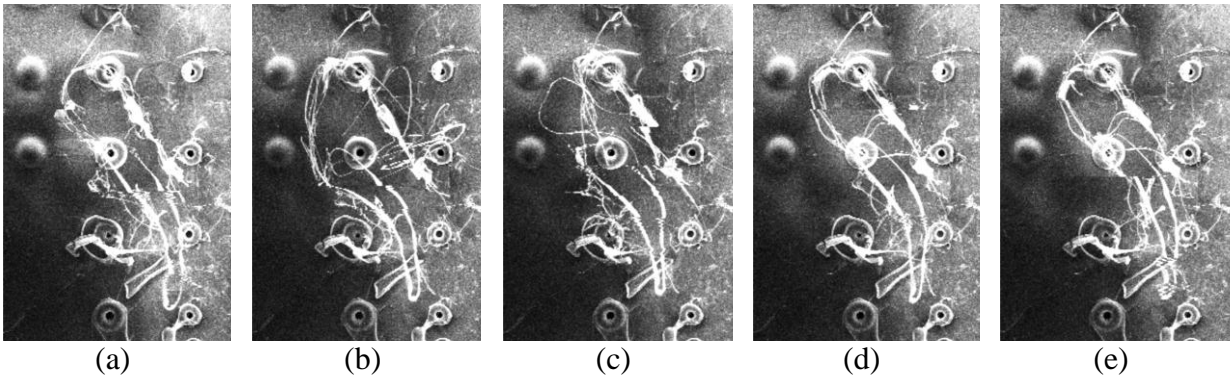
Fig. 5.25 - Series of SEM images of the surface of irradiated Fused Silica with moving
nano-fibers

As previously stated, the aspect ratio of the nano-fibers greatly depended on the sample material. It is noteworthy that the width of the nano-fiber did not vary as much; it was determined to be between approximately $50\ nm$ and $150\ nm$. Therefore, the major difference between the nano-fibers formed on different materials was their length. Table 5-4 lists the general found features.

Table 5-4 - Characteristic features of the nano-fibers for investigated materials

Material	Avg. width	Avg. length	Aspect Ratio
FOTURAN®	~ 150 nm	~ 15 mm	1:100
Quartz Crystal	~ 50 nm	~ 10 mm	1:200
EAGLE2000®	~ 125 nm	~ 30 mm	1:250
Fused Silica	~ 50 nm	~ 60 - 90 mm	> 1:1000
Sapphire	No nano-fibers formed		

5.3.2.1 Extreme Fiber-Aspect-Ratio in Fused Silica

To illustrate the extraordinary nano-fiber aspect ratio resulting from the irradiation of Fused Silica, Fig. 5.26 depicts some of the found fiber formations. The nano-fiber in Fig. 5.26 (a) was generated at a pulse repetition rate of $f_{rep} = 3\ MHz$ at a focusing depth of $t_{focus} = 20\ \mu m$. It has an approximately length $l_{fiber} \approx 180\ \mu m$; the inset shows a magnified view of the fiber depicting its width is approximately $w_{fiber} \approx 100\ nm$. Therefore the aspect ratio of this particular nano-fiber is 1:1800. Fig. 5.26 (b), (c), and (d) show that the width of the nano-fiber stays approximately constant over its full length. The fiber was generated at $f_{rep} = 1\ MHz$ at a focusing depth of $t_{focus} = 10\ \mu m$. At the root, Fig. 5.26 (c) the fiber-width is approximately $w_{fiber} \approx 100\ nm$, at its mid-section, Fig. 5.26 (d), the fiber became only marginal smaller to a width of approximately $w_{fiber} \approx 80\ nm$.
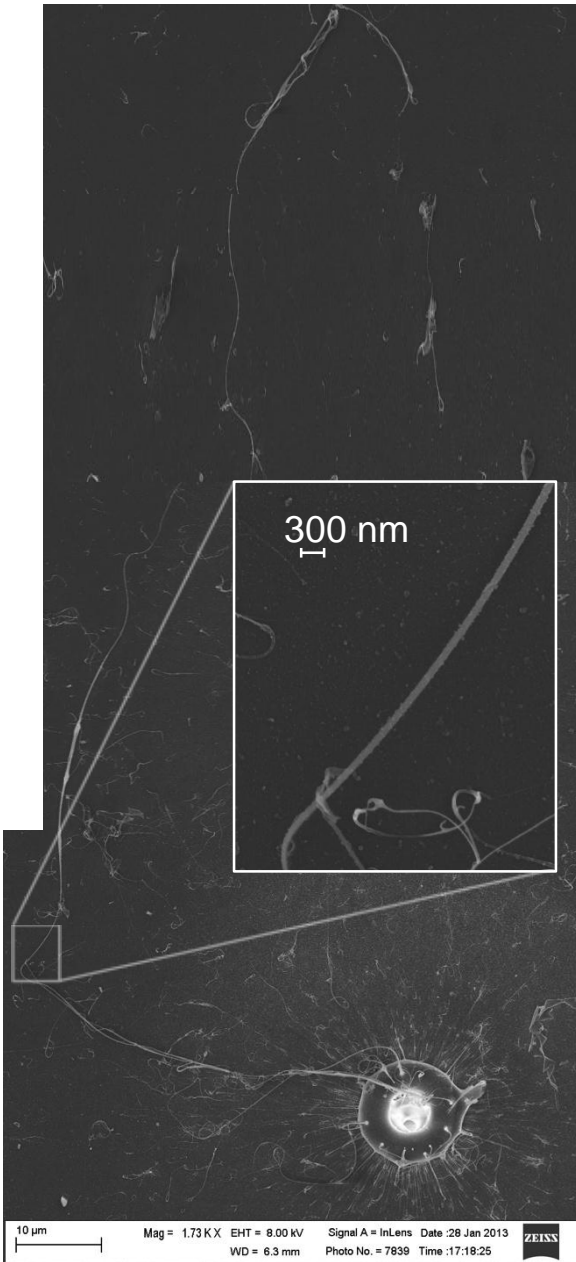
(a)
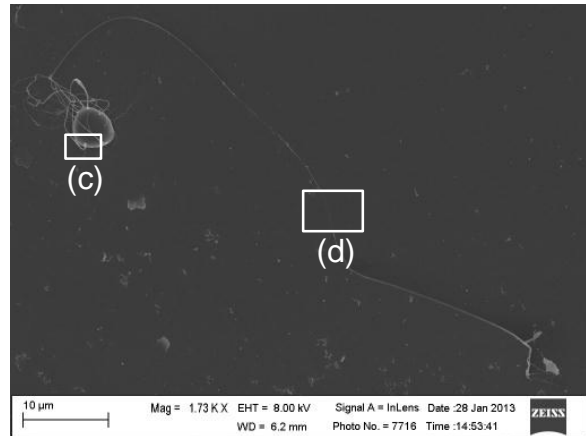
(b)
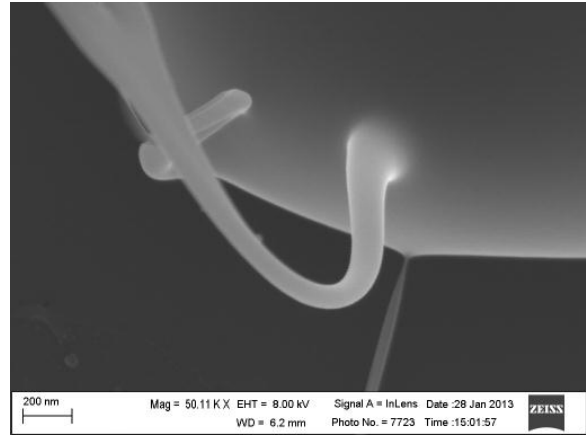
(c)
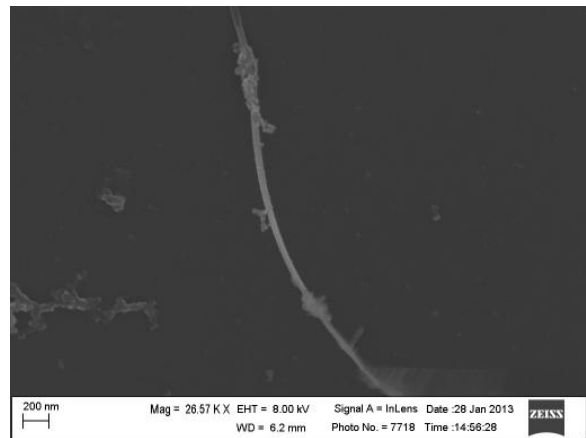
(d)

Fig. 5.26 - SEM images showing the extra-ordinary large nano-fiber aspect-ratio

5.3.2.2 Curled Nano-Fibers in EAGLE2000®

Most of the observed nano-fibers did not show any signs of torsion, however, several nano-fibers found in aluminumsilicate glass EAGLE2000® curled during their formation, as shown in Fig. 5.27. The nano-fibers shown in Fig. 5.27(a) resulted from irradiation with a repetition rate of $f_{rep} = 1\ MHz$ at a focusing depth $t_{focus} = 20\ \mu m$ in an external electric field of $E_{external} = 1\ kV$. Fig. 5.27(b) was generated at the same repetition rate and focusing depth with no external electric field applied. Therefore it is concluded that the external field is not the cause for the curling effect of the produced nano-fiber.
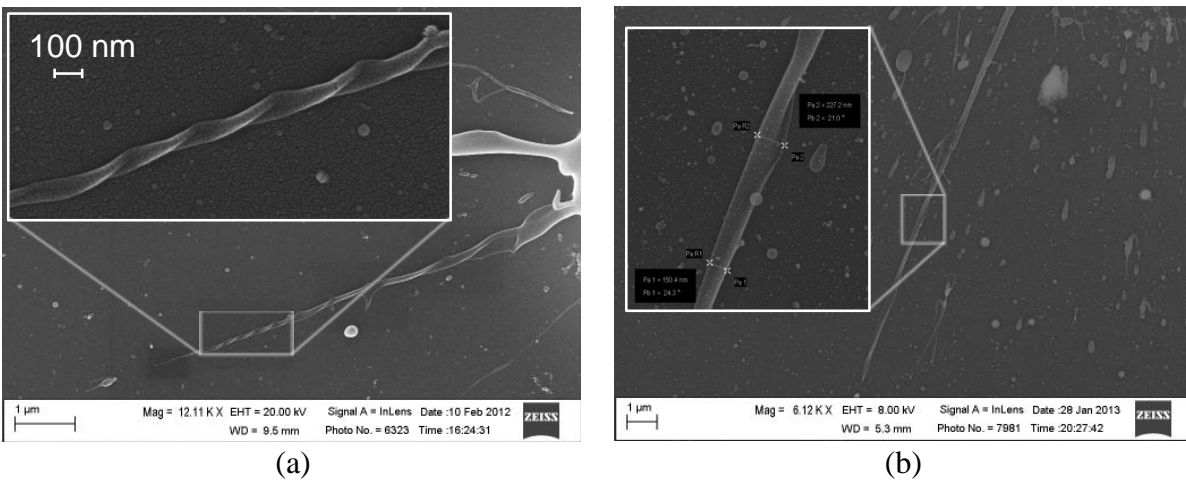
Fig. 5.27 – SEM images of curled nano-fibers in EAGLE2000®, (a) under application of

$1\ kV$ external DC field, and (b) without any external field

5.3.2.3 Crystal-formation on FOTURAN®

FOTURAN® glass contained 0.5% atomic volume silver dopant. After the irradiation of the sample, crystal-like structures were found on several of the irradiated surface, depict in Fig. 5.28. Both spots featured here were irradiated with a pulse repetition rate of $f_{rep} = 9.2\ MHz$ at a

focusing depth $t_{focus} = 20 \, \mu m$. The incident average power in Fig. 5.28(a) was $P_{avg} = 0.5 \, W$, and in Fig. 5.28(b) $P_{avg} = 1.15 \, W$.

(a)   (b)
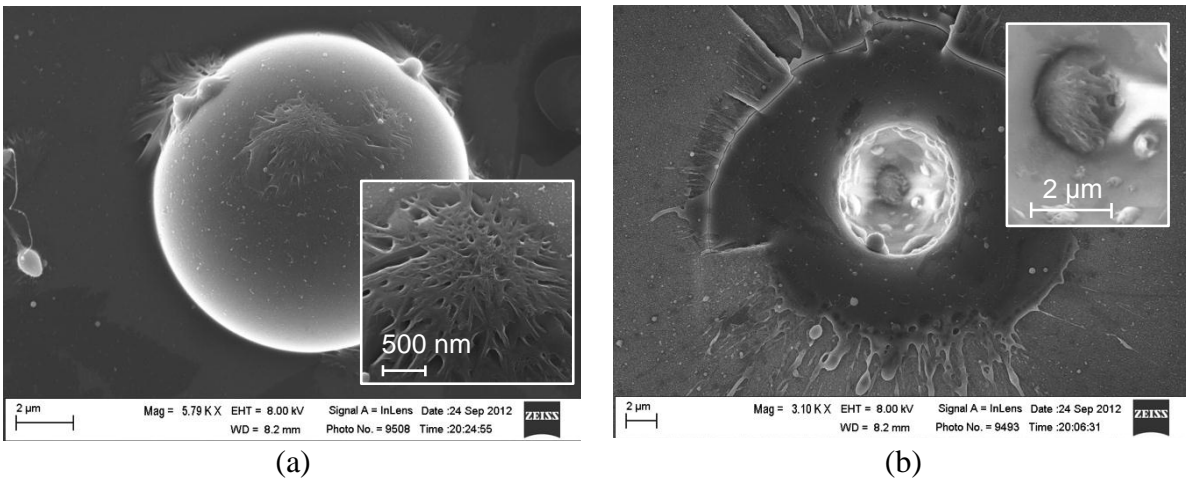
Fig. 5.28 - SEM images of crystal-formation on (a) a bubble surface and (b) a crater bottom on FOTURAN®

From the SEM images obtained it is unclear, if the formed structure indeed is a silver-nano-crystal or a crystallized glass.

5.3.2.4 Nano-fiber formation in Fused Quartz

Even though Fig. 5.23(b) depicted the formation of the desired nano-fibers on irradiation sites in Fused Quartz, many of the fiber-like formation in this material appear different, as shown in Fig. 5.29. Here the structures seem to originate from a larger erupting bubble and then solidified in air.
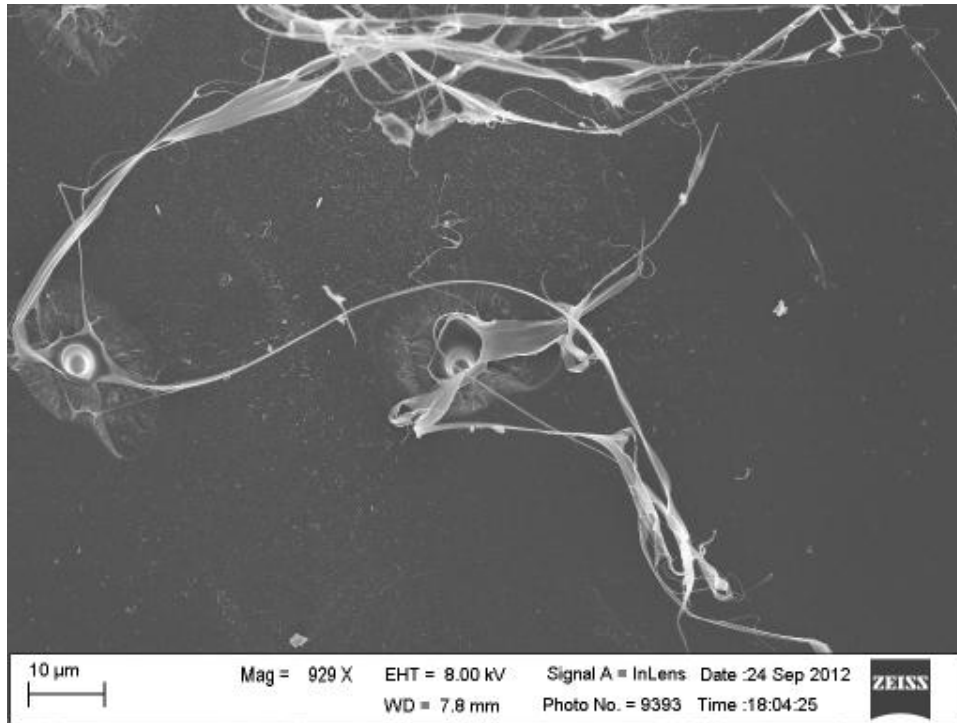
Fig. 5.29 - SEM image of fiber-structures on a Fused Quartz sample

5.3.2.5 Dependence on Focusing Depth

Three general different cases for the formation of nano-fibers could be observed, depending on the focusing depth with respect to the sample surface. In the first case, the laser focus was positioned very shallow below the sample surface. This led to a cap of material being removed of the surface like a chip, with the possibility of forming some low aspect-ratio nano-fibers in the resulting crater, shown in Fig. 5.30(a). If the focus was set deeper into the bulk material to a medium focusing depth, the second case became apparent. In such case, a bubble like feature develops on the surface, from which high aspect-ratio nano-fibers formed. In some instances, the bubble stood intact, as illustrated in Fig. 5.23(c), in other instances the bubble collapses and caved inwards, shown in Fig. 5.30(b). In the last case at large focusing depth, a large bubble developed

on the surface with no evidence of nano-fibers, shown in Fig. 5.30(c). The here shown image is of an erupted bubble, however, in many instances, the bubble stood intact.

(a) (b) (c)
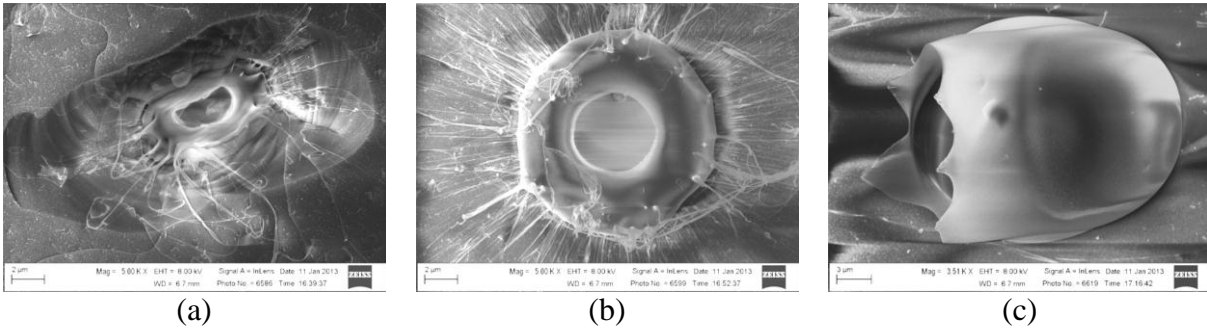
Fig. 5.30 - SEM images of the irradiation sites depending on focusing depth, (a) shallow, (b) medium and (c) large focusing depth

5.3.2.6 Evidence of gaseous phase

To compare the formation of the nano-fibers in the here presented process of femtosecond bulk irradiation with the reports shown by Quintero *et al.* [174], a gaseous phase has to be present during the formation process. It should be pointed out, that there was evidence of such gaseous phase being present at some stage of the irradiation process. As shown in Fig. 5.31, the bubble formed on the surface appears to have erupted from the inside out, especially evident in the magnified image in Fig. 5.31 (c). The SEM images clearly depict the flap of material folding outwards.

(a)	(b)	(c)
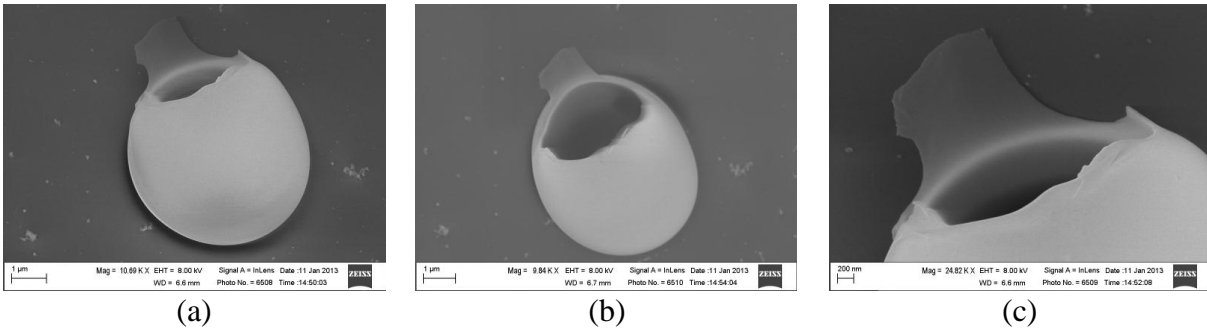
Fig. 5.31 - SEM images of a erupted bubble after femtosecond irradiation of the bulk material, (a) top-view, (b) 30o angled top-view and (c) magnified top-view

On the contrary, there was no evidence found that the nano-fibers are drawn from a gas-jet originating from within the bulk material. At some irradiation sites, the nano-fibers are broken off at their root, allowing observation of the cross-section at high magnification, as depicted in Fig. 5.32. There was no air-channel or gap visible after the fiber was formed.
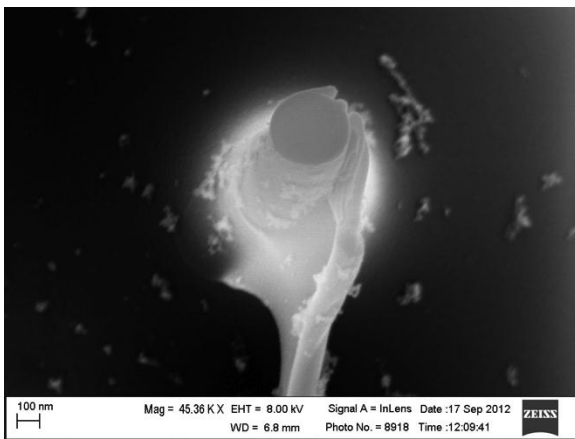
Fig. 5.32 - Image of the cross-section of a nano-fiber that was broken of close to its root

To investigate the structure and possible hollow core of the fiber in more detail, TEM images of single fiber were taken. The next section details the TEM observations.

5.3.3 Transmission Electron Microscopy

The crystalline structure of the nano-fibers is of special interest to determine the formation mechanism. TEM was used to investigate the lattice structure of single nano-fibers.

Fig. 5.33(a) shows that the fibers are solid. There was no hollow inner core apparent in the nano-fiber depicted. A magnified view, Fig. 5.33 (b), revealed the lattice structures of the fiber. It appears to be completely amorphous, as the 2D Fourier-transformed image, Fig. 5.33(c) shows.

| (a) | (b) | (c) |
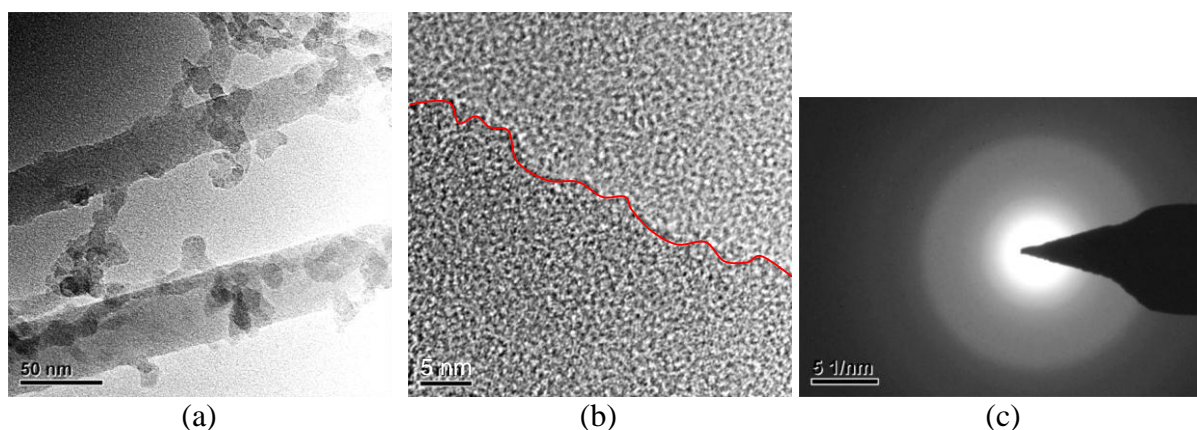
Fig. 5.33 - TEM images of the nano-fibers, (a) 2 separated fibers in overview image, (b) magnified images of a single nano-fiber structure, and (c) the 2D Fourier-transformed image of (b)

Extremely high cooling rates had to be present to (i) prevent break up of the fiber [172] and (ii) preserve the amorphous lattice structure after the solidification process [174], [183]. Therefore, it can also be assumed that a hollow core inside the fiber would have been preserved.

5.3.4 Nano-Fiber Aspect-Ratio Development

In the following, the development of the nano-fiber aspect-ratio due to changing irradiation parameters will be discussed.

The largest aspect-ratio was achieved on Fused Silica surfaces for a focusing depth of $f_{focus} \approx$ 30 μm. When the focusing depth was changed to shallower or deeper positions, the generated nano-fibers were reduced in length. The nano-fiber width, however, remained constant, which overall resulted in a reduced aspect-ratio. Fig. 5.34 depicts this general qualitative trend of the changing aspect-ratio as a function of focusing depth. The blue, green and red shaded regions indicate the projected aspect-ratio for approximate focusing condition.
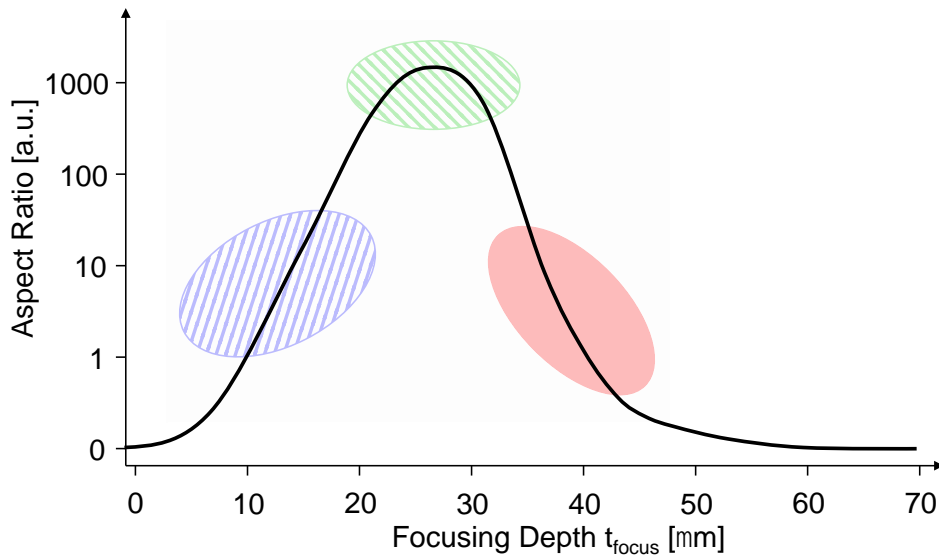
Fig. 5.34 - Graph of the general trend of the aspect-ratio of nano-fibers on Fused Silica

It is interesting to notice that when the incident pulse energy was decreased the aspect-ratio trend shifted towards shallower focusing depth, as shown in Fig. 5.35. In addition, the maximum achievable aspect-ratio also reduced accordingly. On the contrary, an increase of the incident pulse energy did not yield a similar shift of the trend curve towards deeper focusing depth but rather led to a bursting bubble on the surface.
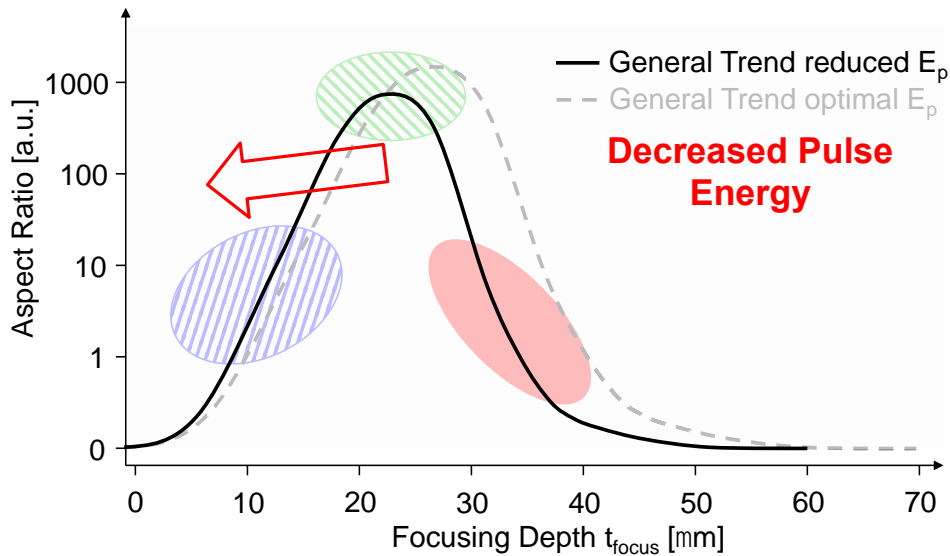
Fig. 5.35 - Graph of general trend of the nano-fiber aspect-ratio for decrease pulse energies

When the irradiated base material was changed, i.e. from Fused Silica to aluminumsilicate glass, the maximum achievable aspect-ratio decreased. This is shown in Fig. 5.36. It should be pointed out that Fused Silica also exhibits the highest melting temperature of the investigated materials that developed nano-fibers. Therefore, it can be assumed that the ejection temperature of the fiber seed is highest in this material, causing longer fibers than for materials with lower melting temperature.
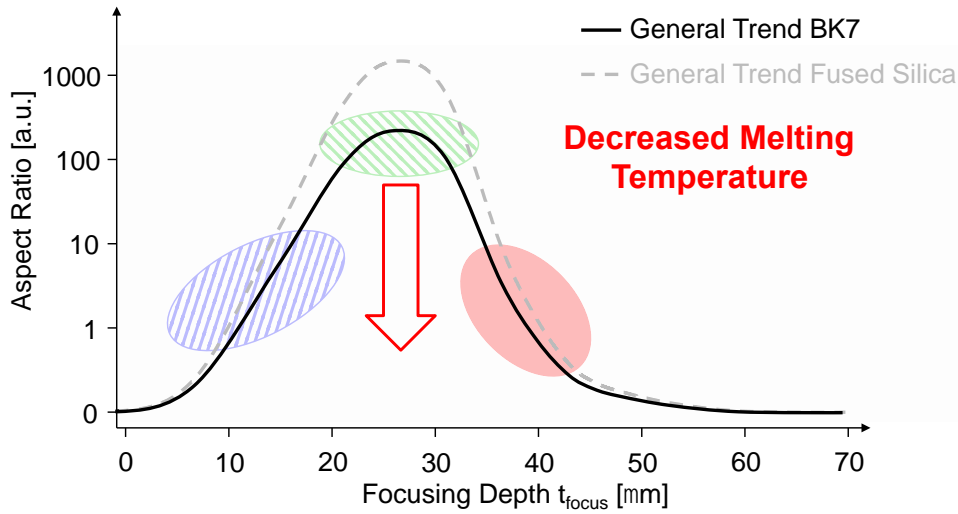
Fig. 5.36 - Graph of general trend of nano-fiber aspect-ratio for changing materials

5.4 Proposed Model for the Generation of Nano-Fibers

Using the results from the conducted experiments, a basic qualitative model is proposed and detailed herein.

Due to the high repetition rate of the incident pulse train, a thermally excited volume is generated around the absorption region. This volume expands quickly based on the HA model introduced in Chapter 2.2.7. The temperature within the volume can also quickly rise above the melting temperature of the base material, leading essentially to an expanding molten front, here defined as the fusion front. A principle scheme of this process is depicted in Fig. 5.37.
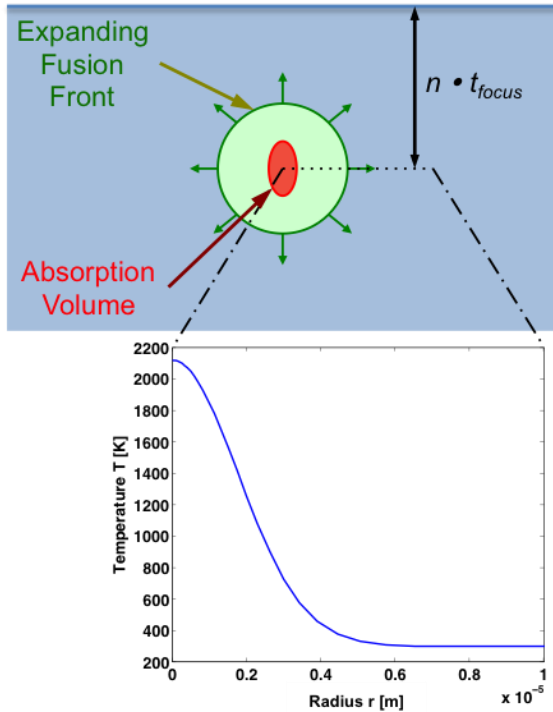
Fig. 5.37 - Scheme of the absorption volume of the incident pulse train and its surrounding molten volume

If the incident pulse train is long enough, the electron density in the absorption volume reaches critical density and the incident energy is mainly only heating the excited electron. This is characterized by a change in the absorption scheme from initially non-linear to quasi-linear absorption; compare Fig. 5.8 through Fig. 5.11. Moreover, the independence of the emission spectrum from the heated focal volume with respect to the pulse repetition rate also supports the fact, that the temperature of the electron system in the absorption volume becomes saturated. At this point the excited electron plasma grows much faster towards the incident beam, which also causes the fusion front to grow faster towards the incident surface. This stage of the thermal expansion process is shown in Fig. 5.38(a).

Once the expansion volume extended all the way to the incident surface, a thin solid skin layer remains between the ambient atmosphere and the molten dielectric material, depicted in Fig. 5.38(b).
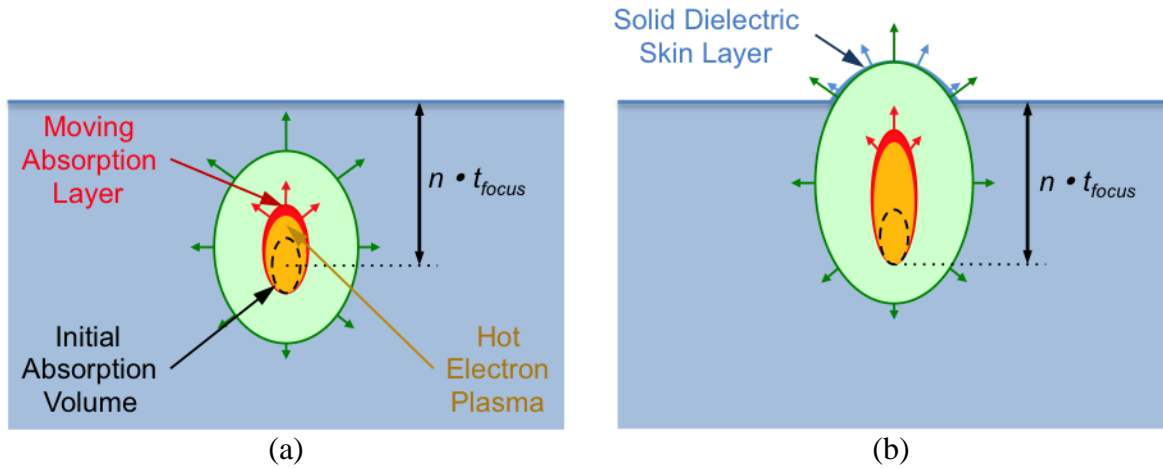
Fig. 5.38 - Scheme of the expansion process of the molten volume; (a) change in absorption regime and (b) expansion volume hits sample surface

Depending on the initial focusing depth, three possible cases have to be considered as depicted in Fig. 5.30. If the focusing depth is set close to the incident surface a material cap will be removed prior to the generation of any nano-fibers. In the second and optimal case, when the focusing depth is set around $f_{focus} \approx 30 \ \mu m$, long nano-fibers will form on top of the thin skin layer, shown in Fig. 5.39(a). Quintero suggested that nano-spheres are detaching from the molten surface, which then form nano-fibers due to the extraordinary cooling rate of these structures in atmosphere. However, it is unclear at this point if the nano-fiber-formation can cause by such detaching nano-spheres or by capillary ejection of molten material. If the focus is set deeper inside the bulk sample, the third case develops as a bubble forms on the sample surface without the formation of nano-fibers, illustrated in Fig. 5.39(b).

It should be pointed out that the gaseous phase very likely develops during the material ejection or bubble formation stage. Due to the fast material ejection or expansion, the pressure relaxed rapidly, which cause the phase change of the heated material; see Chapter 2.2.7. Therefore, no gaseous material states existed during the nano-fiber formation process, which makes it difficult to apply the super-sonic jet model developed by Quintero [174], [184] to the here investigated generation process.
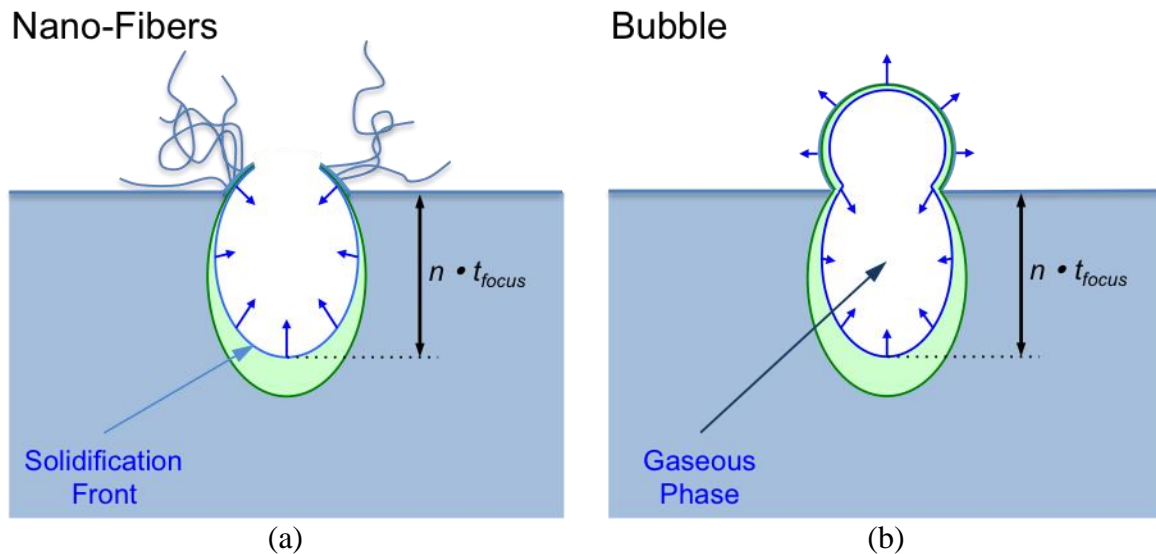
Fig. 5.39 - Schemes of the formation of (a) nano-fibers and (b) intact bubble on the sample surface

The speed of the fusion front is believed to play a critical role in the nano-fiber generation process. Since the expansion speed of the fusion front reduces the further it extends from the initial focal volume, it is thought that an optimal expansion speed is necessary to hit the sample surface to generate high aspect ratio nano-fibers. If the focusing depth was set too shallow, the expansion speed at the surface will be too high and a material cap will be blown off the surface. If the focus

127

was chosen to deep, the expansion speed at the surface will be too low and therefore an intact bubble is formed. More experiments are necessary to verify this hypothesis.

5.5   Conclusion Nano-Fiber Generation

In conclusion, it was found that high repetition rate lasers are required for nano-fiber formation from the bulk materials tested. Only such systems enable the HA-processing regime, which enabled high temperatures in the processing volume. Thus, nano-fibers could be observed when the processing parameters caused the irradiated materials to exceed their melting temperature. However, the repetition rate independent emission spectra collected from the absorption volume suggest that the temperature will saturate eventually.

The here presented data also indicated that there is a change in the absorption regime from a non-linear to quasi-linear absorption process when HA-processing conditions were present. This quasi-linear absorption process is believed to be mainly electron heating on the outer top layer of the laser-induced electron plasma. This electron heating process also caused an asymmetric growth of the molten volume faster towards the incident beam than in orthogonal direction, as also reporter by other researchers.

6   RIPPLES – LASER-INDUCED PERIODIC SURFACE STRUCTURES

6.1   Introduction

The first experiments documenting the generation of laser induced periodical surface structures (LIPSS), also known as surface ripples, were conducted shortly after the invention of the laser, when Birnbaum [52] reported in 1965 periodic structures formed on semiconductor surfaces irradiated with pulsed ruby laser (694.3 nm) radiation at intensities above the ablation threshold. Following in the 80's many deliberate studies of what now is known as low spatial frequency LIPSS (LSFL) were performed on semiconductors [185]-[187], metals [188]-[190], and dielectrics [191], utilizing mainly Q-switched laser sources with pulses as short as picosecond durations. The ripple structures generated showed a periodicity of approximately the laser wavelength with a groove direction perpendicular to the incident beam polarization, thus suggesting an interference effect taking place and leading to a modulation of the ablation pattern.

A widely accepted theoretical model introduced by Sipe *et al.* [192] correlated the ripple generation to the interaction between the E-field of the incident beam with microscopic surface roughness in the "selvedge region" (between $z = 0$ and $l/\lambda << 1$, z is the direction normal to the material surface, λ is the radiation wavelength) of the material. This interaction leads to inhomogeneous energy absorption in the top-most layer of the material. The model computes a material response function, a so-called efficacy factor η, depending solely on the incident beam parameters (polarization direction, incident angle Θ) and the material properties (dielectric function ε, surface roughness). According to Sipe, the efficacy factor describes the response function with which surface roughness leads to inhomogeneous absorption in the selvedge region. This function contains sharp spikes at predicted ripple periods and is defined as [193]

$$\eta_{x,y}(k, k_i) = 2\pi(|v(k_+) + v^*(k_-)|\hat{X} + |v(k_+) + v^*(k_-)|\hat{Y}), \quad (6.1)$$

where the $\hat{X}$- and $\hat{Y}$-terms represent orthogonal directions of the ripple groove direction and v is a complex function proportional to the material absorption. k and k_i are the wave-vector and its component parallel to the surface, respectively. The polarization of the incident beam can then be expressed in terms of k_x and k_y. Bonse *et al.* [193] pointed out, supported by the results of the computation of the efficacy factor in x- and y-direction, there should exist not only a ripple pattern with groove direction perpendicular to the incident E-field but also parallel to it. An experimental proof directly linking Sipe's theory to a ripple pattern parallel to the incident E-field direction is still outstanding.

With the advent of femtosecond-laser sources suitable for material processing new types of ripple structures have been reported. Several researchers reported the observation of LIPSS with a period considerably smaller then the structures generated with longer pulses [104]-[106], [159]. These high spatial frequency LIPSS (HSFL) did not appear to be well explained by *Sipe's* original model. Couillard *et al.* [194] argued that HSFL formation would be covered by Sipe's theory if account was taken of the material changes occurring from the irradiation itself as well as the convergence angle of the laser beam on the sample. *Jia et al.* [195] introduced an alternative model suggesting that the formation of the HSFL results from second harmonic generation (SHG) at the interface of the sample. This SHG signal then interferes with the initially incident fundamental wave in the material at a much shorter periodicity leading to a ripple spacing of $\frac{\lambda}{2n}$. Reif *et al.* [196] as well as Andreev *et al.* [197] developed a model that described the generation of HSFL by the generation of metallic colloids due to the incident laser field. These colloids then

allow for the excitation of Plasmon waves, which can then couple with those from adjacent colloids to form ripples.

In addition there have been several reports on the generation of nano-gratings within the bulk of dielectrics exhibiting seemingly similar properties to the high spatial frequency structures observed on the surface of the sample [198]-[200]. If indeed the same physical mechanisms were the cause for both these effects without further considerations, it would seem to exclude a process relying on a surface wave interference as it is the case in *Sipe's* theory.

More seldom are reports of structures with a groove orientation parallel to the polarization of the incident laser beam, denoted as parallel LIPSS (P-LIPSS). Haugen *et al.* [201] investigated the generation of this type of LIPSS on c:Si surfaces using fs-laser pulses at wavelength of $1300\ nm$ and $2100\ nm$. More recently, Tomita *et al.* [202] reported on ripple effects originating from $100\ kHz$ femtosecond irradiation of smooth ($R_a \sim 0.2\ nm$) and roughen ($R_a \sim 6\ nm$) silicon. Both research groups observed the previously known LSFL ripples when irradiating either material, however they also discovered ripple structures parallel to the incident E-field when irradiating with multiple pulses at fluence levels well below the ablation threshold. The period of these ripple structures was approximately equal to the incident wavelength. Interestingly, these P-LIPSSs were in Tomita's case solely developing on the roughened Si-surface.

A clear understanding of the fluence-dependence of the development of all these various surface ripple structures produced with femtosecond laser pulses is still not apparent even though several studies have been made in the last decade. The development of laser sources in the near- and mid-IR spectrum has opened and will further open new opportunities to study these light-

131

mater interaction schemes at longer wavelengths, particularly for semiconductor materials, which also represent the largest group of studied materials ripples appear on.

The applications of this microscopic, semi-deterministic material surface texturing are widespread, ranging from the fabrication of biomedical substrates for directed cell growth [203], the enhancement of sensor sensitivity [204] or the efficiency improvement of photovoltaic devices [205].

Two important semiconductor materials are silicon (Si) and gallium arsenide (GaAs). Most studies of LIPSS in these materials so far have used laser radiation with shorter wavelengths at a spectral range in which these materials were not transmissive. Both these materials have high transmission at wavelength longer than $1.1 \ \mu m$. The presented investigation was aimed to shed some insight on the fluence-dependence of the development of surface ripples and examine the early stages of ripple formation in these two semiconductor materials, particularly the formation of parallel-LSFL at low intensities.

6.2 Experimental investigation of ripples

The experiments described here focus on the generation and characterization of surface ripple structures using ultrashort-pulsed laser radiation at a wavelength of $2 \ \mu m$. In addition, where appropriate, comparison to irradiation with ultrashort laser pulse at $\lambda = 400 \ nm$ and $\lambda = 800 \ nm$ is included.

6.2.1 Laser irradiation setup

The IR ultrashort pulses were generated using the Coherent Opera OPA, pumped by the Spectra-Physics Spitfire MOPA laser system as previously described in Chapter 3.1.2.

The output radiation from the OPA was passed through a halfwave-plate (HWP) to adjust the polarization orientation. The laser radiation was roughly attenuated by first passing the beam through ND-filters, followed by a partially reflective mirror wheel for fine-tuning capabilities. Rotation of the mirror wheel allowed varying the incident pulse energy on the sample. After passing the attenuation stage the beam was coupled into the standard processing station, as described in Chapter 4.2. The focusing optics was a 10X microscope objective with a NA of 0.25. The irradiation setup is shown schematically in Fig. 4.3. The mirrors used to deflect the laser beam were dielectric mirrors with 99.6% reflectivity for 2 μm radiation, but highly transmissive for visible radiation. However, the focusing objective was comprised of an oxide glass lens system coated with MgF_2 for visible light in the spectral range of $400 - 700\ nm$. Therefore the 2 μm radiation losses through the irradiation tower were measured to be 30-40%, mainly originating from the focusing objective. A precise measurement of the focus spot shape and size was made using a knife-edge scan technique. The $2\ \mu m$ beam shape was recorded throughout the focal region with a Spiricon PyroCAM IR beam camera. A full description of this characterization is provided in an earlier publication [206]. The beam waist in the focus was determined to be approximately $w_0 = 13\ \mu m$.

6.2.2 Irradiation Conditions

The experimental studies described here were made on two materials, intrinsic crystalline (c:) GaAs and intrinsic crystalline (c:) Si. In the latter case the inherent oxide layer that forms naturally on silicon surfaces affected the laser-matter interaction process.

Vital to the understanding of the fluence-dependent evolution of LIPSS is the knowledge of the intensity threshold for surface modification of the samples tested. To predict the modification

threshold of materials used, a procedure adopted by *Liu* [95] was followed, as described in Chapter 2.2.5.

Many of the irradiation conditions were made in the 'writing mode' in which successive pulses partially overlapped on the surface of the material to create a line of irradiated area. Therefore controlling the translation speed of the sample allowed the variation of the number of pulses irradiating the nominal spot diameter and hence the total accumulated fluence or dose of such area. In addition the incident polarization and pulse energy were varied individually while keeping the other parameters constant. For each of the experiments performed, a serpentine-pattern was scanned on a pristine surface of the sample to form an extended irradiated area.

Following the irradiation process the samples were cleaned using an acetone solution in an ultra-sonic bath. They were then characterized with optical microscopy and SEM. The topologic profile of the irradiated area on the sample was inspected using a white-light interferometer (ZYGO NewView 6000). An AFM was used when increased lateral resolution was needed.

6.3 Different Ripple Regimes in Semiconductors

The different types of ripple structures and their definitions are well illustrated by the data observed on GaAs, shown in Fig. 6.1. In this figure, the translation speed was continuously decreased from $0.5\ mm/s$ (left) to $0\ mm/s$ (right). The pulse energy was kept constant at $E_p \approx 100\ nJ$, thus increasing the accumulated surface fluence accordingly. Provided the measured spot radius of $w_0 = 13\ \mu m$, a single spot area on the far left sustained an accumulation of 52 pulses, corresponding to an accumulated fluence of $F_{accum} \approx 1\ J/cm^2$ whereas the same area on the far right was irradiated with up to 350 pulses (accumulated fluence $F_{accum} \approx 6.6\ J/cm^2$). It clearly

shows the dominant ripple structure changing from P-LIPSS on the left, LSFL in the center region

to HSFL on the far right of Fig. 6.1.

The Sipe theory [192] predicts a ripple periodicity of approximately $\Lambda = \lambda$ with a groove

orientation perpendicular to the incident laser beam polarization; the image depicts these

structures marked as LSFL in a region with moderate fluences of $1.35 - 2$ J/cm^2. On the left edge

of Fig. 6.1 are regions irradiated with fluences between 1.0 and 1.35 J/cm^2 in which a 90°-rotated

ripple structure is observed. The periodicity of this structure is smaller than that occurring for

LSFL, however not as small as for HSFL, which occurred at regions to the far right edge of Fig.

6.1 with fluence levels above $2 \, J/cm^2$. One can also recognize the existence of a small transition

region between the different ripple structures.
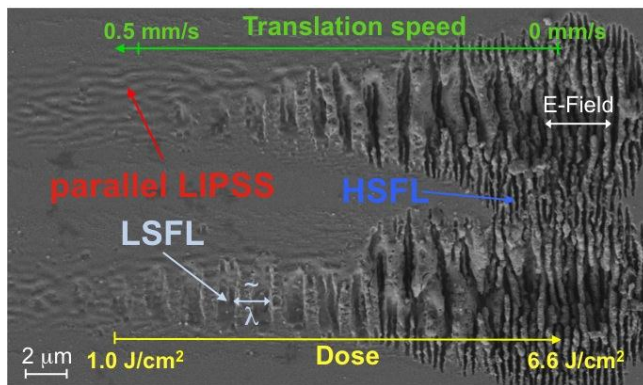
Fig. 6.1 - Irradiation track on the surface of intrinsic c:GaAs after processing with ultrashort

laser radiation; the avg. fluence was increasing toward the right of the track resulting in a

change of the LIPSS pattern, clearly recognizable are three different types of LIPSS: LSFL,

HSFL and P-LIPSS

6.3.1   P-LIPSS ripple regime at low intensities

At low fluences shallow ripples with their groove direction parallel to the incident E-field

vector were formed. Examples of the feature are shown for c:GaAs and c:Si in Fig. 6.2(a) and Fig.

6.2(b), respectively. This type of ripple will be referred to as parallel-LIPSS (P-LIPSS). The period of the feature was measured to be approximately $\Lambda_{P-LIPSS} = 450\ nm$ for all types of semiconductors investigated.

In the case of c:GaAs the translation speed of the sample was set to $v_{lateral} = 0.5\ mms^{-1}$, producing an average pulse-deposition rate of 52 pulses per spot diameter. The pulse energies on target for the samples shown were (a) $E_p = 136\ nJ$ and (b) $E_p = 113\ nJ$. It should be noted that these values were well below the corresponding single shot modification threshold fluence ($F_{incident} \approx 23\ mJ/cm^2$). Moreover, the ripple wave-vector, which is defined as the vector normal to the ripple groove direction, rotates with the rotation of the incident polarization, staying parallel to the incident E-field vector.

(a) (b)
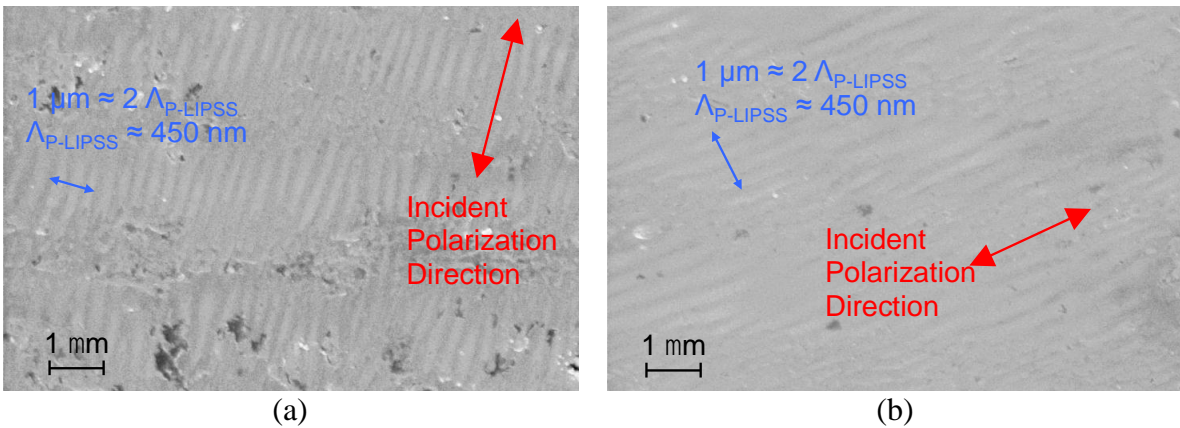
Fig. 6.2 - P-LIPSS on intrinsic c:GaAs with a period of approximately $\Lambda_{P-LIPSS} \approx 450\ nm$ occured for low accumulated fluences on the target at an integration of 52 pulses per spot area, the pulse energies were (a) $E_p = 136\ nJ$ and (b) $E_p = 113\ nJ$

The depth profile of the grooves and bumps was measured on c:GaAs using an AFM and is shown in Fig. 6.3. The peak-to-valley value was approximately $\Delta t_{P-LIPSS} = 10\ nm$. The ripple period was confirmed with approximately $\Lambda \approx 400\ nm$.
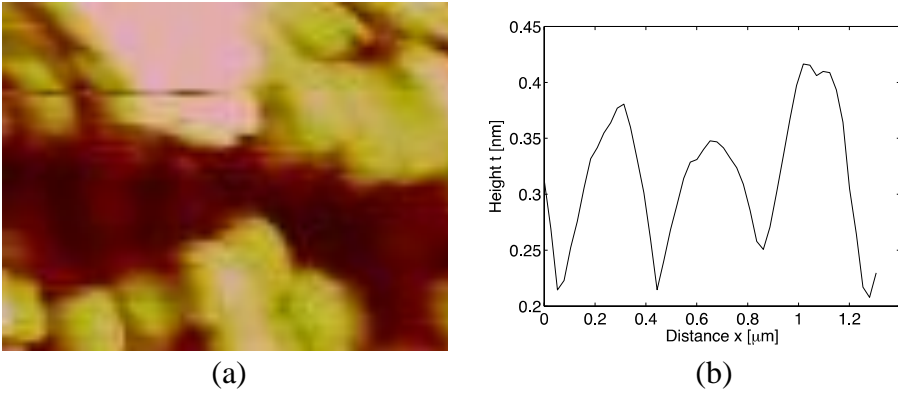
Fig. 6.3 – Measured (a) AFM topology and (b) cross-section profile an P-LIPSS structure on c:GaAs surface

For the case of c:Si, the translation speed of the sample was $v_{lateral} = 0.25 \, mms^{-1}$, therefore the number of pulses accumulated per spot area was 104, which is significantly higher than for c:GaAs. The increased number of shots necessary is attributed to the protective oxide layer on top of c:Si. However, the pulse energies on target for the samples shown in Fig. 6.4 were similar to those used for c:GaAs with $E_p = 129 \, nJ$. As with GaAs, these values translate to single shot fluence values one order of magnitude lower than the measured modification threshold fluence.
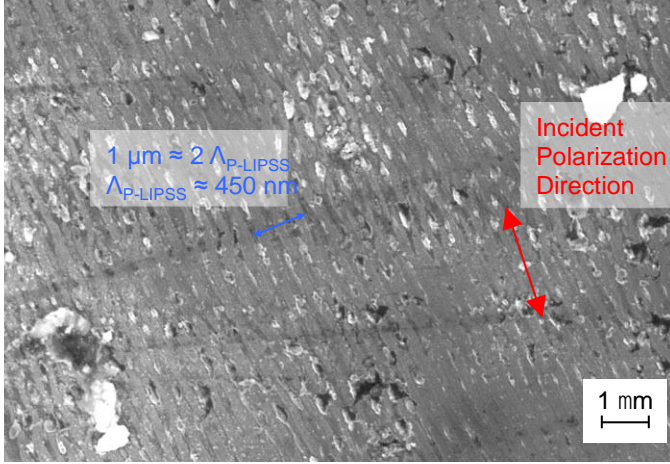
Fig. 6.4 -P-LIPSS on intrinsic c:Si with a period of approximately $\Lambda_{P-LIPSS} \approx 450\ nm$

occured for low accumulated fluences on the target at an integration of 104 pulses per spot

area, the pulse energy was $E_p = 129\ nJ$

Previous studies of ordinary LSFL ripples also noted that the ripples grow continuously over neighboring irradiation tracks to fill the entire irradiated area coherently. This property could not be reproduced here for P-LIPSS. An explanation for such a result might be drawn from [201] where a LIPSS pattern similar to that shown here could only be observed in the central region of the laser spot corresponding to the highest intensity region of the Gaussian intensity distribution. Observations based on Fig. 6.2(b) revealed the width of the ripple structure being less than $D_{P-LIPSS} \approx 1\ \mu m$ compared to an incident Gaussian beam diameter of $2w_0 = 26\ \mu m$. Therefore the range of favorable conditions required for the generation of P-LIPSS might be outside the overlapping region of neighboring tracks.

6.3.1.1 Polarization dependence of P-LIPSS

As shown above, the dependence of the ripple orientation on the polarization was similar to that previously reported for both LSFL and HSFL with the difference to be parallel. A rotation of

the incident E-field vector causes the ripple structure to rotate as well following the E-field and aligning parallel to the polarization, as depicted in Fig. 6.2. This behavior underlines the connection between incident E-field and ripple generation mechanism.

6.3.2 Theory of P-LIPSS

The theoretical model of LSF ripple development is based on Sipe's theory [192] and was computed using calculation proposed by Bonse [193]. However, the challenge of the presented work was to predict properties of ripples parallel to the incident E-field orientation, which were not included in Bonse's work.

Sipe's theory describes the generation of dipole-sources, defined as [192]

$$\vec{Q}(\vec{\rho}) = b(\vec{k})l\overleftrightarrow{\gamma}\vec{E}_i e^{i\vec{k}_+ \cdot \vec{\rho}} + b^*(\vec{k})l\overleftrightarrow{\gamma}\vec{E}_i e^{i\vec{k}_- \cdot \vec{\rho}},$$ (6.2)

in the very narrow "selvedge-region" due to the incident field $\vec{E}_i$ and the susceptibility of the material $\overleftrightarrow{\gamma}$. The factor $b(\vec{k})$ describes the topologic profile of the surface of this region. As one can easily imagine, any surface roughness will cause the deflection of the incident E-field, mainly originating from Fresnel transmission coefficients, causing minuscular perturbations resulting in a modified representation of the wave-vector $\vec{k}_\pm = \vec{k}_i + \vec{k}$. In addition, the field from the induced dipole emits circularly in the x-y-plane giving rise to an E-field component perpendicular to the original incident E-field. Thus the present E-field in the underlying bulk region is a superposition of the incident refracted field $\vec{E}^{(0)}$ and the perturbed field emitted by the dipole $\vec{E}^{(1)}$, given as [193]

$$\vec{E}(\vec{r}) = \vec{E}^{(0)}(\vec{r}) + \vec{E}^{(1)}(\vec{r}),$$ (6.3)

where $\vec{r}$ indicates the radial nature of the total field function and thus having contributions in both the s- and p-polarization directions.

The absorption $A(\vec{r})$ in the underlying bulk region will be proportional to $|\vec{E}(\vec{r})|^2$. It can be shown that the interfering parts of $\vec{E}^{(0)}$ and $\vec{E}^{(1)}$ lead to a modulated absorption term [192]

$$A(\vec{r}) \cong 2Re\{\vec{E}^{(0)^*}(\vec{r}) \cdot \vec{E}^{(1)}(\vec{r})\} \qquad (6.4)$$

and becomes [192]

$$A(\vec{\rho}) = \frac{2}{\lambda} lRe\left\{ b(\vec{k})[v(\vec{k}_+) + v^*(\vec{k}_-)] \times e^{i\vec{k}_+ \cdot \vec{\rho}}\right\}, \qquad (6.5)$$

with $l = z, \quad \frac{l}{\lambda} \ll 1,$

which is also proportional to [193]

$$A(\vec{\rho}) \propto [\eta_x(k_x, k_i) + \eta_y(k_y, k_i)]|b(\vec{k})|. \qquad (6.6)$$

This enables the computation of the efficacy factor for the bulk region of the material. More practical equation for $v(\vec{k}_+)$ and $v(\vec{k}_-)$ given by Bonse [193] were used to compute an efficacy factor model. Here it was assumed that the incident polarization is parallel with the x-direction of the x,y-plane on the surface and the beam is incident normal to the surface ($\theta = 0$). In that case the function for $v(\vec{k}_+)$ is given as [193]

$$v(\vec{k}_\pm, s - pol) = [h_{ss}(k_\pm)\left(\frac{k_y}{k_\pm}\right)^2 \hat{Y} + \qquad (6.7)$$

$$h_{kk}(k_\pm)\left(\frac{k_x}{k_\pm}\right)^2 \hat{X}]\gamma_t|t_s(\vec{k}_i)|^2,$$

with $k_\pm = \sqrt{k_x^2 + k_y^2}.$

The values for the necessary dielectric functions $\varepsilon = (n + i\kappa)^2$ for crystalline and amorphous GaAs and Si, respectively, were taken from [207]. They are documented in Table 6-1. The incident wavelength was varied between 800 nm and 2 μm, the shape factors s and f were kept at 0.4 and

0.1, respectively, as suggested by Bonse for spherically shaped islands. The results of the efficacy factor computations for GaAs and Si are shown in Fig. 6.5.

Table 6-1 - Values for dielectric function ε for crystalline (c:) and amorphous (a:) GaAs and Si

	n	
c:GaAs @ 800 nm	3.68356	0.08905
c:GaAs @ 2 μm	3.34108	0
a:GaAs @ 2 μm	3.8^6	0
c:Si @ 800 nm	3.69246	0.0297
c:Si @ 2 μm	3.45268	0
a:Si @ 2 μm	3.44224	0

There is a small offset between the ripple period measured in the experimental results of P-LIPSS shown in Fig. 6.2 and Fig. 6.4 and the predicted period due to the calculations due to Sipe's theory. The peak for c:GaAs (Fig. 6.5(b)) and c:Si(Fig. 6.5(d)) relates to a ripple periodicity of approximately $\Lambda_{P-MODEL} = 500 \, nm$, however the experimentally determined ripple periodicity is approximately $\Lambda_{P-LIPSS} = 450 \, nm$. Nevertheless, such an offset can be caused by the transient material properties during the fs-irradiation, as the shift of the peak of the efficacy factor towards larger values of k_y resulting from amorphous GaAs already depicts (dashed line).

---

[6] Value taken from ref. [194]
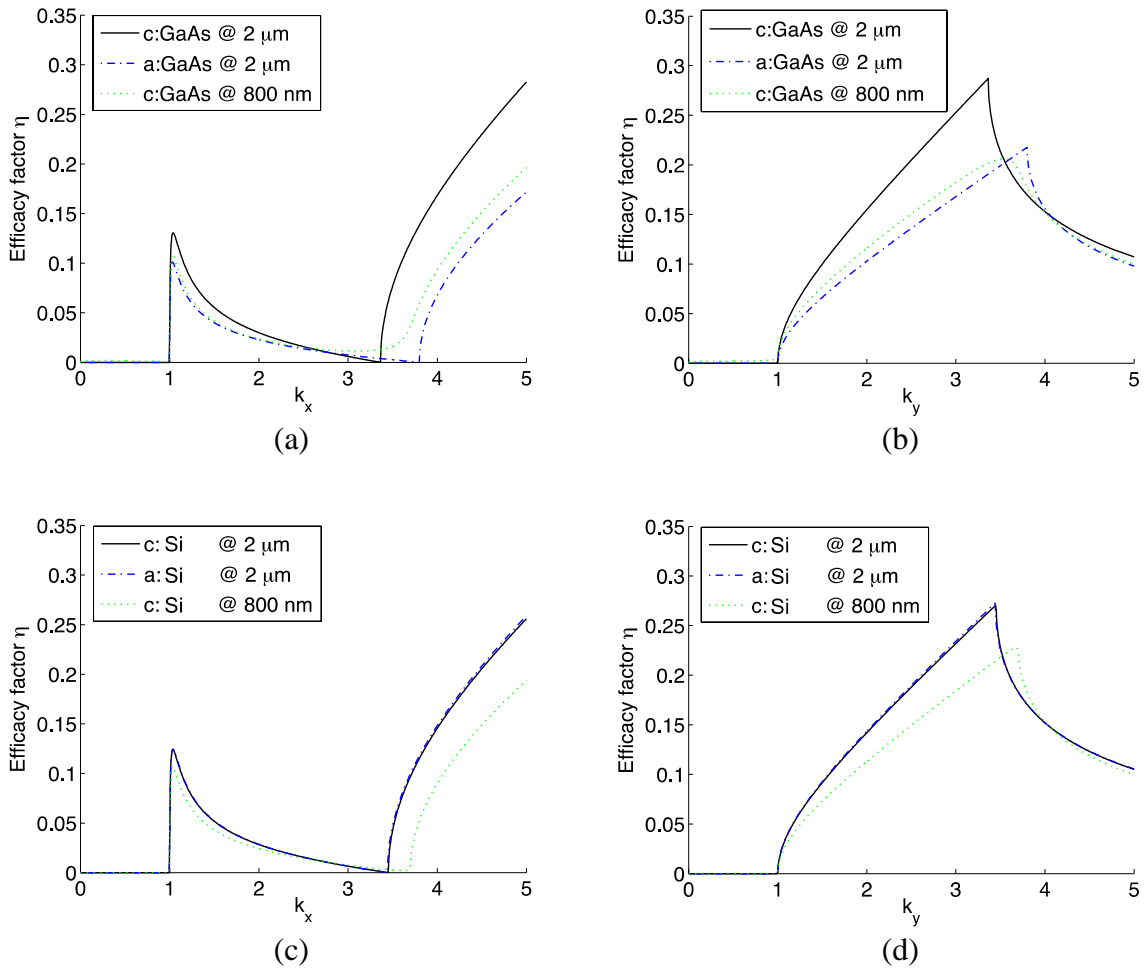
Fig. 6.5 - Efficacy factor of GaAs (top) and Si (bottom) for s-polarized light incident normal to sample surface with groove direction (a)/(c) perpendicular and (b)/(d) parallel to radiation E-field

Unclear from this first-principles theory is why the parallel ripple structure occurs at a lower surface fluence level than the LSFL features. A possible explanation is the existence of a resonant feedback mechanism, which supports different directions of the susceptibility tensor at different incident accumulated fluences.

Even though observation from Fig. 6.1 might suggest the existence of a transition region between P-LIPSS and LSFL with a coexistence of both structures, it was not possible to generate such experimentally. In experiments targeting this specific fluence-window, only one structure or the other developed.

The computational model for c:GaAs and c:Si, as shown in Fig. 6.5(a) and Fig. 6.5(c), respectively, predicted the ripple periodicity of approximately the laser wavelength.
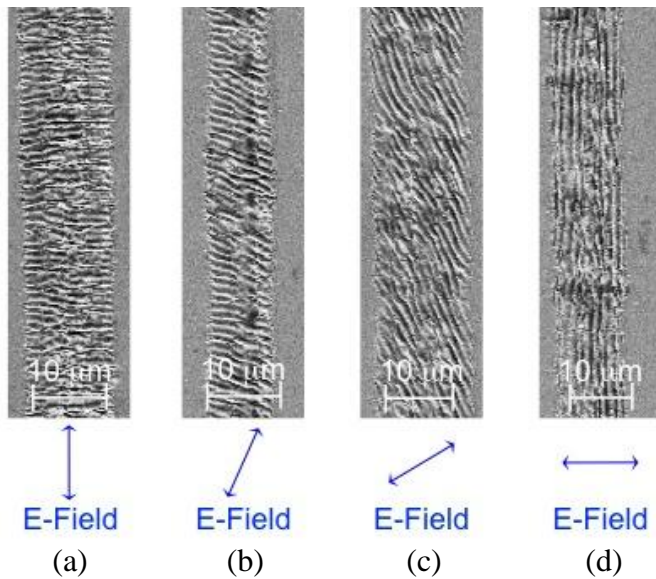
Fig. 6.6 – SEM images of LIPSS (LSFL) at moderate accumulated fluence of $2\,J/cm^2$ ($E_p = 104\,nJ$, $v_{lateral} = 0.25\,mms^{-1}$) on c:GaAs for varying incident E-field directions

It should be noted that the images in Fig. 6.6 depict multiple neighboring laser tracks with an overlap of each other of ~ 30%. The ripple structure developed here is spatial coherent not only within a single track, as shown before in the case of P-LIPSS, but also between neighboring laser tracks. This would allow one to structure large areas with spatially coherent LSFL structures for particular applications.

Furthermore, the generation of LSFL was also investigated using 400 nm and 800 nm laser wavelength [208]. Both materials exhibited the structure formation in a window of significant lower accumulated fluences around $0.3 \, J/cm^2$.

6.3.3 High Spatial Frequency LIPSS

With increasing accumulated fluences above $2 \, J/cm^2$, HSFL started to develop and eventually dominated the structure. In this regime the ripples developed a periodicity of approximately $\Lambda_{HSFL} = 400 \, nm$ at $2 \, \mu m$ incident laser wavelength, shown in Fig. 6.7, with an orientation perpendicular to the incident E-field. Both structures, LSFL and HSFL, were generated at equal pulse energies but varying translation speeds, therefore the determining factor for the generation of either ripple structure was the number of pulses per area. That observation is consistent with reports by Bonse [193] who noticed a development of HSFL when accumulating multiple irradiation events at $800 \, nm$ laser wavelength on InP surfaces.
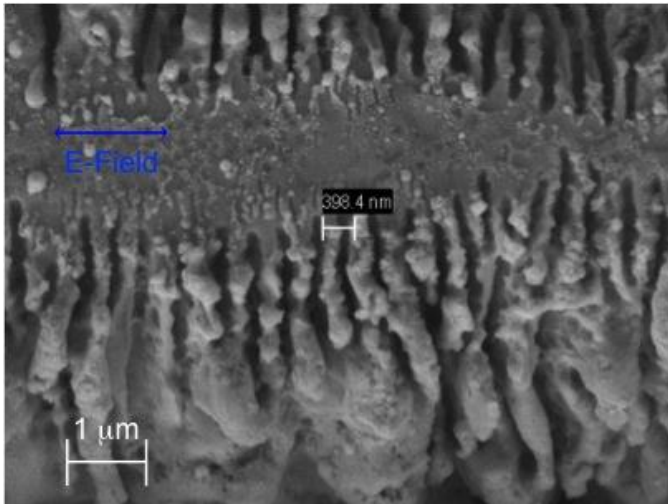
Fig. 6.7 - LIPSS developed at high accumulated fluences of $2.45 \, J/cm^2$ on c:GaAs surfaces

Experiments using $400\ nm$ and $800\ nm$ incident radiation wavelengths did not lead to the development of HSFL, however, no special care was taken for favorable irradiation condition for such ripple generation since it was not matter of research in this thesis. Nevertheless, other research has also shown the generation of HSFL using shorter incident laser wavelength.

6.4   Conclusion Ripple Formation

In summary the generation of a parallel LIPSS with respect to the incident E-field orientation was shown at **$2\ \mu m$** radiation wavelength on c:GaAs and c:Si. The periodicity was predictable on the basis of the Sipe's theory [192]. Moreover, the development of ripple structure has been categorized in three different regimes, which led to P-LIPSS at low accumulated fluences, LSFL at moderate accumulated fluences and HSFL at high accumulated fluences.

When partially overlap of the modified region is granted P-LIPSS exhibits the same general properties of coherence as observed for LSFL.

7 FEMTOSECOND LASER PROCESSING OF SEMICONDUCTORS

Before one discusses the processing of semiconductor materials, some considerations should be paid to the differences in processing environment in such materials compared to other materials. Firstly, semiconductors possess a much larger refractive index compared to dielectrics. Thus, diffraction at the interface between air and the sample itself will be substantial, causing the effective NA of the focusing optic to decrease significantly. Furthermore, the effective speed of light in the bulk of the medium will decrease by the fraction of the refractive index $\frac{1}{n(\omega)}$, causing the pulse to become effectively shorter in space compared to dielectrics.

The lattice structure of a semiconductor is in general crystalline, as opposed to the amorphous lattice structure of common dielectric materials such as Fused Silica. Nevertheless, laser-induced modification has been observed in crystalline dielectrics as well such as sapphire or Fused Quartz. The major difference to be taken into account between crystalline and amorphous materials is the thermal conductivity and possible birefringence of such materials.

In general, semiconductors develop an oxide layer on the surface when exposed to oxygen-rich ambient air. Therefore, a two-layer system has to be considered or the samples have to be buffer-etched before used in an experiment. The natural oxidation rate of c:GaAs and c:Si was investigate elsewhere [209].

In this study c:Si and crystalline c:GaAs were the semiconductor materials primarily studied. For each of the two, various dopant types and concentration were investigated. An overview of the investigated specimens and their properties is given in Table 7-1.

Table 7-1 – Overview of the investigated semiconductor specimens

Sample Materials	Lattice Structure	Fabrication Method	Free Absorber Concentration [cm^{-3}]	Band gap Energy [eV]
intrinsic c:GaAs	zinc blende	Cz[7]	1.00E+18	1.476
n-doped c:GaAs	zinc blende	Cz	1.00E+21	1.476
p-doped c:GaAs	zinc blende	Cz	1.00E+23	1.476
intrinsic c:Si	diamond cubic	floatzone	1.50E+11	1.181
intrinsic c:Si	diamond cubic	Cz	2.00E+14	1.181
n-doped c:Si	diamond cubic	Cz	1.20E+12	1.181
n-doped c:Si	diamond cubic	Cz	1.00E+15	1.181
n-doped c:Si	diamond cubic	Cz	5.00E+18	1.181
p-doped c:Si	diamond cubic	Cz	1.00E+13	1.181
p-doped c:Si	diamond cubic	Cz	1.00E+16	1.181
p-doped c:Si	diamond cubic	Cz	1.00E+19	1.181

The general transmission spectra of c:GaAs and c:Si are shown in Fig. 7.1. It is apparent, that there is no significant absorption line in the investigated IR-region between 1.1 μm and 2.5 μm.

---

[7] Cz: Czochralski crystal growth
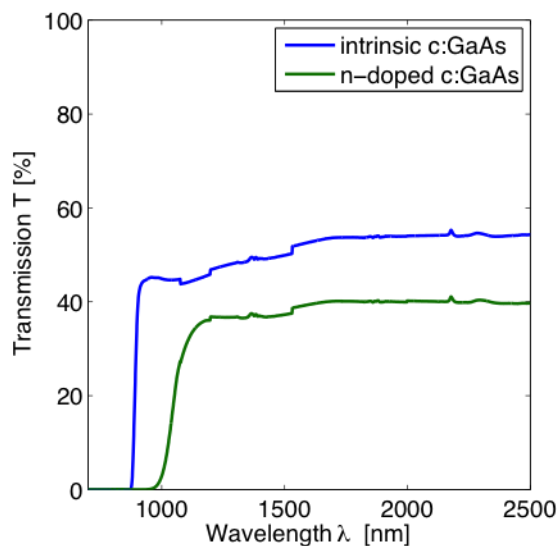
Fig. 7.1 - Graph of general transmission spectrum of c:GaAs and c:Si for NIR/mid-IR wavelength

7.1   Ablation Threshold Measurements

Although the modification threshold for both transparent dielectrics [2], [77], [80], [158], [160], [210]-[212] and semiconductors [159], [194], [213]-[215] due to incident ultrashort-pulsed laser radiation has been previously characterized, the influence of the dopant concentration has yet to be studied. Moreover, the dependencies of the photon-energy of the incident radiation and the band gap energy of the irradiated matter are not yet investigated.

7.1.1   Experimental Approach

To investigate these dependencies, various samples were irradiated using the setup described in Section 4.2, providing the focusing objective, online imaging and sample illumination capabilities, and the computer-controlled 3D motion system. The low repetition rate Spectra Physics Spitfire in combination with the OPA, detailed in Section 3.1.2, was used as the radiation source for these experiments since single pulse irradiation was required for the threshold

measurement [95]. Three different excitation wavelengths were used: $800\ nm$, $1.3\ \mu m$, and $2.4\ \mu m$. The frequency spectrum at $800\ nm$ is shown in Section 3.1.1, the spectra at $1.3\ \mu m$ and $2.4\ \mu m$ wavelengths are shown in Fig. 7.2.
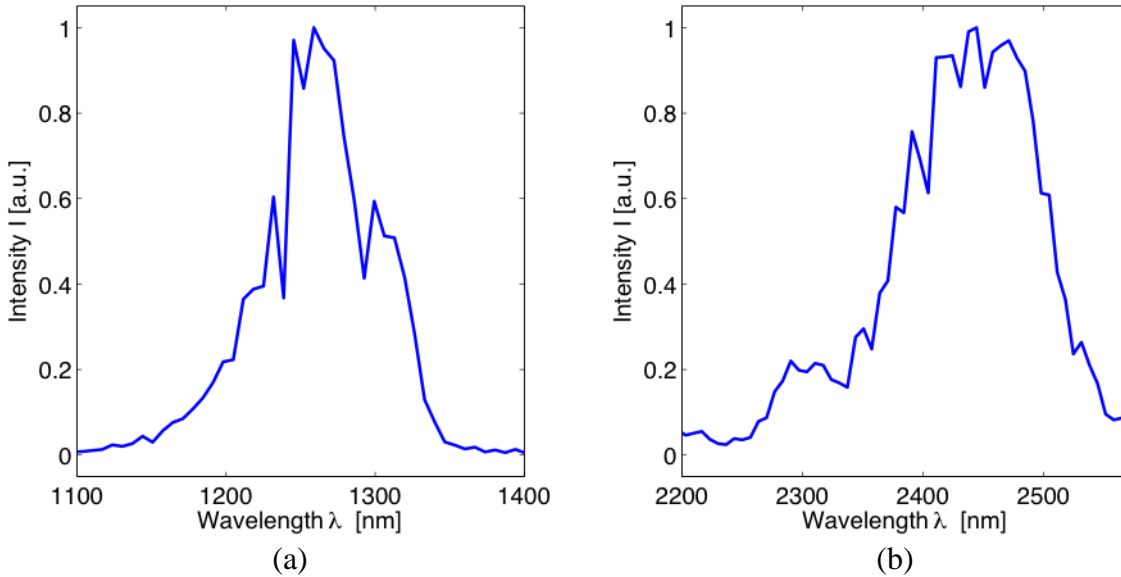
Fig. 7.2 - Graphs of measured spectral emission from OPA at wavelengths of (a) $1.3\ \mu m$ and (b) $2.4\ \mu m$

Before the samples were irradiated, the oxide layer was removed by buffer-etching each sample in 5% hydrofluoric acid solution for 1 min [216]. The samples were then irradiated with single pulses at varying pulse energies and laser wavelengths. Examples of microscope images of the threshold maps produced with laser wavelengths at $800\ nm$, $1.3\ \mu m$, and $2.4\ \mu m$ on intrinsic c:Si are depicted in Fig. 7.3. As the images indicate, several irradiation sites were produced at each pulse energy for averaging. The actual area of the modified material (inset Fig. 7.3) was measured for each irradiation site at the maximum magnification of 100X DIC of the used Olympus BX-52 optical microscope.
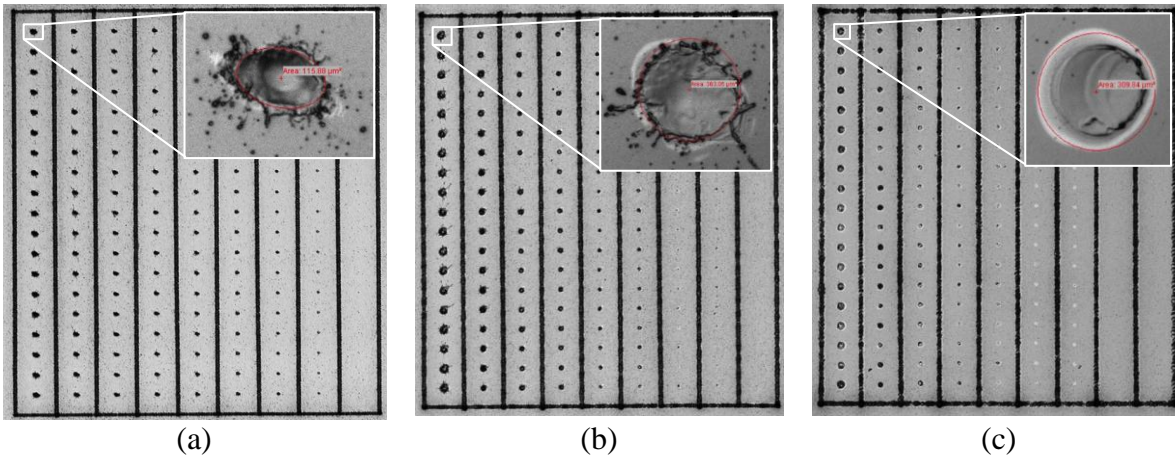
Fig. 7.3 – Microscope images of threshold maps on intrinsic c:Si using wavelengths of (a) 800 nm, (b) 1300 nm, and (c) 2400 nm, insets show measured modified area of a single irradiation site

7.1.2   Threshold Measurement

Most published modification thresholds for semiconductors are available for ultrashort-pulsed laser wavelength at around 800 nm [159], [213]-[215]. Therefore the modification threshold at this wavelength region was investigated first. The squared-diameter function yielding the threshold fluence for a wavelength of 800 nm on c:GaAs is shown in Fig. 7.4(a). Fig. 7.4(b) depicts the threshold fluences as a function of dopant concentration on c:Si for this wavelength.
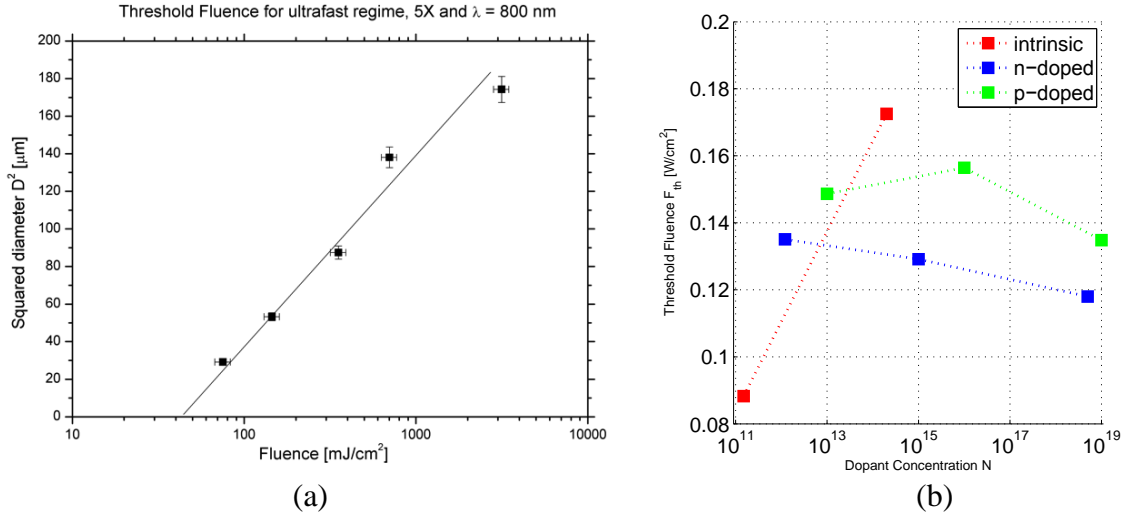
Fig. 7.4 – Graphs of (a) squared diameter yielding modification threshold on intrinsic c:GaAs, and (b) threshold fluences as function of dopant concentration on c:Si at a incident wavelength of $800 \, nm$

For c:GaAs an extrapolated threshold fluence of approximately $F_{th}(c:GaAs, \lambda = 800 \, nm) \approx 45 \frac{mJ}{cm^2}$ was found. This value is three-times lower than expected from literature data [214]. The modification threshold fluences found for Silicon around $F_{th}(c:Si, \lambda = 800 \, nm) \approx 100 \frac{mJ}{cm^2}$ correspond to the published values in the literature [159]. Furthermore, no obvious dependence of the dopant concentration can be established at $800 \, nm$ incident wavelength. The two-fold variation of the threshold fluence around a $100 \frac{mJ}{cm^2}$ could be caused by slightly varying focusing conditions during the experiment.

Fig. 7.5 depicts the threshold measurements on c:GaAs for in incident wavelength of $2 \, \mu m$. The graphs show a modification threshold of approximately $F_{th}(c:GaAs, \lambda = 2 \, \mu m) \approx 35 \frac{mJ}{cm^2}$ for doped and intrinsic c:GaAs. This is a slight decrease in the threshold fluence compared to that at

$800\ nm$ wavelength. One might have expected a greater difference due to the change in the absorption regime from direct absorption to 3-photon absorption (3PA).
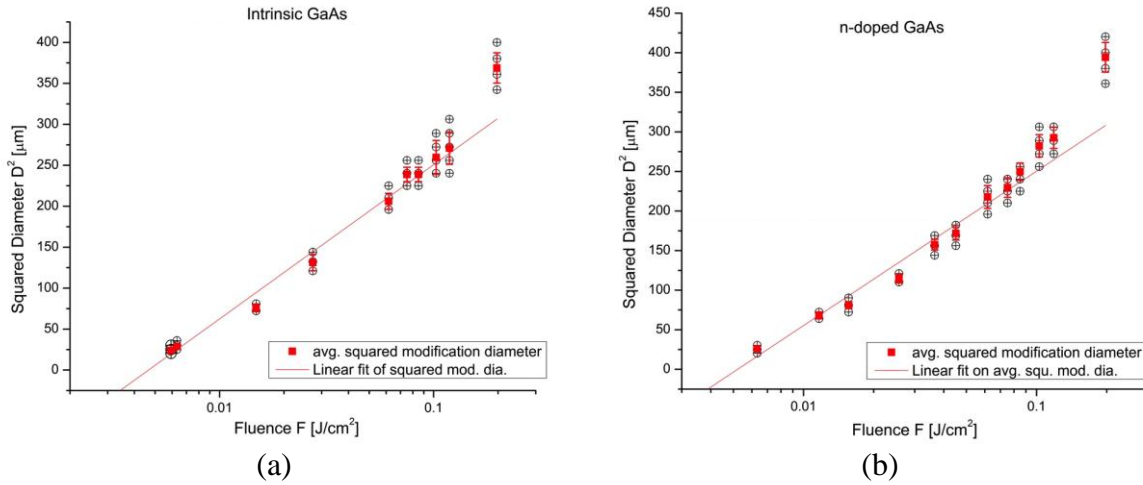
Fig. 7.5 - Graphs of modification threshold fluence of (a) intrinsic c:GaAs and (b) n-doped c:GaAs at an incident wavelength of $2\ \mu m$

The threshold fluences for the various dopant concentration of c:Si are depicted in Fig. 7.6(a) and Fig. 7.6(b) at incident wavelength of $1.3\ \mu m$ and $2.4\ \mu m$, respectively.

The graphs indicate, as before in the NIR, there is no apparent dependence on the dopant type or concentration. The measured modification threshold fluences are approximately $F_{th}(c:Si, \lambda = 1.3\ \mu m) \approx 30\ \frac{mJ}{cm^2}$ and $F_{th}(c:Si, \lambda = 2.4\ \mu m) \approx 20\ \frac{mJ}{cm^2}$. Just as for c:GaAs, such reduction in the threshold fluence was unexpected here due to the change in the absorption regime from linear to 2PA and 3PA, respectively. However, the fluence itself is inversely dependent on the wavelength as the following equation shows

$$F(\lambda) = \frac{P_{inc}}{A(w_0)} = \frac{P_{inc}}{\pi w_0^2} = \frac{P_{inc}}{\pi \cdot \left(1.22 \frac{\pi \lambda}{NA}\right)^2}.$$

(7.1)
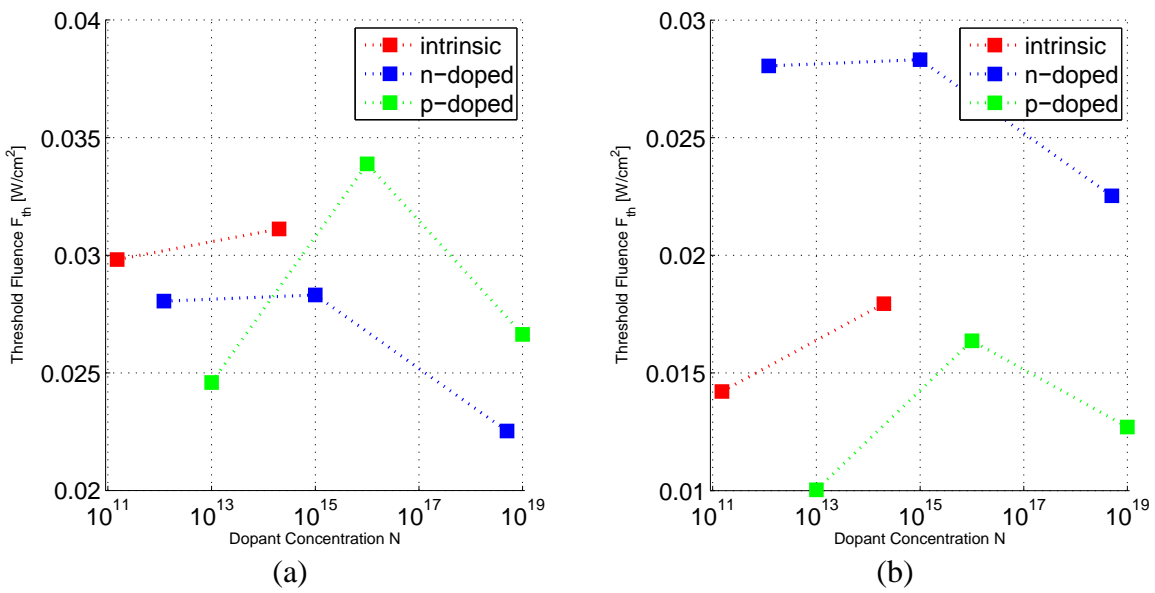
Fig. 7.6 - Graphs of the modification threshold fluences for as function of dopant concentration in c:Si for (a) 1.3 μm and (b) 2.4 μm incident wavelength

Therefore it becomes obvious that the fluence is inversely proportional to the square of the wavelength. However, the pulse energy is independent of the incident wavelength. For an easier understanding of the dependence of the modification threshold as a function of incident photon energy, Fig. 7.7 depicts the threshold pulse energy vs. photon energy.
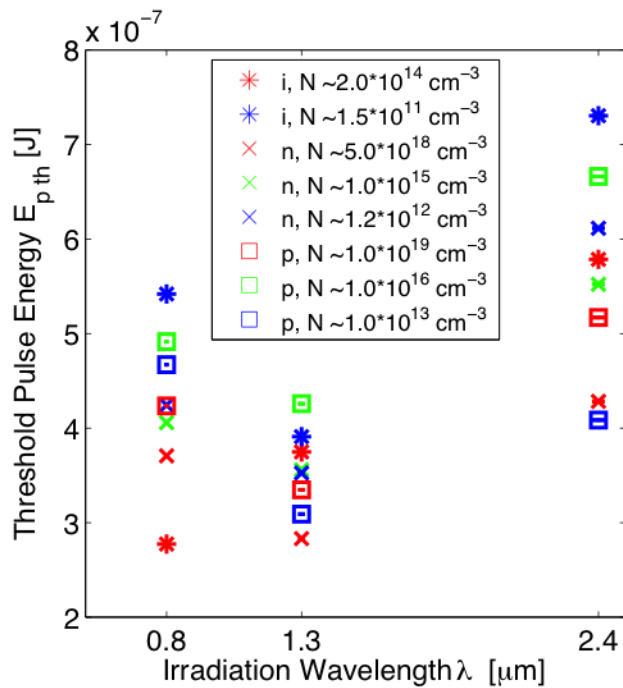
Fig. 7.7 - Graph of the modification threshold pulse energy vs. incident wavelength for various c:Si specimens

The graph shows clearly that the modification threshold pulse energy of the investigate Silicon specimens were within the same order of magnitude for all three wavelength. This reflects a similar result as observed in c:GaAs. The theoretical absorption regime, however, changed from linear absorption for $800\ nm$, through 2PA for $1.3\ \mu m$, to 3PA for $2.4\ \mu m$. Due to this change the modification threshold was expected to increase significantly. It can therefore be concluded that non-linear absorption was not the dominant absorption mechanisms for the induced surface modification on the investigated semiconductors for photon energies smaller than the band gap energy.

7.2   Ultrafast Bulk Transmission Measurements

An experiment was then performed which was aimed at the understanding of bulk modification in the semiconductor material as it has been shown before in dielectrics [9]. An important metric for a technology transfer of FLDW from dielectrics to semiconductors is the amount of absorbed energy in the bulk material. In the case of dielectrics, approximately 20% to 50% of the incident energy is absorbed during the modification process [128]. To verify the absorption during semiconductor bulk processing, the transmitted power through an intrinsic c:GaAs sample was measured as a function of focusing depth, focusing power and repetition rate for an incident wavelength of $\lambda_{IN} = 1043\ nm$. Fig. 7.8 illustrates the used setup, which is basically an open-aperture z-scan technique [217]. The focusing objective used had an NA of 0.1.
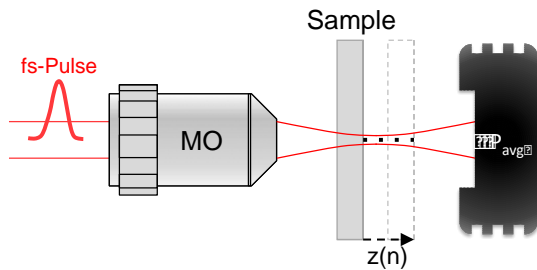
Fig. 7.8 – Scheme of semiconductor bulk transmission measurement setup

Fig. 7.9 shows the measured normalized transmitted power through the **500 μm** thick sample wafer for three focusing conditions at NAs of 0.25, 0.4, and 0.5 at pulse repetition rates of 0.1, 1, and 5 MHz. The most-left value in each curve in Fig. 7.9(a), (b) and (c) corresponds to the event of surface ablation. The focusing depth is given in terms of sample translation in air. The effective focusing depth in the wafer corresponds to the product of focusing depth and the refractive index for c:GaAs of 3.4.
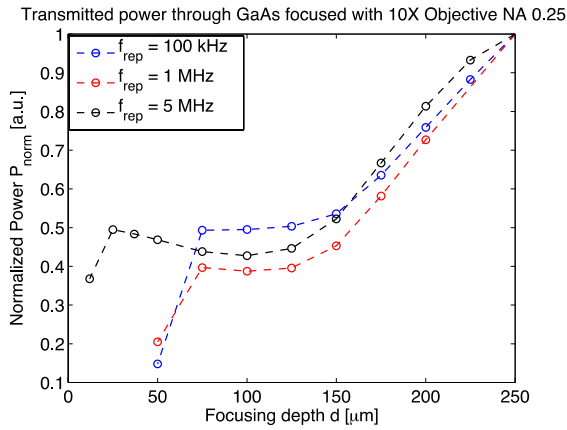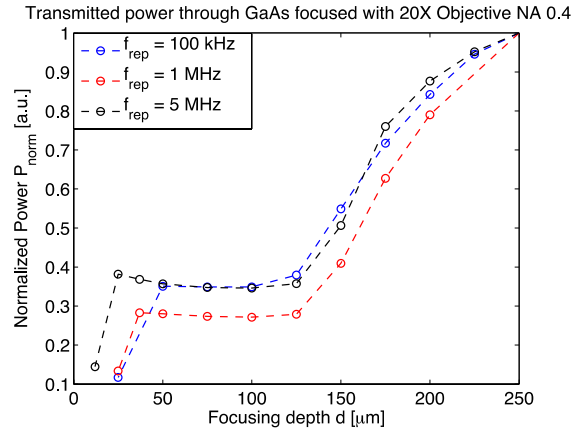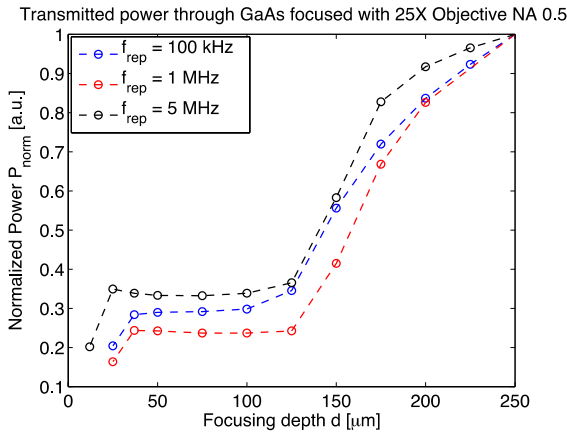
Fig. 7.9 – Graphs of measured transmitted power vs. focusing depth during ultrashort-pulsed irradiation of intrinsic c:GaAs for repetition rates 0.1, 1, and 5 MHz for focusing NAs of (a) 0.25, (b) 0.4, and (c) 0.5

Accounting for Fresnel reflection at the incident surface of approximately 30%, it is apparent that in any case less than 25% of the effectively incident energy in the bulk material was transmitted. Such transmission results are similar to the reported transmission values for bulk modification in dielectrics.

156

7.3   Ultrafast Bulk Modification of Semiconductors

Waveguide-writing in bulk silicon material was previously reported in ref. [15], [218]. In the reported experiments, the sample possessed a thick oxide layer with a thickness of $t_{SiO_2} = 25\ \mu m$. The influence of this oxide layer on the possibility to induce bulk modification so far has not been studied in detail.

To investigate the induced modification in the bulk of semiconductor material with no or only very thin oxide layers[8], intrinsic c:GaAs and c:Si samples with natural oxide layers were irradiated using a meander pattern as depicted in Fig. 7.10. The pulse energy and polarization of the incident radiation were varied during the experiment within the parameter space reported by ref. [15], [218]. The samples were then cleaved in the middle of the irradiated tracks as shown in Fig. 7.10 and inspected using a light microscope (images not shown). No evidence for modification of the bulk material could be found.
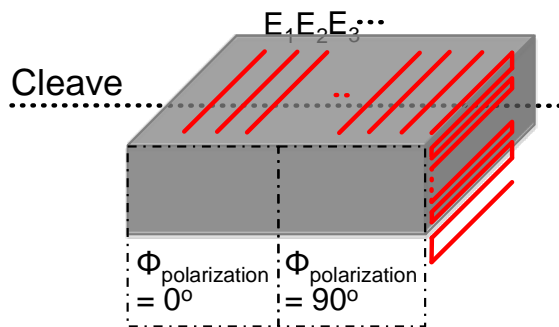
Fig. 7.10 - Scheme of semiconductor bulk irradiation showing the meander pattern adopted

To verify the findings of missing modification tracks in the bulk of the material, a second experiment was performed. The same intrinsic c:GaAs and c:Si base-material were irradiated with

---

[8] The natural oxide layer is only a few tens of nanometers thick.

a grating pattern in the bulk of the sample using $100\,fs$ pulsed $2\,\mu m$ radiation, as demonstrated before in dielectrics [219]. A cw-IR-probe-beam from a diode-laser source (Lucent D2502G fiber-coupled diode on Newport Butterfly diode mount, ILX Lightwave driver) was then passed through the post-irradiated samples at the locations of the expected grating pattern. The transmitted intensity profile of the probe-beam was captured for each sample using an IR-sensitive beam-camera (Spiricon PyroCam). A scheme of the setup is shown in Fig. 7.11(a). If bulk modification due to the irradiation with ultrashort-pulsed laser radiation occurred, a diffraction pattern as depicted in Fig. 7.11(b) was expected to be captured by the beam camera.
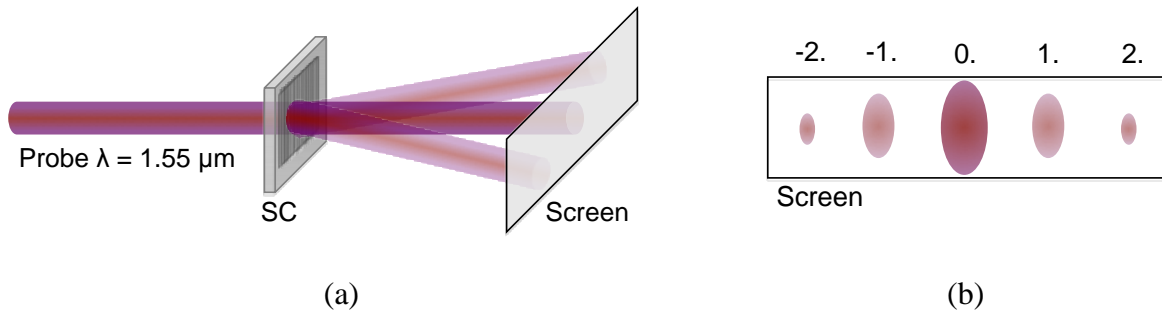
Fig. 7.11 - (a) Scheme of grating test setup using cw-IR-probe-beam and IR-sensitive beam-camera; (b) expected output-profile captured by the beam-camera

The actual recorded intensity profiles for c:GaAs and c:Si are shown in Fig. 7.12 (a) and (b), respectively. No diffraction pattern matching the irradiated grating pattern was observed for the investigated irradiation parameter space.

<center>(a)   (b)</center>
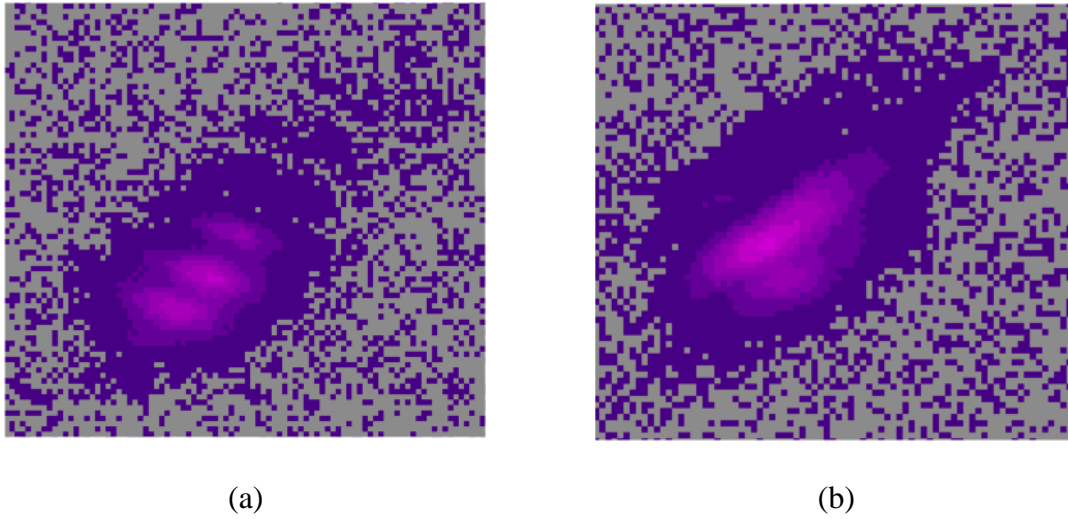
Fig. 7.12 – Intensity profile of probe-beam output as captured by beam-camera from (a) c:GaAs and (b) c:Si sample

7.4   Simulation Results

7.4.1   Surface Modification

Using the non-linear propagation and absorption model, the electron density due to ultrashort irradiation was calculated for incident wavelength of 800 nm, 1.3 μm, and 2.4 μm on intrinsic Silicon. The material parameter values for Silicon in the model used are listed in Table 7-2.

First, the focus was set on the surface of the sample to compare the simulation results to the modification threshold experiment. Additionally, the topological surface profiles of a single irradiation site were recorded for all three incident wavelengths using a white-light interferometer measurement (ZYGO NewView 6000). Fig. 7.13 depicts (a) a microscope image of the ablation spot, (b) the depth profile of that ablation spot, and (c) the simulated non-degenerative electron density, all for 800 nm (top), 1.3 μm (middle), and 2.4 μm (bottom). Here the surface fluence was kept constant at $F_{surface} \cong 0.25 \, J/cm^2$ as well as the focusing objective with a NA of 0.25.

<center>159</center>

Table 7-2 - Material parameter used for the propagation model and Silicon

	Definition	Unit	Value
$n(800\ nm)$	Refractive index	1	3.69409
$n(1.3\ \mu m)$	Refractive index	1	3.50849
$n(2.0\ \mu m)$	Refractive index	1	3.45268
$n(2.4\ \mu m)$	Refractive index	1	3.44143
α	Linear absorption coefficient	m^{-1}	$1.3 \cdot 10^4$
β_2	2PA absorption coefficient	$\dfrac{m^4}{W^2}$	$4.918 \cdot 10^{-21}$ [220]
β_3	3PA absorption coefficient	$\dfrac{m^6}{W^3}$	$9.433 \cdot 10^{-34}$ [221]
$\alpha_{avalanche}$	Avalanche coefficient	$\dfrac{m^2}{W}$	$1.0 \cdot 10^{-2}$ [222]
n_2	Non-linear refractive index	$\dfrac{m^2}{W}$	$5.7 \cdot 10^{-18}$ [220]
ρ_{atom}	Atomic density	m^{-3}	$1.6 \cdot 10^{28}$
C	Electric conductivity	$\Omega \cdot m$	$4 \cdot 10^2$
t_{recomb}	Electron recombination time	fs	100 [222]
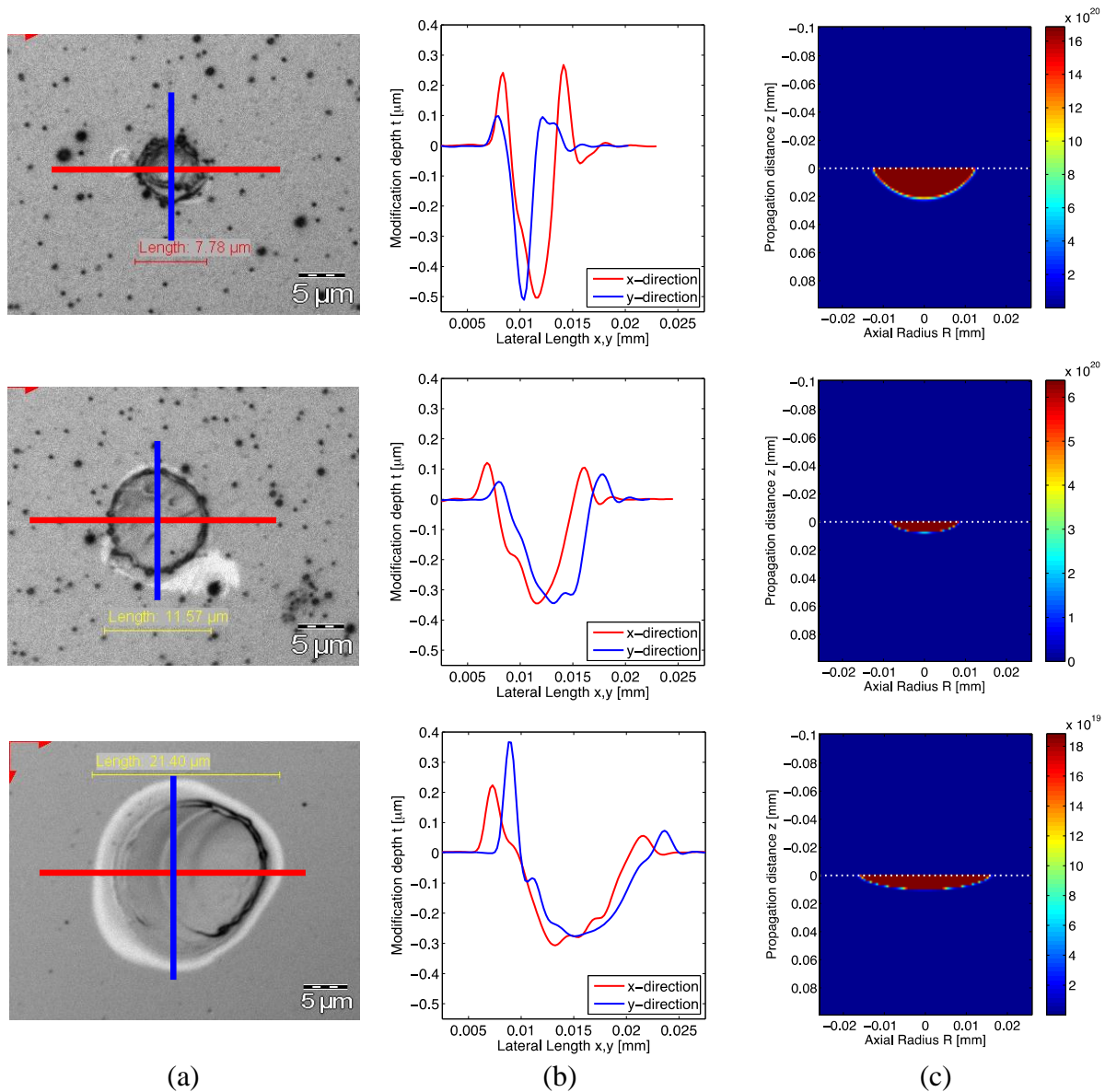
Fig. 7.13 – Series of (a) microscope surface images, (b) topological surface profiles and (c) simulated electron density profiles for $800\,nm$ (top), $1.3\,\mu m$ (middle), and $2.4\,\mu m$ (bottom) at $F_{surface} \cong 0.25\,J/cm^2$ and $NA = 0.25$

The depth profiles (column (b)) indicate that the pulse penetrates deeper at shorter wavelengths. This trend corresponds to the simulation results, which show that the laser-induced

electron density is much shallower at $1.3\ \mu m$ and $2.4\ \mu m$ wavelengths when compared to $800\ nm$ incident wavelength. This reduced penetration depth was unexpected because the absorption regime was believed to change from linear at $800\ nm$ to 2PA and 3PA for $1.3\ \mu m$ and $2.4\ \mu m$ wavelengths, respectively. The reduced penetration depth would however correspond to the reduction of the critical electron density for longer wavelengths, which is given as

$$N_c(\lambda) = \left(\frac{2\pi c}{e}\right)^2 \frac{\epsilon_0 m_e}{\lambda^2}. \qquad\qquad (7.2)$$

One aspect worth noting is that these results suggested again that the primary absorption mechanism seemed neither to be MPI nor free-carrier absorption. The same observation was made previously for the modification threshold.

Regarding the influence of the dopant concentration, several different concentrations were simulated at an incident wavelength of $2.4\ \mu m$. The wavelength of $2.4\ \mu m$ was chosen because the corresponding photon energy required 3PA to occur to bridge the band gap. Fig. 7.14 illustrates the calculated electron densities at the end of a $100\ fs$ laser pulses for (a) $1.5 \cdot 10^{11}\ cm^{-3}$, (b) $2 \cdot 10^{14}\ cm^{-3}$, and (c) $2 \cdot 10^{19}\ cm^{-3}$ doped Silicon samples. The end of the pulse was chosen because at that time all energy contained in the pulse was incident and possibly absorbed. The pulse energy was set to $100\ nJ$.
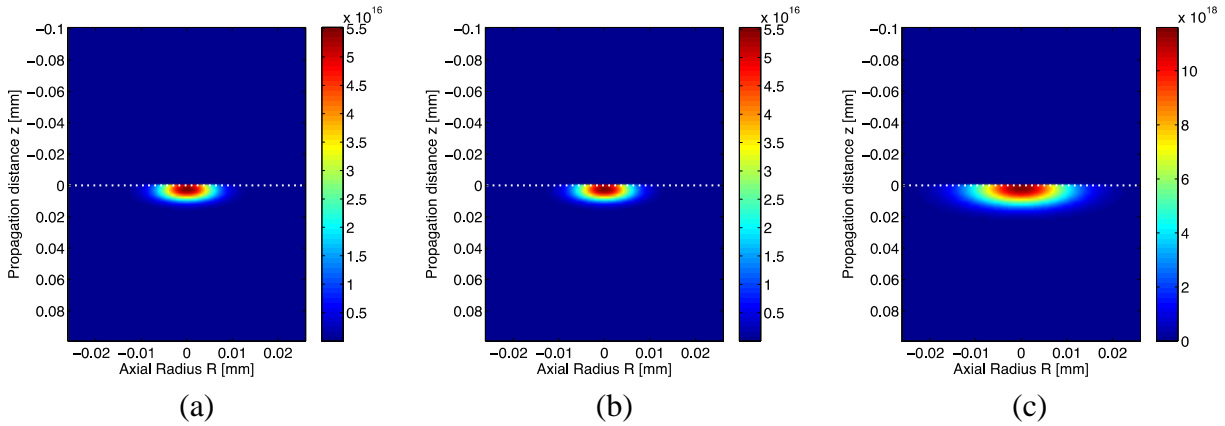
Fig. 7.14 - Graphs of simulated electron density on Silicon surface due to an incident ultrashort $100\ nJ$ pulse at a wavelength of $2.4\ \mu m$ for dopant concentrations of (a) $1.5 \cdot 10^{11}\ cm^{-3}$, (b) $2 \cdot 10^{14}\ cm^{-3}$, and (c) $2 \cdot 10^{19}\ cm^{-3}$ with a pulse energy of $E_p = 100\ nJ$

It is apparent from the figure that the laser-induced electron density is the same for $1.5 \cdot 10^{11}\ cm^{-3}$ and $2 \cdot 10^{14}\ cm^{-3}$ doped Silicon and the utilized parameter set. However, for $2 \cdot 10^{19}\ cm^{-3}$ doped silicon, the laser-induced electron density is approximately two orders of magnitude higher. Moreover, the experimental results reported by Leyder *et al.* [223] coincide with outcomes from the model implemented here for low incident pulse energies of only $E_p = 100\ nJ$, at which no influence of the dopant concentration was seen in the simulated electron density up to an approximately concentration of $2 \cdot 10^{18}\ cm^{-3}$. Fig. 7.15 shows the full plot of the simulated electron densities achieved at the end of the $100\ fs$ laser pulse against dopant concentration and incident pulse energy. It is apparent from the graph that the pulse energy is the primary factor of induced electron density up to a critical dopant concentration. That concentration was coinciding with the critical electron density for the low level pulse energy of $100\ nJ$. However, at higher incident pulse energies $E_p > 250\ nJ$, all specimens, independent of their

dopant concentration quickly reach critical electron density, where the tail of the incident pulse is reflected due plasma reflection. It should be pointed out that a pulse energy of $300 \, nJ$ corresponds to a fluence of only $4 \, mJ/cm^2$, which is approximately one order of magnitude below the surface modification threshold.
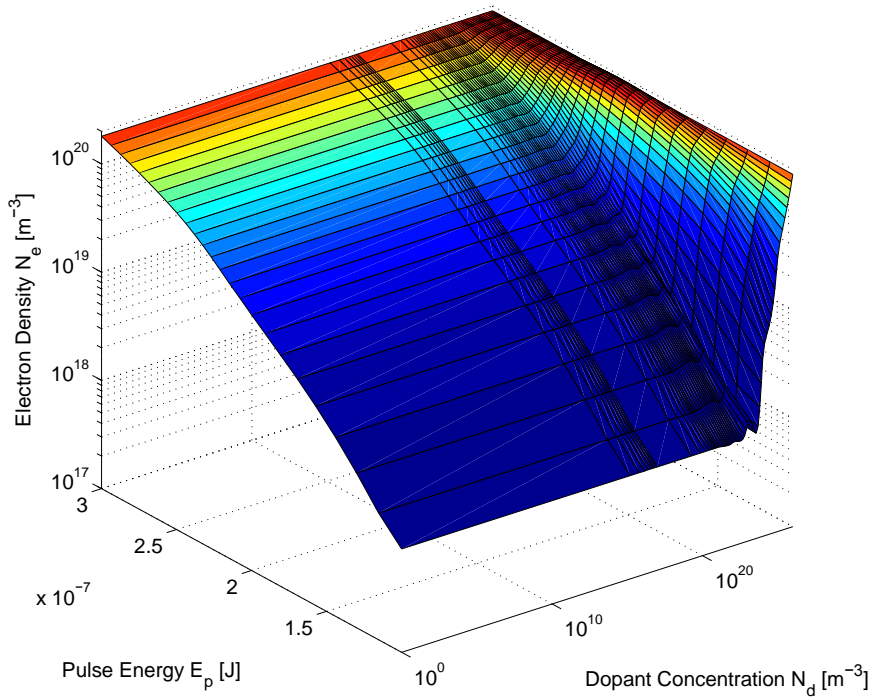
Fig. 7.15 - Simulated graph of electron density due to incident laser radiation as function of dopant concentration and pulse energy E_p for silicon

7.4.2   Bulk Modification

Another set of simulations was conducted for bulk modification at a wavelength of $2.0 \, \mu m$. Therefore, the focus was set at a depth of $t_{focus} = 30 \, \mu m$ below the surface of intrinsic Silicon with a dopant concentration of $1.5 \cdot 10^{11} \, cm^{-3}$. The focusing NA was 0.5 and the pulse energy was $E_p = 1 \, \mu J$. The material parameters necessary for the model are listed in Table 7-2. Fig.

7.16(a) illustrates the laser-induced accumulated electron density and Fig. 7.16(b) the on-axis electron density evolution.
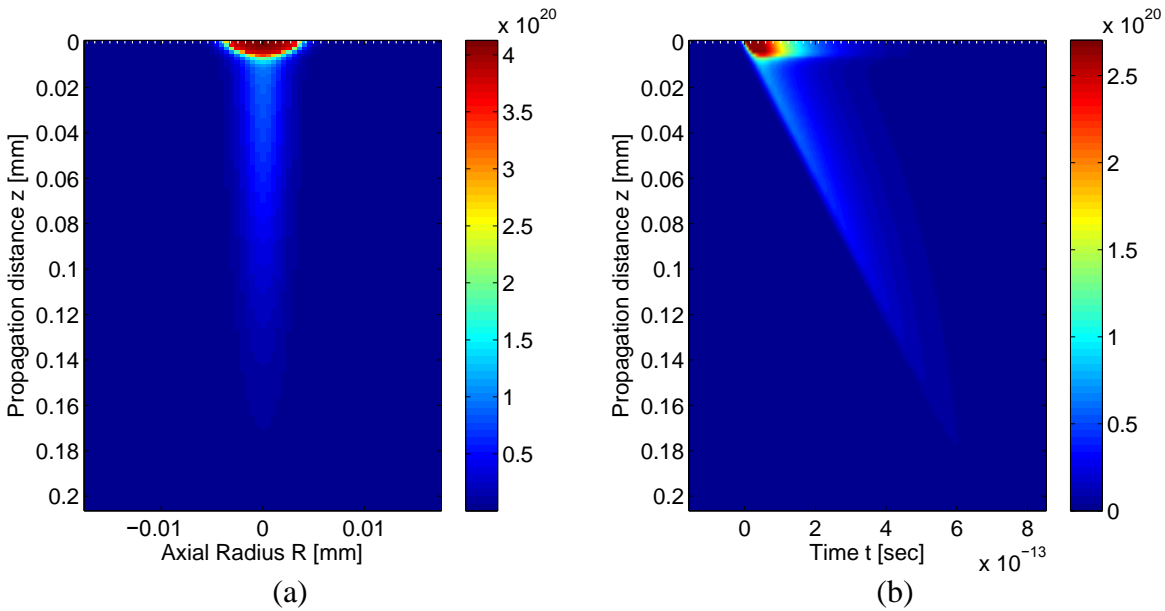
Fig. 7.16 - Graphs of simulated (a) accumulated electron density and (b) electron density evolution at $r = 0$ for ultrashort pulse irradiation focused in the bulk of intrinsic c:Si

Fig. 7.16(b) depicts that the electron density on the input facet of the sample quickly rises to critical electron density, with the leading edge of the pulse. At that point, most of the incident energy is reflected off of the electron cloud. Only a small portion of this is actually focused in the bulk material.

Obviously, the incident pulse energy can be reduced to a level at which the pulse can indeed penetrate the material, approximately $300 \, nJ$. However, comparing the corresponding fluence to the surface modification threshold, which in general is lower than the bulk modification threshold due to impurities and free bonds on the edge, it becomes apparent that pulse modification cannot be achieved with these wavelengths.

7.5   Ultrafast Back-Side Surface Structuring of Semiconductors

Because of the non-transparent character of semiconductors in the visible region of the spectrum, it is difficult to observe bulk modification by microscopic means as is commonly done with dielectrics. Therefore, a simple approach of testing the possibility of bulk modification is to modify the back-side surface of the sample material by focusing through the sample. Using ultrashort-pulsed laser radiation at the wavelengths $\lambda_1 = 1043\ nm$ and $\lambda_2 = 2\ \mu m$ and under the condition that the front surface was not ablated, no evidence of back-side modification could be found. Changing to longer pulses with durations in the ns-range, back-side ablation using $2\ \mu m$ radiation was possible, as depicted in Fig. 7.17.
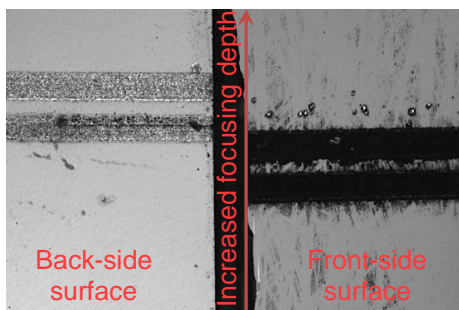
Fig. 7.17 - Microscope image of ablation tracks using 2μm ns-pulsed radiation on the front-
and back-side of an intrinsic c:GaAs wafer at varying focusing depths

7.6   Conclusion of Semiconductor Laser Processing

The conducted experiments in the transparent region have shown that bulk modification of c:GaAs or c:Si was not possible. The reasons were two-fold. When sufficient pulse energy for modification was incident on the sample, the leading edge of the pulse caused an extremely fast rise of the electron density to critical density. At that point, the electron cloud reflected the majority of the incident pulse and therefore insufficient energy for modification was focused inside the

sample. By extending the pulse duration as shown in the back-side ablation experiment, the peak intensity was significantly lowered and the electron density grew slower accordingly, allowing the main pulse to penetrate the sample. Moreover, it has been shown that the pulse energy necessary for surface modification is larger than the pulse energy sufficient to reach critical electron density. This means that simple reduction of pulse energy was insufficient to overcome the bulk modification threshold.

With regard to the dependence of the dopant concentration, the propagation model developed here verified that the absorption is independent of the dopant concentration. However, the modification threshold was independent of dopant concentration and incident photon energy. The experiments have illustrated that the threshold fluence follows a λ^{-2} curve regardless of the absorption regime (linear, 2PA, or 3PA). This means that avalanche ionization is the primary absorption mechanism. The seed electrons for the avalanche process are generated by MPI during the leading edge of the pulse or readily available due to the dopant concentration.

7.7   Future experiment

To test the here developed theory a time-resolved reflection experiment is proposed for future studies of the matter.

7.7.1   Time-resolved Ultrafast Transmittance of Semiconductors

The classical light-matter-interaction picture is based on a steady-state condition of the physical mechanisms involved such as a constantly oscillating EM-field of the radiation and a thermo-dynamic equilibrium of the matter present. On the contrary, when dealing with ultrashort-pulsed laser radiation, such a steady-state condition is not present. The radiation pulse is too short to interact with matter in a thermo-dynamic equilibrium condition [74], [224], as pointed out in

167

Section 2.2. Therefore, transient responses will dominate the interaction picture and cause the response to be different from the known steady-state response. One particular phenomenon of interest is the ultrafast transmittance of semiconductor materials due to an incident ultrashort laser pulse with a photon-energy below the band gap energy of the material. Whereas in a steady-state condition, the material will be transparent to the radiation; in a transient state a high reflectance can occur due to absorption followed by a transient electron plasma.

Knowledge of how much of the incident energy is transmitted into the bulk material is essential to predict if the material can be modified in the focal region using the FLDW technique. To measure the amount of transmitted energy a pump-probe reflectance measurement should be conducted similar to the experiments in ref. [225], [226], but the excitation wavelength should be changed to $1.3 \, \mu m$ and $2.0 \, \mu m$ for probe- and pump-beam, respectively.

7.7.1.1 Experimental Approach

The outputs of the OPA at $2.0 \, \mu m$ and $1.33 \, \mu m$ are used for pump and probe beams, respectively. Both wavelengths can be extracted from the OPA simultaneously with a known temporal offset of approximately $180 \, ps$. The probe beam is then steered over a micro-positioning stage to allow the variation of the temporal offset of either beam with respect to the other, as shown in Fig. 7.18.
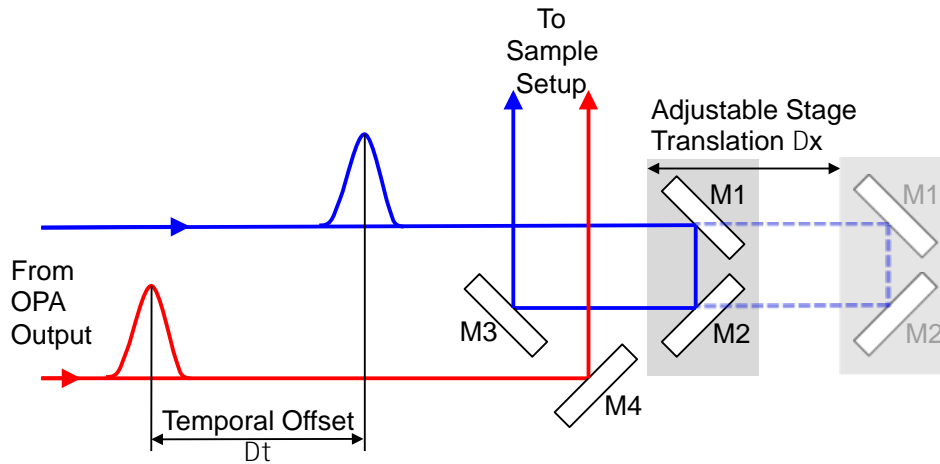
Fig. 7.18 - Schematic of a simple delay line to adjust temporal offset of to pulses to each other with M1 and M2 as translation mirrors and M3 and M4 as stationary mirrors

The temporal offset is here related to the translation of the stage by

$$\Delta x = \frac{1}{2}\Delta t \cdot c\,[m].$$ (7.3)

with Δx and Δt being the translation distance of the stage and the temporal delay of the two pulses to each other, respectively. After correction of the initial offset the maximum achievable delay between the two pulses is approximately $150\ ps$ corresponding to a translation distance of $2.25\ cm$.

The pump beam is focused on the semiconductor sample at an incident angle of approximately 45°. A microscope objective is positioned such that the probe radiation can be used as an illumination source to image the sample surface. The reflection from the sample surface is imaged on to a CCD camera sensitive to mid-IR radiation (Fig. 7.19).
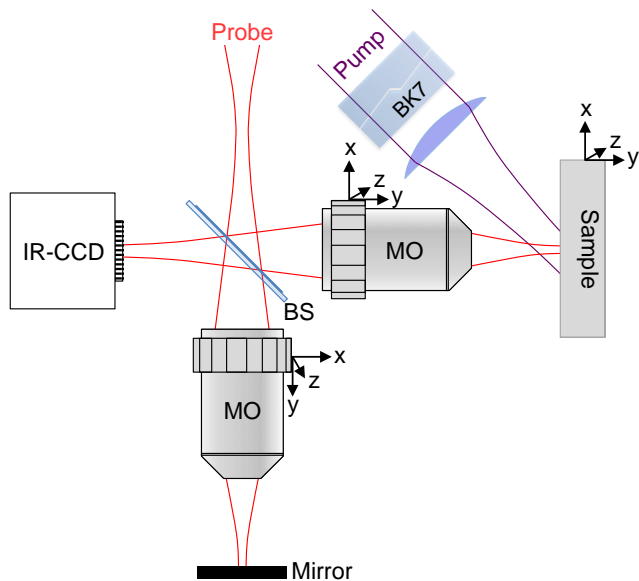
Fig. 7.19 - Schematic of pump-probe ultrafast reflectance measurement setup; BS: beam splitter, MO: microscope objective

The IR-CCD will first be calibrated with reflected probe radiation without a pump beam present on the sample. After successful calibration the pump will be passed onto the sample surface and the amount of reflected radiation will be recorded at varying time delays.

7.7.1.2   Expected Results

Many studies regarding the dynamics of ultrafast light-matter interaction focus on the transient phase changes of the matter during and within several picoseconds after the pulse [225], [227]-[229]. The excitation wavelength is thereby, in general, non-transmissive for the probe material.

Here, information can be deduced about the ultrafast transmittance through the material boundary when the photon energies of the incident radiation are insufficient to bridge the band gap directly. Furthermore, the temporal window will concentrate on the effects during the laser pulse itself.

With the data acquired, an accurate prediction can be drawn of how much energy is transmitted from an incident pulse into the bulk of the sample.

7.7.1.2.1 Technical Challenges

In an ideal case, the probe pulse should be temporally shorter with respect to the pump pulse to enable temporal resolution throughout the incident event. However, both pulses have approximately equal temporal duration when exiting the OPA. To stretch the pump pulse in time it will be passed through a dispersive element with known properties, such as Fused Silica or BK7. Using the increased material dispersion in such media, a $100\ fs$ pulse, covering $\Delta\lambda = 100\ nm$ 10 dB bandwidth at a center wavelength of $2\ \mu m$, will be stretched to $300\ fs$ passing through $10\ cm$ of i.e. BK7 glass.

8 CONCLUSION

This thesis aims to advance the development of the Femtosecond Laser Direct Writing technique for photonic applications in bulk material. It examines changes occurring in the light-matter interaction process, specifically in absorption regimes present when using high repetition rate femtosecond pulsed radiation. The results suggested, specifically with regard to the extension of the FLDW technique from dielectric to semiconductor materials, that a scaling of the laser wavelength towards the IR alone is not sufficient to introduce modifications in bulk c:GaAs or c:Si. Even though non-linear processes are still dominant using ultrashort pulses, the presence of enhanced avalanche ionization prohibits bulk modification.

In another study it was shown that 3D FLDW can introduce a positive refractive index of up to $5 \cdot 10^{-5}$ in bulk Telluride glass. Even though this index change is not as high as previously achieved in other dielectrics, it resulted in the first direct inscription of a wave-guiding structure in Te-glass-family. The increase of the refractive index in the core of the guide is thought to be due to the migration of La-atoms from the core into the surrounding volume.

The use of high repetition rate femtosecond lasers to irradiate in the bulk of dielectrics such as Fused Silica, aluminumsilicate glass, or FOTURAN® glass, led to the formation of novel nano-fibers on the surface of such dielectrics. To extend the understanding of this novel formation process, a broad range of materials and irradiation conditions was investigated. It was demonstrated that there exists a correlation between heat-accumulation during the irradiation process and the occurrence of nano-fibers. A model was developed to predict the temperature in the irradiated bulk material. It was found that this temperature exceeded the melting temperature in the focal volume, and that the high rate of energy deposition gave rise to the formation of nano-

fiber on the sample surface. A qualitative model of the nano-fiber formation process was developed (Section 5.4) on the basis of the obtained results.

Special interest was paid to the heat accumulation process itself. It was shown (Section 5.3.1) that the initial non-linear absorption regime is followed by an additional quasi-linear absorption regime when the conditions for heat accumulation were met. This quasi-linear regime is thought to be driven by simple electron heating of the laser-induced plasma. Post-irradiation measurements of the radial and axial expansion of the laser-modified region showed that the modification grew faster in the z-direction towards in the incident beam. This result is consistent with an absorption mechanism based on electron heating in the heat-accumulation regime.

On semiconductor surfaces, the reproducible generation of parallel Laser Induced Periodic Surface Structures (LIPSS) with respect to the incident E-field orientation was shown at $2 \ \mu m$ radiation wavelength is shown in 6. The model suggested by Bonse, on the basis of the Sipe's theory of LIPSS formation, was extended to predict the periodicity of this parallel structure. Moreover, the development of LIPSS has been categorized in three different regimes, which led to parallel-LIPSS (P-LIPSS) at low, Low Spatial Frequency LIPSS (LSFL) at moderate, and High Spatial Frequency LIPSS (HSFL) at high accumulated fluences.

The feasibility of semiconductor bulk modification using conventional 3D FLDW scheme used for dielectrics was investigated. The surface modification threshold due to femtosecond laser irradiation was found to be independent of the excitation wavelength and therefore independent of the multi-photon absorption scheme. In addition, the dopant concentration of the irradiated samples could not conclusively be correlated to the modification threshold in experiments. A model of the propagation and absorption process of ultrashort laser pulses was developed and

revealed that a dependence of the modification threshold on the dopant concentration is unlikely. Independent published research supports theses results, as summarized in section (Section 7.1).

The results in 7 suggest that the absorption mechanism dominant during femtosecond irradiation of semiconductors is avalanche ionization. Due to the rapid rise in electron density on the surface of the irradiated sample, it was not possible to achieve sufficient energy input into the bulk of the material to overcome the modification threshold. Moreover, the model suggests that the greater part of the pulse is reflected from the critical density in the laser-induced electron plasma.

Continued research is necessary to fully understand the ultrafast phenomena occurring during femtosecond irradiation of semiconductor material. The results presented in this thesis present a good basis for further investigations.

REFERENCES

[1]   S. Nolte, C. Momma, H. Jacobs, A. Tünnermann, B. N. Chichkov, B. Wellegehausen, and H. Welling, "Ablation of metals by ultrashort laser pulses," *J Opt Soc Am B*, vol. 14, no. 10, p. 2716, 1997.

[2]   M. Shirk and P. A. Molian, "A review of ultrashort pulsed laser ablation of materials," *Journal of Laser Applications*, vol. 10, no. 1, p. 18, Jan. 1998.

[3]   G. Dumitru, V. Romano, H. P. Weber, M. Sentis, and W. Marine, "Femtosecond ablation of ultrahard materials," *Applied Optics*, vol. 74, no. 6, pp. 729–739, Jun. 2002.

[4]   A. Zoubir, L. Shah, K. C. Richardson, and M. C. Richardson, "Practical uses of femtosecond laser micro-materials processing," *Applied Optics*, Jan. 2003.

[5]   J. Choi, R. Bernath, M. Ramme, and M. C. Richardson, "Increase of ablation rate using burst mode femtosecond pulses," *Optical Society of America-CLEO/QELS Conference*, Jan. 2007.

[6]   D. Bäuerle, *Laser Processing and Chemistry*, Fourth Edition. Springer Verlag, 2011.

[7]   K. Davis, K. Miura, N. Sugimoto, and K. Hirao, "Writing waveguides in glass with a femtosecond laser," *Opt. Lett.*, vol. 21, no. 21, pp. 1729–1731, Oct. 1996.

[8]   J. Choi, M. Ramme, T. Anderson, and M. C. Richardson, "Femtosecond laser written embedded diffractive optical elements and their applications," presented at the Proceedings of SPIE, 2010, vol. 7589, p. 75891A.

[9]   K. Sugioka and S. Nolte, "3D Fabrication of Embedded Microcomponents," *Laser Precision Microfabrication*, Jan. 2010.

[10]   M. Ams, G. D. Marshall, P. Dekker, and J. Piper, "Ultrafast laser written active

        devices," *Laser & Photonics Reviews*, vol. 10, Jan. 2008.

[11]   E. A. Romanova, A. I. Konyukhov, D. Furniss, A. B. Seddon, and T. M. Benson,

        "Femtosecond Laser Processing as an Advantageous 3-D Technology for the

        Fabrication of Highly Nonlinear Chip-Scale Photonic Devices," *J Lightwave

        Technol*, vol. 27, no. 15, pp. 3275–3282, Aug. 2009.

[12]   C. Monat, P. Domachuk, and B. J. Eggleton, "Integrated optofluidics: A new river of

        light," *Nature Photon*, vol. 1, no. 2, pp. 106–114, 2007.

[13]   M. Ams, D. Little, R. Williams, and G. D. Marshall, "Overview of laser

        microfabrication techniques for photonic devices," *... 2008 and the 2008 Australian

        Conference on Optical ...*, Jan. 2008.

[14]   A. Lee, B. Johnston, M. Ams, J. Dawes, and J. Piper, "Fabrication of photonic

        devices using novel laser-assisted methods," *Proceedings of SPIE*, Jan. 2004.

[15]   J. Burghoff, M. Will, S. Nolte, A. Tünnermann, A. H. Nejadmalayeri, and P. R.

        Herman, "Photonics in silicon using mid-IR femtosecond pulses," presented at the

        Proceedings of SPIE, 2005, vol. 5714, pp. 245–252.

[16]   Y. Ma, H. Shi, J. Si, T. Chen, F. Yan, F. Chen, and X. Hou, "Photoinduced

        microchannels and element change inside silicon by femtosecond laser pulses,"

        Optics ..., pp. 1–3, Sep. 2011.

[17]   B. Jalali and S. Fathpour, "Silicon Photonics," *J Lightwave Technol*, vol. 24, no. 12,

        pp. 4600–4615, Dec. 2006.

[18]   A. W. Topol, D. L. Tulipe, L. Shi, D. J. Frank, K. Bernstein, S. E. Steen, A. Kumar,

G. U. Singco, A. M. Young, and K. W. Guarini, "Three-dimensional integrated circuits," *IBM Journal of Research and Development*, vol. 50, no. 4, pp. 491–506, 2006.

[19]   L. D. Browning, J. M. Beyer, and J. C. Shetler, "Building cooperation in a competitive industry: SEMATECH and the semiconductor industry," *Academy of Management Journal*, pp. 113–151, 1995.

[20]   D. A. Irwin and P. J. Klenow, "High-tech R&D subsidies Estimating the effects of Sematech," *Journal of International Economics*, vol. 40, no. 3, pp. 323–344, 1996.

[21]   T. H. Maiman, "Stimulated optical radiation in ruby," *Nature*, vol. 187, pp. 493–494, 1960.

[22]   K. MacLeish and J. Amos, *Leonardo Da Vinci : a man for all ages*, vol. 152, no. 3. National Geographic, 1977, pp. 296–329.

[23]   C. Huygens, *Traité de la lumière*. 1690.

[24]   T. Young, *A course of lectures on natural philosophy and the mechanical arts*. 1807.

[25]   J. Maxwell, "A Dynamical Theory of the Electromagnetic Field," *Philosophical Transactions of the Royal Society of …*, vol. 155, pp. 459–512, 1865.

[26]   M. Born, E. Wolf, and A. B. Bhatia, "Principles of Optics: Electromagnetic Theory of Propagation, Interference and diffraction of light," *Cambridge University Press*, p. 986, Jan. 2000.

[27]   M. Planck, "On the Law of the Energy Distribution in the Normal Spectrum," *Ann Phys*, 1901.

[28]   A. Einstein, "On the electrodynamics of moving bodies," *Ann Phys*, 1905.

[29]   G. N. Lewis, "The conservation of photons," *Nature*, vol. 118, pp. 874–875, 1926.

[30]   A. Einstein, *Strahlungs-Emission und -Absorption nach der Quantentheorie*. 1916.

[31]   A. Einstein, "On the quantum theory of radiation," *Physikalischen Zeitschrift*, vol. 18, no. 121, 1917.

[32]   A. KASTLER, "Optical Methods of Atomic Orientation and of Magnetic Resonance," *Journal of the Optical Society of America*, vol. 47, no. 6, pp. 460–465, 1957.

[33]   P. Ehrenfest, "Weak Quantization," *Phys. Rev*, 1924.

[34]   V. Fabrikant, *On the Problem of an Experimental Proof of the Existence of Negative Absorption*. Tr. VEI, 1940.

[35]   J. Gordon and H. Zeiger, "Molecular Microwave Oscillator and New Hyperfine Structure in the Microwave Spectrum of NH_{3}," *Phys. Rev*, 1954.

[36]   N. Basov and A. Prokhorov, *The Use Of Molecular Bundles In Radiospectroscopic Studies Of Rotating Molecular Spectra*, vol. 27. Soviet Journal of Experimental and Theoretical Physics, 1954, pp. 431–438.

[37]   N. Bloembergen, "Spin relaxation processes in a two-proton system," *Phys. Rev*, vol. 104, no. 6, p. 1542, 1956.

[38]   A. Schawlow and C. Townes, "Infrared and optical masers," *Phys. Rev*, Jan. 1958.

[39]   A. Javan, W. R. Bennett Jr, and D. R. Herriott, "Population inversion and continuous optical maser oscillation in a gas discharge containing a He-Ne mixture," *Phys Rev Lett*, vol. 6, no. 3, pp. 106–110, 1961.

[40]   C. Patel, "Interpretation of CO_{2} Optical Maser Experiments," *Phys Rev Lett*, vol. 12, no. 21, pp. 588–590, May 1964.

[41]   J. E. GEUSIC, H. M. MARCOS, and L. G. Van Uitert, "LASER OSCILLATIONS IN Nd- DOPED YTTRIUM ALUMINUM, YTTRIUM GALLIUM AND GADOLINIUM GARNETS," *Appl Phys Lett*, vol. 4, no. 10, pp. 182–184, 1964.

[42]   F. J. M. R. W. Hellwarth, "Giant Optical Pulsations from Ruby," *Applied Optics*, vol. 1, no. 101, pp. 103–105, Jan. 1962.

[43]   W. G. Wagner and B. A. Lengyel, "Evolution of the Giant Pulse in a Laser," *J Appl Phys*, vol. 34, no. 7, pp. 2040–2046, 1963.

[44]   L. E. Hargrove, R. L. Fork, and M. A. Pollack, "Locking Of He-Ne Laser Modes Induced By Synchronous Intracavity Modulation," *Appl Phys Lett*, vol. 5, no. 1, p. 4, 1964.

[45]   M. DiDomenico Jr, J. Geusic, H. Marcos, and R. Smith, "Generation of Ultrashort Optical Pulses by Mode Locking YAlG:Nd Laser ," *Appl Phys Lett*, vol. 8, no. 7, pp. 180–&, 1966.

[46]   D. Kuizenga and A. Siegman, "FM and AM mode locking of the homogeneous laser--Part I: Theory," *Quantum Electronics, IEEE Journal of*, vol. 6, no. 11, pp. 694–708, 1970.

[47]   K. Sala and M. C. Richardson, "Optical Kerr effect induced by ultrashort laser pulses," *Phys Rev A*, vol. 12, no. 3, pp. 1036–1047, Sep. 1975.

[48]   K. Sala, M. C. Richardson, and N. R. Isenor, "Passive mode locking of lasers with the optical Kerr effect modulator," *Quantum Electronics, IEEE Journal of*, vol. 13,

no. 11, pp. 915–924, 1977.

[49]   W. Knox, M. Downer, R. Fork, and C. Shank, "Amplified femtosecond optical pulses and continuum generation at 5-kHz repetition rate," *Opt. Lett.*, Jan. 1984.

[50]   W. Knox, "Generation and kilohertz-rate amplification of femtosecond optical pulses around 800 nm," *Journal of the Optical Society of America B*, Jan. 1987.

[51]   P. F. Moulton, "Spectroscopic and laser characteristics of Ti: Al 2 O 3," *J Opt Soc Am B*, vol. 3, no. 1, pp. 125–133, 1986.

[52]   M. Birnbaum, "Semiconductor Surface Damage Produced By Ruby Lasers," *J Appl Phys*, vol. 36, no. 11, pp. 3688–&, Jan. 1965.

[53]   M. Bass, "Laser-induced Damage Probability at 1.06, um and 0.69, m," *NBS special publication*, Jan. 1972.

[54]   N. Bloembergen, "Laser-induced electric breakdown in solids," *Ieee J Quantum Elect*, Jan. 1974.

[55]   D. Du, X. Liu, G. Korn, J. Squier, and G. Mourou, "Laser- induced breakdown by impact ionization in SiO2 with pulse widths from 7 ns to 150 fs," *Appl Phys Lett*, vol. 64, no. 23, pp. 3071–3073, 1994.

[56]   D. von der Linde, "Materie in extrem intensiven Laserfeldern," *Naturwissenschaften*, Jan. 1994.

[57]   P. Pronko, S. Dutta, J. Squier, J. Rudd, and D. Du, "Machining of sub-micron holes using a femtosecond laser at 800 nm," *Optics Communications*, vol. 114, pp. 106–110, 1995.

[58]   J. Ion, *Laser processing of engineering materials: principles*. Elsevier Butterworth-

Heinemann, 2005.

[59]   M. M. Ramsay, G. A. Hockham, and K. C. Kao, "Propagation in optical fiber

         waveguides," *Electronics Communications of Japan*, vol. 50, pp. 162–169, 1975.

[60]   M. M. Ramsay, G. A. Hockham, and K. C. Kao, "Lightwaves in fiber lightguides. II

         - Attenuation mechanisms and conclusions," *Nachrichten Elektronik*, vol. 30, pp.

         183–185, Aug. 1976.

[61]   N. B. Livsey, "Apparatus for application of metallic coatings to metallic substrates,"

         26-May-1981.

[62]   D. L. Bourell, J. B. Beaman, M. C. Leu, and D. W. Rosen, "A brief history of

         additive manufacturing and the 2009 roadmap for additive manufacturing: looking

         back and looking ahead," 2009.

[63]   W. Koechner, *Solid-State Laser Engineering*. Springer Verlag, 2006.

[64]   *The theory of laser materials processing: heat and mass transfer in modern

         technology*. Springer, 2009.

[65]   D. A. Belforte, "2012 Annual Economic Review and Forecast," *Industrial Laser

         Solutions*, vol. 28, no. 1, pp. 1–18, 2012.

[66]   R. W. Boyd, *Nonlinear Optics*. Academic Press, 2008.

[67]   M. Fox, *Optical Properties of Solids*, 1st ed. Oxford University Press, 2001.

[68]   E. Kaxiras, *Atomic and Electronic Structure of Solids*. Cambridge Univ Press, 2003.

[69]   P. Drude, "Zur Elektronentheorie der Metalle - Drude - 2006 - Annalen der Physik -

         Wiley Online Library," *Ann Phys*, 1900.

[70]   P. Y. Yu and M. Cardona, *Fundamentals of Semiconductors*. Springer, 2010.

[71]   M. Grundmann, *The physics of semiconductors*, Second Edition. Springer Verlag, 2010.

[72]   N. W. Ashcroft and N. D. Mermin, *Solid state physics*. Harcourt School, 1976.

[73]   D. Strickland and G. Mourou, "Compression of amplified chirped optical pulses," *Optics Communications*, vol. 56, no. 3, pp. 219–221, 1985.

[74]   S. Sundaram and E. Mazur, "Inducing and probing non-thermal transitions in semiconductors using femtosecond laser pulses," *Nature Materials*, vol. 1, no. 4, pp. 217–224, 2002.

[75]   A. Tünnermann, S. Nolte, and J. Limpert, "Femtosecond vs. Picosecond Laser Material Processing," *Laser Technik Journal*, vol. 1, Jan. 2010.

[76]   K. Sugioka, M. Meunier, and A. Piqué, *Laser Precision Microfabrication*. Springer, 2010.

[77]   R. R. Gattass and E. Mazur, "Femtosecond laser micromachining in transparent materials," *Nature Photon*, Jan. 2008.

[78]   E. N. Glezer, M. Milosavljevic, L. Huang, R. J. Finlay, T. H. Her, J. P. Callan, and E. Mazur, "Three-dimensional optical storage inside transparent materials," *Opt. Lett.*, vol. 21, no. 24, p. 2023, 1996.

[79]   B. Stuart, M. Feit, A. Rubenchik, B. W. Shore, and M. Perry, "Laser-Induced Damage in Dielectrics with Nanosecond to Subpicosecond Pulses," *Phys Rev Lett*, vol. 74, no. 12, pp. 2248–2251, Mar. 1995.

[80]   B. Stuart, M. Feit, S. Herman, A. Rubenchik, B. W. Shore, and M. Perry, "Nanosecond-to-femtosecond laser-induced breakdown in dielectrics," *Phys Rev B*,

vol. 53, no. 4, pp. 1749–1761, Jan. 1996.

[81]   B. N. Chichkov, C. Momma, S. Nolte, F. vonAlvensleben, and A. Tünnermann, "Femtosecond, picosecond and nanosecond laser ablation of solids," *Applied Optics*, vol. 63, no. 2, pp. 109–115, 1996.

[82]   C. Schaffer, "Interaction of Femtosecond Laser Pulses with Transparent Materials," *garf.fis.usal.es*, Jan. 2001.

[83]   P. W. Milonni and J. H. Eberly, *Lasers*. Wiley-Interscience, 1988.

[84]   L. Keldysh, "Ionization in the Field of a Strong Electromagnetic Wave," *Sov Phys Jetp-Ussr*, vol. 20, no. 5, pp. 1307–&, Jan. 1965.

[85]   C. B. Schaffer, A. Brodeur, and E. Mazur, "Laser-induced breakdown and damage in bulk transparent materials induced by tightly focused femtosecond laser pulses," *Meas. Sci. Technol.*, Jan. 2001.

[86]   S. Tzortzakis, L. Sudrie, M. Franco, and B. Prade, "Self-Guided Propagation of Ultrashort IR Laser Pulses in Fused Silica," *Phys Rev Lett*, Jan. 2001.

[87]   A. Couairon, L. Sudrie, M. Franco, and B. Prade, "Filamentation and damage in fused silica induced by tightly focused femtosecond laser pulses," *Phys Rev B*, Jan. 2005.

[88]   I. M. Burakov, N. M. Bulgakova, R. Stoian, A. Mermillod-Blondin, E. Audouard, A. Rosenfeld, A. V. Husakou, and I. V. Hertel, "Spatial distribution of refractive index variations induced in bulk fused silica by single ultrashort and short laser pulses," *J Appl Phys*, vol. 101, no. 4, pp. 043506–043506, 2007.

[89]   M. I. Kaganov, I. M. Lifshitz, and L. V. Tanatarov, "Relaxation between electrons

and the crystalline lattice," *Sov Phys Jetp-Ussr*, vol. 4, no. 173, 1957.

[90]   S. Anisimov and B. Kapeliovich, "Electron emission from metal surfaces exposed to ultrashort laser pulses," *… Eksperimental noi i …*, 1974.

[91]   L. Jiang and H. Tsai, "Improved two-temperature model and its application in ultrashort laser heating of metal films," *J Heat Trans-T Asme*, vol. 127, no. 10, pp. 1167–1173, 2005.

[92]   E. G. Gamaly, "The physics of ultra-short laser interaction with solids at non-relativistic intensities," *Physics reports*, vol. 508, no. 4, pp. 91–243, Nov. 2011.

[93]   B. Averill and P. Eldredge, "General Chemistry: Principles, Patterns, and Applications," *cardinalscholar.bsu.edu*

, Mar. 2012.

[94]   M. Ramme, A. Housman, I. Mingareev, and M. C. Richardson, "Femtosecond Single-Pulse Light-Matter-Interaction in Semiconductors with varying Dopant Concentration," *Femtomachining 2013*. Cargese, 2013.

[95]   J. M. Liu, "Simple technique for measurements of pulsed Gaussian-beam spot sizes," *Opt. Lett.*, vol. 7, no. 5, pp. 196–198, 1982.

[96]   R. House, J. Bettis, and A. Guenther, "Subsurface structure and laser damage threshold," *Ieee J Quantum Elect*, vol. 13, no. 5, pp. 363–364, 1977.

[97]   R. Stoian, D. Ashkenasi, A. Rosenfeld, and E. Campbell, "Coulomb explosion in ultrashort pulsed laser ablation of Al2O3," *Phys Rev B*, vol. 62, no. 19, pp. 13167–13173, 2000.

[98]   L. Shah, J. Tawney, and M. C. Richardson, "Femtosecond laser deep hole drilling of

silicate glasses in air," *Appl Surf Sci*, vol. 183, pp. 151–164, Jan. 2001.

[99]   A. Ben-Yakar, A. Harkin, J. Ashmore, R. L. Byer, and H. A. Stone, "Thermal and fluid processes of a thin melt zone during femtosecond laser ablation of glass: the formation of rims by single laser pulses," *J Phys D Appl Phys*, vol. 40, no. 5, pp. 1447–1459, Feb. 2007.

[100]   D. Breitling, A. Ruf, and F. Dausinger, "Fundamental aspects in machining of metals with short and ultrashort laser pulses," pp. 49–63, 2004.

[101]   M. Ramme, A. Vaupel, M. Hemmer, J. Choi, I. Mingareev, and M. C. Richardson, "Lasers for Ultrafast Laser-Materials Processing," in in *Ultrafast Laser Processing: From Micro- to Nanoscale*, 1st ed., no. 2, K. Sugioka and Y. Cheng, Eds. Pan Stanford Publishing Pte Ltd, pp. 1–45.

[102]   G. N. Smith, K. Kalli, and K. Sugden, "Advances in femtosecond micromachining and inscription of micro and nano photonic devices," no. 15, Frontiers in Guided Wave Optics and Optoelectronics, 2010.

[103]   N. Sanner, O. Utéza, B. Chimier, M. Sentis, P. Lassonde, F. Légaré, and undefined author, "Toward determinism in surface damaging of dielectrics using few-cycle laser pulses," *Appl Phys Lett*, vol. 96, no. 7, p. 071111, 2010.

[104]   A. Borowiec and H. K. Haugen, "Subwavelength ripple formation on the surfaces of compound semiconductors irradiated with femtosecond laser pulses," *Appl Phys Lett*, vol. 82, no. 25, pp. 4462–4464, 2003.

[105]   F. Costache, M. Henyk, and J. Reif, "Modification of dielectric surfaces with ultra-short laser pulses," *Appl Surf Sci*, vol. 186, no. 1, pp. 352–357, Jan. 2002.

185

[106]   J. Reif, F. Costache, M. Henyk, and S. PANDELOV, "Ripples revisited: non-classical morphology at the bottom of femtosecond laser ablation craters in transparent dielectrics," *Appl Surf Sci*, vol. 197, pp. 891–895, Sep. 2002.

[107]   J. Bonse, A. Rosenfeld, and J. Kruger, "Implications of transient changes of optical and surface properties of solids during femtosecond laser pulse irradiation to the formation of laser-induced periodic surface structures," *Appl Surf Sci*, vol. 257, no. 12, pp. 5420–5423, Apr. 2011.

[108]   R. Buividas, L. Rosa, R. Šliupas, T. Kudrius, G. Šlekys, V. Datsyuk, and S. Juodkazis, "Mechanism of fine ripple formation on surfaces of (semi)transparent materials via a half-wavelength cavity feedback," *Nanotechnology*, vol. 22, no. 5, p. 055304, Dec. 2010.

[109]   J. Reif, O. Varlamova, S. Varlamov, and M. Bestehorn, "The role of asymmetric excitation in self-organized nanostructure formation upon femtosecond laser ablation," *Applied Optics*, Jun. 2011.

[110]   L. Petit, N. Carlie, T. Anderson, M. Couzi, J. Choi, M. C. Richardson, and K. C. Richardson, "Effect of IR femtosecond laser irradiation on the structure of new sulfo-selenide glasses," *Opt Mater*, vol. 29, no. 8, pp. 1075–1083, Apr. 2007.

[111]   D. Wortmann, M. Ramme, and J. Gottmann, "Refractive index modification using fs-laser double pulses," *Optics Express*, vol. 15, no. 16, p. 10149, Aug. 2007.

[112]   S. Guizard, P. Martin, G. Petite, P. D'Oliveira, and P. Meynadier, "Time-resolved study of laser-induced colour centres in SiO2," *J Phys-Condens Mat*, vol. 8, no. 9, pp. 1281–1290, 1996.

[113]   A. Zoubir, C. Rivero, R. Grodsky, K. C. Richardson, M. C. Richardson, T. Cardinal, and M. Couzi, "Laser-induced defects in fused silica by femtosecond IR irradiation," *Phys Rev B*, vol. 73, no. 22, p. 224117, Jun. 2006.

[114]   P. Nandi, G. Jose, C. Jayakrishnan, S. Debbarma, K. Chalapathi, K. Alti, A. K. Dharmadhikari, J. A. Dharmadhikari, and D. Mathur, "Femtosecond laser written channel waveguides in tellurite glass," *Optics Express*, vol. 14, no. 25, pp. 12145–12150, Jan. 2006.

[115]   K. Miura, J. Qiu, H. Inouye, T. Mitsuyu, and K. Hirao, "Photowritten optical waveguides in various glasses with ultrashort pulse laser," *Appl Phys Lett*, vol. 71, p. 3329, 1997.

[116]   A. Zoubir, C. Lopez, M. C. Richardson, and K. C. Richardson, "Femtosecond laser fabrication of tubular waveguides in poly(methyl methacrylate)," *Opt. Lett.*, vol. 29, no. 16, pp. 1840–1842, Jan. 2004.

[117]   A. Zoubir, M. C. Richardson, C. Rivero, and A. Schulte, "Direct femtosecond laser writing of waveguides in As~ 2S~ 3 thin films," *Opt. Lett.*, Jan. 2004.

[118]   S. Nolte, M. Will, J. Burghoff, and A. Tünnermann, "Femtosecond waveguide writing: a new avenue to three-dimensional integrated optics," *Applied Optics*, vol. 77, no. 1, pp. 109–111, Jun. 2003.

[119]   S. Nolte, M. Will, J. Burghoff, and A. Tünnermann, "Three-dimensional structuring of glass by ultrashort laser pulses," *Proceedings of SPIE*, vol. 4984, p. 194, 2003.

[120]   M. Will, J. Burghoff, S. Nolte, and A. Tünnermann, "Fabrication of three-dimensional photonics devices using femtosecond laser pulses," *Proceedings of*

SPIE, vol. 4978, p. 147, 2003.

[121]   M. Will, S. Nolte, B. N. Chichkov, and A. Tünnermann, "Optical properties of waveguides fabricated in fused silica by femtosecond laser pulses," *Applied Optics*, Jan. 2002.

[122]   G. D. Marshall, M. Ams, and M. J. Withford, "Direct laser written waveguide-Bragg gratings in bulk fused silica," *Opt. Lett.*, vol. 31, no. 18, pp. 2690–2691, 2006.

[123]   G. D. Marshall, P. Dekker, M. Ams, and J. Piper, "Directly written monolithic waveguide laser incorporating a distributed feedback waveguide-Bragg grating," *Opt. Lett.*, vol. 33, no. 9, pp. 956–958, Jan. 2008.

[124]   T. T. Fernandez, G. della Valle, R. Osellame, G. Jose, N. Chiodo, A. JHA, and P. Laporta, "Active waveguides written by femtosecond laser irradiation in an erbium-doped phospho-tellurite glass," *Optics Express*, vol. 16, no. 19, pp. 15198–15205, Jan. 2008.

[125]   R. Osellame, H. J. W. M. Hoekstra, G. Cerullo, and M. Pollnau, "Femtosecond laser microstructuring: an enabling tool for optofluidic lab-on-chips," *Laser & Photon. Rev.*, vol. 5, no. 3, pp. 442–463, Feb. 2011.

[126]   C. Schaffer, J. Garcia, and E. Mazur, "Bulk heating of transparent materials using a high-repetition-rate femtosecond laser," *Applied Optics*, vol. 76, no. 3, pp. 351–354, 2003.

[127]   S. M. Eaton, H. Zhang, P. R. Herman, F. Yoshino, L. Shah, J. Bovatsek, and A. Arai, "Heat accumulation effects in femtosecond laser-written waveguides with variable repetition rate," *Optics Express*, vol. 13, no. 12, pp. 4708–4716, 2005.

[128]   S. M. Eaton, H. Zhang, M. Ng, J. Li, W. Chen, and S. Ho, "Transition from thermal

diffusion to heat accumulation in high repetition rate femtosecond laser writing of

buried optical waveguides," *Optics Express*, vol. 16, p. 9443, Jun. 2008.

[129]   M. Ams, G. D. Marshall, D. Spence, and M. J. Withford, "Slit beam shaping method

for femtosecond laser direct-write fabrication of symmetric waveguides in …,"

Optics Express, Jan. 2005.

[130]   J. Choi, "Femtosecond laser written volumetric diffractive optical elements and their

applications," doctoral dissertation (University of Central Florida, 2009), 2009.

[131]   J. Gottmann and D. Wortmann, "Highspeed manufacturing of periodical surface and

in-volume nanostructures by fs-laser direct writing," presented at the Proceedings of

SPIE, 2008.

[132]   P. Maine, D. Strickland, P. Bado, M. Pessot, and G. Mourou, "Generation of

ultrahigh peak power pulses by chirped pulse amplification," *Ieee J Quantum Elect*,

vol. 24, no. 2, pp. 398–403, 1988.

[133]   M. Pessot, J. Squier, G. Mourou, and D. Harter, "Chirped-pulse amplification of

100-fsec pulses," *Opt. Lett.*, Jan. 1989.

[134]   O. Martinez, "3000 times grating compressor with positive group velocity

dispersion: Application to fiber compensation in 1.3-1.6 μm region," *Quantum

Electronics, IEEE Journal of*, vol. 23, no. 1, pp. 59–64, 1987.

[135]   E. Treacy, "Optical Pulse Compression with Diffraction Gratings," *Ieee J Quantum

Elect*, vol. 5, no. 9, pp. 454–&, 1969.

[136]   J. E. Midwinter and J. Warner, "The effects of phase matching method and of crystal

symmetry on the polar dependence of third-order non-linear optical polarization," *Br. J. Appl. Phys.*, vol. 16, no. 11, pp. 1667–1674, Jul. 1965.

[137]   M. E. Fermann, A. Galvanauskas, G. Sucha, and D. Harter, "Fiber-lasers for ultrafast optics," *Applied Physics B: Lasers and Optics*, vol. 65, no. 2, pp. 259–275, Aug. 1997.

[138]   G. C. Cho, B. Liu, L. Shah, Z. Liu, Y. Che, and J. Xu, "Latest developments of ultrafast fiber laser and its material applications," presented at the Proceedings of SPIE, 2009, vol. 7214, pp. 72140R–1.

[139]   D. Schaefer, J. Gottmann, M. Hermans, J. Ortmann, and I. Kelbassa, "High speed micro scanner for 3D in-volume laser micro processing," presented at the SPIE LASE, 2013, vol. 8608, pp. 860808–860808–6.

[140]   A. Zoubir, "Towards direct writing of 3-D photonic circuits using ultrafast lasers," University of Central Florida, 2004.

[141]   A. Streltsov and N. Borrelli, "Study of femtosecond-laser-written waveguides in glasses," *Journal of the Optical Society of America B*, Jan. 2002.

[142]   J. Chan, T. Huser, S. Risbud, and D. Krol, "Modification of the fused silica glass network associated with waveguide fabrication using femtosecond laser pulses," *Applied Optics*, Jan. 2003.

[143]   "Femtosecond micromachining of symmetric waveguides at 1.5 μm by astigmatic beam focusing," vol. 27, no. 21, pp. 1938–1940, 2002.

[144]   M. Will, J. Burghoff, S. Nolte, and A. Tünnermann, "Femtosecond-laser-induced refractive index modifications for fabrication of three-dimensional integrated optical

devices," *Proceedings of SPIE*, vol. 4941, p. 58, 2003.

[145]   M. Ams, G. D. Marshall, and M. J. Withford, "Study of the influence of femtosecond laser polarisation on direct writing of waveguides," *Optics Express*, vol. 14, no. 26, p. 13158, 2006.

[146]   R. Osellame, S. Taccheo, and M. Marangoni, "Femtosecond writing of active optical waveguides with astigmatically shaped beams," *Journal of the Optical Society of America B*, Jan. 2003.

[147]   G. Valle, R. Osellame, and P. Laporta, "Micromachining of photonic devices by femtosecond laser pulses," *Journal of Optics A: Pure and …*, Jan. 2009.

[148]   H. Ebendorff-Heidepriem, T. Foo, Y. Li, M. Oermann, and T. M. Monro, "New tellurite glasses for erbium fibre lasers," *Opto-Electronics and Communications Conference, 2008 and the 2008 Australian Conference on Optical Fibre Technology. OECC/ACOFT 2008. Joint conference of the*, pp. 1–2, 2008.

[149]   R. Stepien, R. Buczynski, D. Pysz, I. Kujawa, A. Filipkowski, M. Mirkowska, and R. Diduszko, "Development of thermally stable tellurite glasses designed for fabrication of microstructured optical fibers," *J Non-Cryst Solids*, vol. 357, no. 3, pp. 873–883, Feb. 2011.

[150]   T. M. Monro and H. Ebendorff-Heidepriem, "Progress in Microstructured Optical Fibers," *Annual Review Of Materials Research*, Jan. 2006.

[151]   J. Wang, E. VOGEL, and E. Snitzer, "Tellurite glass: a new candidate for fiber devices," *Optical materials(Amsterdam)*, vol. 3, pp. 187–203, Jan. 1994.

[152]   X. Feng, A. K. Mairaj, D. W. Hewak, and T. M. Monro, "Nonsilica glasses for holey

fibers," *Lightwave Technology, Journal of*, vol. 23, no. 6, pp. 2046–2054, 2005.

[153] X. Feng, F. Poletti, A. Camerlingo, F. Parmigiani, P. Petropoulos, P. Horak, G. M. Ponzo, M. Petrovich, J. Shi, W. H. Loh, and D. J. Richardson, "Dispersion controlled highly nonlinear fibers for all-optical processing at telecoms wavelengths," *Optical Fiber Technology*, vol. 16, no. 6, pp. 378–391, Dec. 2010.

[154] A. Mori, "Tellurite-based fibers and their applications to optical communication networks," *J Ceram Soc Jpn*, vol. 116, no. 1358, pp. 1040–1051, 2008.

[155] C. Rivero, K. C. Richardson, and R. Stegeman, "Quantifying Raman gain coefficients in tellurite glasses," *Journal of Non- …*, Jan. 2004.

[156] M. D. O'donnell, K. C. Richardson, R. Stolen, A. B. Seddon, D. Furniss, V. K. Tikhomirov, C. Rivero, M. Ramme, R. Stegeman, G. Stegeman, M. Couzi, and T. Cardinal, "Tellurite and fluorotellurite glasses for fiberoptic Raman amplifiers: Glass characterization, optical properties, Raman gain, preliminary fiberization, and fiber characterization," *J Am Ceram Soc*, vol. 90, no. 5, pp. 1448–1457, 2007.

[157] R. R. Gattass, "Femtosecond-laser interactions with transparent materials: applications in micromachining and supercontinuum generation," mazur-www.harvard.edu, 2006.

[158] D. Ashkenasi, R. Stoian, and A. Rosenfeld, "Single and multiple ultrashort laser pulse ablation threshold of Al2O3 (corundum) at different etch phases," *Appl Surf Sci*, vol. 154, pp. 40–46, 2000.

[159] J. Bonse, S. Baudach, J. Kruger, W. Kautek, and M. Lenzner, "Femtosecond laser ablation of silicon–modification thresholds and morphology," *Applied Optics*, Jan.

2002.

[160]   J. Kruger and W. Kautek, "Ultrashort Pulse Laser Interaction with Dielectrics and Polymers," *ADVANCES IN POLYMER SCIENCE*, Jan. 2004.

[161]   M. Lenzner and W. Rudolph, "Laser-induced optical breakdown in solids," *Strong Field Laser Physics*, vol. 134, no. 11, pp. 243–257, 2009.

[162]   C. Schaffer, A. BRODEUR, J. García, and E. Mazur, "Micromachining bulk glass by use of femtosecond laser pulses with nanojoule energy," *Opt. Lett.*, Jan. 2001.

[163]   M. Ramme, "Refractive index modification in fused silica by using fs-laser single and double pulses," University of Applied Science Aachen, Aachen, Germany, 2006.

[164]   S. M. Eaton, M. L. Ng, T. Rafique, and P. R. Herman, "High refractive index contrast in fused silica waveguides by tightly focused, high-repetition rate femtosecond laser," presented at the Lasers and Electro-Optics, 2009 and 2009 Conference on Quantum electronics and Laser Science Conference. CLEO/QELS 2009. Conference on, 2009, pp. 1–2.

[165]   A. Barty, K. Nugent, D. Paganin, and A. Roberts, "Quantitative optical phase microscopy," *Opt. Lett.*, vol. 23, no. 11, pp. 817–819, Jan. 1998.

[166]   D. Paganin and K. Nugent, "Noninterferometric phase imaging with partially coherent light," *Phys Rev Lett*, vol. 80, no. 12, pp. 2586–2589, Jan. 1998.

[167]   K. Nugent, D. Paganin, and T. Gureyev, "A phase odyssey," *Phys Today*, vol. 54, no. 8, pp. 27–32, Jan. 2001.

[168]   T. T. Fernandez, S. M. Eaton, G. della Valle, M. R. Vazquez, M. Irannejad, G. Jose,

A. JHA, G. Cerullo, R. Osellame, and P. Laporta, "Femtosecond laser written optical waveguide amplifier in phospho-tellurite glass," *Optics Express*, vol. 18, no. 19, pp. 20289–20297, 2010.

[169]   I. Miyamoto, K. Cvecek, Y. Okamoto, M. Schmidt, and H. Helvajian, "Characteristics of laser absorption and welding in FOTURAN glass by ultrashort laser pulses," *Optics Express*, vol. 19, no. 23, pp. 22961–22973, 2011.

[170]   I. Miyamoto, K. Cvecek, and M. Schmidt, "Simple Evaluation Procedure of Nonlinear Absorptivity in Glass Welding using USLP with High-Pulse Repetition Rates," *Physics Procedia*, 2012.

[171]   F. Quintero, J. Pou, F. Lusquiños, and A. Riveiro, "Experimental analysis of the production of micro-and nanofibres by Laser Spinning," *Appl Surf Sci*, vol. 254, no. 4, pp. 1042–1047, 2007.

[172]   F. Quintero, A. B. Mann, J. Pou, F. Lusquiños, and A. Riveiro, "Rapid production of ultralong amorphous ceramic nanofibers by laser spinning," *Appl Phys Lett*, vol. 90, no. 15, p. 153109, 2007.

[173]   F. Quintero, J. Pou, R. Comesaña, F. Lusquiños, A. Riveiro, A. B. Mann, R. G. Hill, Z. Y. Wu, and J. R. Jones, "Laser Spinning of Bioactive Glass Nanofibers," *Advanced Functional Materials*, vol. 19, no. 19, pp. 3084–3090, Oct. 2009.

[174]   F. Quintero, O. Dieste, J. Pou, F. Lusquiños, and A. Riveiro, "On the conditions to produce micro- and nanofibres by laser spinning," *J Phys D Appl Phys*, vol. 42, no. 6, p. 065501, Feb. 2009.

[175]   N. Bulgakova, R. Stoian, and A. Rosenfeld, "Laser-induced modification of

transparent crystals and glasses," *Quantum Electron+*, vol. 40, no. 11, pp. 966–985, 2010.

[176]   F. Livingston, W. Hansen, A. Huang, and H. Helvajian, "Effect of laser parameters on the exposure and selective etch rate in photostructurable glass," *Proceedings of SPIE*, vol. 4637, p. 404, 2002.

[177]   E. R. Dobrovinskaya, L. A. Lytvynov, and V. Pishchik, "Properties of sapphire," in in *Sapphire*, Springer, 2009, pp. 55–176.

[178]   J. Kruger, M. Lenzner, S. Martin, M. Lenner, C. Spielmann, A. Fiedler, and W. Kautek, "Single-and multi-pulse femtosecond laser ablation of optical filter materials," *Appl Surf Sci*, vol. 208, pp. 233–237, 2003.

[179]   Y. Jee, M. F. Becker, and R. M. Walser, "Laser-induced damage on single-crystal metal surfaces," *J Opt Soc Am B*, vol. 5, no. 3, pp. 648–659, 1988.

[180]   I. Miyamoto, K. Cvecek, and M. Schmidt, "Evaluation of Nonlinear Absorptivity and Absorption Region in Fusion Welding of Glass using Ultrashort Laser Pulses," *Physics Procedia*, 2011.

[181]   I. Miyamoto, K. Cvecek, and M. Schmidt, "Evaluation of nonlinear absorptivity in internal modification of bulk glass by ultrashort laser pulses," *Optics Express*, vol. 19, no. 11, pp. 10714–10727, 2011.

[182]   S. Richter, S. Döring, A. Tünnermann, and S. Nolte, "Bonding of glass with femtosecond laser pulses at high repetition rates," *Applied Physics A: …*, vol. 103, no. 2, pp. 257–261, 2011.

[183]   O. Dieste, F. Quintero, J. Pou, F. Lusquiños, and A. Riveiro, "Influence of the

working conditions on nanofiber diameters obtained by laser spinning," *Applied Optics*, vol. 104, no. 4, pp. 1217–1222, May 2011.

[184]   F. Quintero, F. Varas, J. Pou, F. Lusquiños, M. Boutinguiza, R. Soto, and M. Pérez-Amor, "Theoretical analysis of material removal mechanisms in pulsed laser fusion cutting of ceramics," *J Phys D Appl Phys*, vol. 38, no. 4, p. 655, 2005.

[185]   P. M. Fauchet, "Surface ripples on silicon and gallium arsenide under picosecond laser illumination," *Appl Phys Lett*, vol. 40, no. 9, p. 824, 1982.

[186]   D. C. Emmony, "Laser mirror damage in germanium at 10.6 μm," *Appl Phys Lett*, vol. 23, no. 11, pp. 598–600, 1973.

[187]   H. J. Leamy, G. A. Rozgonyi, T. T. Sheng, and G. K. Celler, "Periodic regrowth phenomena produced by laser annealing of ion-implanted silicon," *Appl Phys Lett*, vol. 32, no. 9, pp. 535–537, 1978.

[188]   A. K. Jain, "Periodic surface ripples in laser-treated aluminum and their use to determine absorbed power," *J Appl Phys*, vol. 52, no. 7, pp. 4882–4884, 1981.

[189]   J. C. Koo and R. E. Slusher, "Diffraction from laser-induced deformation on reflective surfaces," *Appl Phys Lett*, vol. 28, no. 10, pp. 614–616, 1976.

[190]   N. R. Isenor, "CO2 laser-produced ripple patterns on NixP1−x surfaces," *Appl Phys Lett*, vol. 31, no. 3, pp. 148–150, 1977.

[191]   P. Temple and M. Soileau, "Polarization charge model for laser-induced ripple patterns in dielectric materials," *Ieee J Quantum Elect*, vol. 17, no. 10, pp. 2067–2072, Oct. 1981.

[192]   J. E. Sipe, J. Young, J. Preston, and H. M. van Driel, "Laser-induced periodic

surface structure. I. Theory," *Phys Rev B*, vol. 27, no. 2, pp. 1141–1154, 1983.

[193]   J. Bonse, M. Munz, and H. Sturm, "Structure formation on the surface of indium phosphide irradiated by femtosecond laser pulses," *J Appl Phys*, vol. 97, no. 1, pp. 013538–013538, 2005.

[194]   M. Couillard, A. Borowiec, H. K. Haugen, J. S. Preston, E. M. Griswold, and G. A. Botton, "Subsurface modifications in indium phosphide induced by single and multiple femtosecond laser pulses: A study on the formation of periodic ripples," *J Appl Phys*, vol. 101, no. 3, p. 033519, 2007.

[195]   T. Jia, H. Chen, M. Huang, F. Zhao, J. Qiu, R. Li, Z. Xu, X. He, J. Zhang, and H. Kuroda, "Formation of nanogratings on the surface of a ZnSe crystal irradiated by femtosecond laser pulses," *Phys Rev B*, vol. 72, no. 12, p. 125429, Sep. 2005.

[196]   J. Reif, O. Varlamova, and F. Costache, "Femtosecond laser induced nanostructure formation: self-organization control parameters," *Applied Optics*, vol. 92, no. 4, pp. 1019–1024, Jun. 2008.

[197]   A. Andreev, M. Nazarov, I. Prudnikov, A. Shkurinov, and P. Masselin, "Noncollinear excitation of surface electromagnetic waves: Enhancement of nonlinear optical surface response," *Phys Rev B*, vol. 69, no. 3, p. 035403, Jan. 2004.

[198]   V. Bhardwaj, V. Bhardwaj, E. Simova, E. Simova, P. Rajeev, P. Rajeev, C. Hnatovsky, C. Hnatovsky, R. Taylor, R. Taylor, D. Rayner, D. Rayner, P. B. Corkum, and P. B. Corkum, "Optically Produced Arrays of Planar Nanostructures inside Fused Silica," *Phys Rev Lett*, vol. 96, no. 5, p. 057404, Feb. 2006.

[199]   W. Yang, E. Bricchi, P. G. Kazansky, J. Bovatsek, and A. Arai, "Self-assembled

periodic sub-wavelength structures by femtosecond laser direct writing," *Optics Express*, vol. 14, no. 21, pp. 10117–10124, 2006.

[200]   R. S. Taylor, C. Hnatovsky, E. Simova, P. P. Rajeev, D. M. Rayner, and P. B. Corkum, "Femtosecond laser erasing and rewriting of self-organized planar nanocracks in fused silica glass," *Opt. Lett.*, vol. 32, no. 19, pp. 2888–2890, 2007.

[201]   T. H. R. Crawford and H. K. Haugen, "Sub-wavelength surface structures on silicon irradiated by femtosecond laser pulses at 1300 and 2100 nm wavelengths," *Appl Surf Sci*, vol. 253, no. 11, pp. 4970–4977, Mar. 2007.

[202]   T. Tomita, R. Kumai, H. Nomura, and S. Matsuo, "Surface roughness assisted 100 kHz femtosecond laser induced nanostructure formation on silicon surface," *Applied Optics*, 2011.

[203]   E. Martinez, E. Martinez, E. Engel, E. Engel, J. PLANELL, J. PLANELL, J. Samitier, and J. Samitier, "Effects of artificial micro- and nano-structured surfaces on cell behaviour," *Annals of Anatomy - Anatomischer Anzeiger*, vol. 191, no. 1, pp. 126–135, Jan. 2009.

[204]   M. Shen, C. H. Crouch, J. E. Carey, R. Younkin, and E. Mazur, "Formation of regular arrays of silicon microspikes by femtosecond laser irradiation through a mask," *Appl Phys Lett*, vol. 82, no. 11, Jan. 2003.

[205]   M. Halbwax, T. Sarnet, P. Delaporte, M. Sentis, H. Etienne, F. Torregrosa, V. Vervisch, I. Perichaud, and S. Martinuzzi, "Micro and nano-structuration of silicon by femtosecond laser: Application to silicon photovoltaic cells fabrication," *Thin Solid Films*, vol. 516, no. 20, pp. 6791–6795, Aug. 2008.

[206]   M. Ramme, J. Choi, T. Anderson, I. Mingareev, and M. C. Richardson, "Sub-micron machining of semiconductors-Femtosecond surface ripples on GaAs by 2 µm laser light," presented at the Proceedings of SPIE, 2010, vol. 7590, p. 8.

[207]   M. Bass, W. L. Wolfe, E. Van Stryland, and D. R. Williams, *Handbook of Optics*. McGraw-Hill Professional, 1995.

[208]   M. Ramme, J. Choi, T. Anderson, and M. C. Richardson, "Femtosecond Laser Materials Processing In The Townes Laser Institute," presented at the ICALEO Proceedings, 2009, pp. 1–8.

[209]   F. Lukeš, "Oxidation of Si and GaAs in air at room temperature," *Surface Science*, vol. 30, no. 1, pp. 91–100, 1972.

[210]   J. Ihlemann, B. WOLFF, and P. SIMON, "Nanosecond and Femtosecond Excimer Laser Ablation of Fused-Silica," *Applied Optics*, vol. 54, no. 4, pp. 363–368, 1992.

[211]   D. Ashkenasi, A. Rosenfeld, H. Varel, and M. Wähmer, "Laser processing of sapphire with picosecond and sub-picosecond pulses," *Appl Surf Sci*, 1997.

[212]   X. Liu, D. Du, and G. Mourou, "Laser ablation and micromachining with ultrashort laser pulses," *Ieee J Quantum Elect*, vol. 33, no. 10, pp. 1706–1716, Jan. 1997.

[213]   H. O. Jeschke, M. Garcia, M. Lenzner, and J. Bonse, "Laser ablation thresholds of silicon for different pulse durations: theory and experiment," *Appl Surf Sci*, Jan. 2002.

[214]   M. MacKenzie, A. Borowiec, G. C. Weatherly, and H. K. Haugen, "Femtosecond laser pulse ablation of GaAs and InP: studies utilizing scanning and transmission electron microscopy," *Applied Optics*, vol. 77, no. 3, pp. 411–417, Aug. 2003.

[215]   J. Bovatsek, L. Shah, A. Arai, and Y. Uehara, "Laser ablation threshold and etch rate

comparison between the ultrafast Yb fiber-based FCPA laser …," *Proceedings of*

SPIE, Jan. 2004.

[216]   A. Marcinkevičius, S. Juodkazis, M. Watanabe, M. Miwa, S. Matsuo, H. Misawa,

and J. Nishii, "Femtosecond laser-assisted three-dimensional microfabrication in

silica," *Opt. Lett.*, vol. 26, no. 5, pp. 277–279, 2001.

[217]   E. W. Van Stryland and M. Sheik-Bahae, "Z-Scan Measurements of Optical

Nonlinearities," *Characterization Techniques and Tabulations for Organic*

Nonlinear Materials, MG Kuzyk and CW Dirk, eds.,(Marcel Dekker, Inc., 1998), pp.

655–692, 1998.

[218]   A. H. Nejadmalayeri, P. Scrutton, J. Mak, A. S. Helmy, P. R. Herman, J. Burghoff,

S. Nolte, A. Tünnermann, and J. Kaspar, "Solid phase formation of silicon

nanocrystals by bulk ultrafast laser-matter interaction," *Opt. Lett.*, vol. 32, no. 24,

pp. 3474–3476, 2007.

[219]   R. Martinez-Vazquez, R. Osellame, G. Cerullo, and O. Svelto, "Fabrication of

photonic devices in nanostructured glasses by femtosecond laser pulses," *Optics*

Express, vol. 15, no. 20, p. 12628, Jan. 2007.

[220]   A. D. Bristow, N. Rotenberg, and H. M. Van Driel, "Two-photon absorption and

Kerr coefficients of silicon for 850–2200," *Appl Phys Lett*, vol. 90, no. 19, pp.

191104–191104–3, 2007.

[221]   X. Liu, R. M. Osgood, Y. A. Vlasov, and W. M. J. Green, "Mid-infrared optical

parametric amplifier using silicon nanophotonic waveguides," *Nature*, vol. 4, no. 8,

pp. 557–560, May 2010.

[222]   I. B. Bogatyrev, D. Grojo, P. Delaporte, S. Leyder, M. Sentis, W. Marine, and T. E. Itina, "Non-linear absorption of 1.3-µm wavelength femtosecond laser pulses focused inside semiconductors: Finite difference time domain-two temperature model combined computational study," *J Appl Phys*, vol. 110, no. 10, pp. 103106–103106–10, 2011.

[223]   S. Leyder, D. Grojo, P. Delaporte, W. Marine, M. Sentis, and O. Utéza, "Non-linear absorption of focused femtosecond laser pulses at 1.3µm inside silicon: Independence on doping concentration," *Appl Surf Sci*, Nov. 2012.

[224]   K. Bennemann, "Ultrafast dynamics in solids," *J Phys-Condens Mat*, vol. 16, no. 30, pp. R995–R1056, 2004.

[225]   K. Sokolowski-Tinten, J. Bialkowski, A. Cavalleri, D. von der Linde, A. Oparin, J. Meyer-ter-Vehn, and S. Anisimov, "Transient states of matter during short pulse laser ablation," *Phys Rev Lett*, vol. 81, no. 1, pp. 224–227, Jan. 1998.

[226]   V. V. Temnov, K. Sokolowski-Tinten, P. Zhou, and D. von der Linde, "Femtosecond time-resolved interferometric microscopy," *Applied Optics*, vol. 78, no. 4, pp. 483–489, Mar. 2004.

[227]   K. Sokolowski-Tinten and D. von der Linde, "Generation of dense electron-hole plasmas in silicon," *Phys Rev B*, vol. 61, no. 4, pp. 2643–2650, 2000.

[228]   K. Sokolowski-Tinten, J. Bialkowski, A. Cavalleri, and D. von der Linde, "Observation of a transient insulating phase of metals and semiconductors during short-pulse laser ablation," *Appl Surf Sci*, vol. 127, pp. 755–760, 1998.

[229]   J. Callan, A. Kim, L. Huang, and E. Mazur, "Ultrafast electron and lattice dynamics in semiconductors at high excited carrier densities," *Chemical Physics*, vol. 251, no. 1, pp. 167–179, 2000.